Divergent changes in aerosol optical hygroscopicity and new particle

2	formation induced by heatwaves
3 4 5 6	Yuhang Hao ^{1, a} , Peizhao Li ^{1, a} , Yafeng Gou ¹ , Zhenshuai Wang ¹ , Mi Tian ¹ , Yang Chen ² , Ye Kuang ³ , Hanbing Xu ⁴ , Fenglian Wan ¹ , Yuqian Luo ¹ , Wei Huang ⁵ , Jing Chen ^{1, 6, *}
7	¹ College of Environment and Ecology, Chongqing University, Chongqing 400045,
8	China
9	² Center for the Atmospheric Environment Research, Chongqing Institute of Green
10	and Intelligent Technology, Chinese Academy of Sciences, Chongqing 400714, China
11	³ Institute for Environmental and Climate Research, Jinan University, Guangzhou
12	511443, China
13	⁴ Experimental Teaching Center, Sun Yat-sen University, Guangzhou 510275, China
14	⁵ National Meteorological Center, China Meteorological Administration, Beijing
15	100081, China
16	⁶ Key Laboratory of Three Gorges Reservoir Region's Eco-Environment, Ministry of
17	Education, Chongqing University, Chongqing 400045, China
18 19 20	^a These authors contributed equally
21	Correspondence to: Jing Chen (chen.jing@cqu.edu.cn)

22 **Abstract.** As a crucial climate-forcing driver, the aerosol optical enhancement factor 23 (f(RH)) is significantly modulated by chemical compositions and the evolution of 24 particle number size distribution (PNSD), e.g., during new particle formation (NPF). 25 However, Tthe mechanisms regulating aerosol optical hygroscopicity during different 26 NPF eventdays and non-event days, particularly those influenced by heatwaves due to global warming, remain poorly understood. In the extremely hot summer of 2022 in 27 28 urban Chongqing of southwest China, simultaneous measurements of aerosol optical 29 and hygroscopic properties, PNSD, and bulk chemical compositions were conducted. 30 Two distinct types of NPF were identified: the ones with relatively polluted period 31 (P1NPF_P) and clean cases during heatwave-dominated period (P2NPF_{C, HW}). Compared 32 to the NPF_P events, Heatwaves triggered NPF_C, HWNPF occurred approximately one 33 hour earlier and prolonged the subsequent growth was prolonged, accompanied 34 byresulting in a smaller aerosol effective radius (R_{eff}) and lower formation/growth rate 35 during heatwaves. This agreed with the concurrently increased aerosol hemispheric backscattering fraction and scattering Ångström exponent. f(RH) was generally higher 36 37 during on NPF-eventdays in comparison to that for non-event cases in both periods. 38 Moreover, Hheatwave-induced stronger photooxidation may intensify the formation of 39 more hygroscopic secondary components, as well as the atmospheric aging/subsequent 40 growth of both pre-existing particles and newly formed ultrafine particles ones, thereby 41 enhancing f(RH)aerosol optical hygroscopicity especially during heatwave-influenced 42 NPF_{C. HW}NPF eventdays. The promoted f(RH) and lowered R_{eff} could synergistically 43 elevate the aerosol direct radiative forcing, specifically under persistent heatwave 44 conditions. Further in-depth exploration on molecular-level characterizations and 45 aerosol radiative impacts of both direct and indirect interactions during weather 46 extremes (e.g., heatwaves) with the warming climate are recommended.

47

48 **1 Introduction**

49

50

51

52

53

54

55

56

57

58

59

60

61

62

63

64

65

66

67

68

69

70

71

72

73

74

75

76

Weather extremes (e.g., heatwaves) have become more and more frequent and intense largely due to the global climate change, and the heatwave-driven environmental, climatic, and health effects have garnered widespread attention (Hauser et al., 2016; Sun et al., 2016). The China Climate Bulletin 2022 confirmed that the national average temperature reached an unprecedented high level since 2012 (China Meteorological Administration, 2022), and the risk of heatwaves in China will persist and potentially intensify in the future (Guo et al., 2016; Li et al., 2017). Extreme heatwave events could pose significant threats to human health, the survival of organisms, agriculture, and socio-economic activities (e.g., power supply restrictions) (Anderson and Bell, 2011; Ma et al., 2021; Su, 2021). Moreover, heatwaves can trigger natural disasters such as droughts and wildfires, affecting social stability (Sharma and Mujumdar, 2017). Heatwaves could also affect the atmospheric physical and chemical processes by modulating ambient meteorological conditions. Specifically, extremely high temperature weather is typically characterized by a combination of intensified solar radiation with elevated temperature and low humidity levels. This could significantly affect the formation and evolution of secondary aerosols in the atmosphere (Bousiotis et al., 2021; Hamed et al., 2011; Kurtén et al., 2007), given that the air temperature is crucial for chemical reactions (Xu et al., 2011). New particle formation (NPF) serves as a crucial source of atmospheric particulate matter and plays a significant role in the secondary transformation processes in the atmosphere (Zhu et al., 2021). Generally, NPF involves the initial formation of thermodynamically stable clusters from condensable vapors (e.g., ammonia, sulfuric acid, and organic precursor gases) and subsequent growth of the formed clusters, eventually reaching detectable sizes or even larger dimensions (Kerminen et al., 2018; Kulmala et al., 2003, 2012). Over time, these newly formed particles have the potential to serve as cloud condensation nuclei (CCN), thereby impacting the global climate (Salma et al., 2016). NPF events normally introduce a sharp increase in the number concentration of nucleation mode particles

77 within a short time, altering the particle number size distribution (PNSD). These 78 variations in PNSD likely influence intrinsic physicochemical properties of aerosols, 79 such as the optical hygroscopicity (Chen et al., 2014; Titos et al., 2016; Zhao et al., 80 2019). 81 Aerosol hygroscopicity plays a critical role in the atmospheric environment and climate 82 change, given the complex interaction between aerosol particles and water vapor (Zhao 83 et al., 2019; Zieger et al., 2011). Water uptake by aerosols not only alters the particle 84 size and composition (e.g., as reflected in the aerosol refractive index) but also impacts 85 aerosol scattering efficiency, which further contributes to the uncertainty in aerosol radiative forcing estimation (Titos et al., 2016, 2021). The aerosol optical 86 87 hygroscopicity parameter, f(RH), defined as the ratio of the scattering coefficient at a 88 certain RH to that of the dry condition, was widely used to describe the aerosol 89 scattering enhancement through water uptake (Covert et al., 1972; Titos et al., 2016; 90 Zhao et al., 2019). Numerous studies have demonstrated that f(RH) is influenced by the 91 size distribution, in addition to particle chemical composition (Chen et al., 2014; Kuang 92 et al., 2017; Petters and Kreidenweis, 2007; Quinn et al., 2005). There is currently 93 limited research on the variations in aerosol optical hygroscopicity during NPF days 94 despite significant changes in aerosol size distributions and chemical compositions, 95 partly due to that newly formed particles insignificantly affect the optical properties of 96 aerosols (Kuang et al., 2018). However, previous studies have observed the 97 enhancement in aerosol hygroscopicity (Cheung et al., 2020; Wu et al., 2015, 2016) and 98 extinction coefficients (Shen et al., 2011; Sun et al., 2024) during the subsequent growth 99 of NPF.NPF could alter the size distribution thereby aerosol optical properties, 100 nonetheless, there is currently limited research on the impact of NPF on aerosol optical 101 hygroscopicity (Ma et al., 2016; Ren et al., 2021). It is suggested that the influence of 102 NPF on aerosol hygroscopicity was likely due to changes in aerosol chemical 103 composition at different stages of NPF events (Cheung et al., 2020), whereas the 104 subsequent particle growth associated with NPF events can significantly affect particle 105 hygroscopicity as well (Wu et al., 2016). Although there have been a great 106 manyprevious studies onshowed the chemical composition dependences of aerosol

hygroscopicity on chemical composition (Petters and Kreidenweis, 2007; Titos et al., 2016; Zhao et al., 2019) (e.g., the variation in composition of precursor species during NPF events), it is important to acknowledge that the utilized chemical compositions of NPF were either from PM_{2.5} or PM₁ bulk data, which This may differ from the corresponding composition of newly formed ultrafine particles primarily in the nucleation and Aitken modes. This may, further introduceing bias in exploring the impacts of NPF events and subsequent growth on aerosol optical hygroscopicity if solely based on PM_{2.5} chemical composition, especially in the initial nucleation stage of NPF. Hence, more comprehensive investigations on the influencing mechanisms of aerosol optical hygroscopicity from different perspectives are required, e.g., for the aspects of the evolution of particle size distribution in modulating aerosol optical and hygroscopic properties (Tang et al., 2019; Zhao et al., 2019). Additionally, field observations on f(RH) under extreme weather conditions (e.g., heatwaves) are rather scarce, largely hindering our understanding of how weather extremes (e.g., extremely high temperature) influence the optical hygroscopic properties of aerosols. This knowledge gap further impedes comprehensive understanding of the aerosol water uptake property and resulted effects on air quality and the climate under varied synoptic conditions.

During the summer of 2022, a rare heatwave event raged throughout China, especially the Sichuan-Chongqing region of southwest China (Chen et al., 2024; Wang et al., 2024), with the daily maximum temperature exceeding 40 °C lasted for 29 days observed at Beibei meteorological station in Chongqing (Hao et al., 2023). This persistent heatwave not only impacted residents' daily lives significantly, but also affected the aerosol optical and hygroscopic properties likely through NPF-changed aerosol physicochemical characteristics and relevant atmospheric processing during the period. In this study, a field observation was conducted by using a combination of a home-built humidified nephelometer system and a scanning mobility particle sizer (SMPS), along with the total suspended particle (TSP) filter sampling. A main goal of this study is to investigate the influence of heatwaves on both aerosol optical hygroscopicity and the NPF with subsequent growth events, along with the related

discrepancies and subsequent impacts on aerosol optical and hygroscopic properties. Furthermore, we aimed to explore the mechanisms behind the variability in f(RH) under different meteorological conditions and diverse NPF events. This study will further enrich insights into the potential environmental and climatic impacts due to variations in the aerosol optical hygroscopicity and size distribution, specifically under weather extremes (e.g., heatwaves) with the changing climate.

143

144

145

146

147

148

149

150

151

152

153

154

155

156

157

158

159

160

161

162

163

142

137

138

139

140

141

2 Data and Methods

2.1 Field observation

A continuous field observation on aerosol optical, hygroscopic and chemical properties was carried out from July 29 to August 19, 2022. The detailed description of the observation site is available in Supporting Information, S1. During the observation period, urban Chongqing suffered a rare heatwave (Fig. S1; Chen et al., 2024; Wang et al., 2024), which significantly affected the local transportation and industrial activities (Hao et al., 2023). China Meteorological Administration (CMA) defines heatwaves as three or more consecutive days with daily maximum temperature (T_{max}) above 35 °C (http://www.cmastd.cn/standardView.jspx?id=2103; Guo et al., 2016; Sun et al., 2014; Tan et al., 2007). Since no unified definition of heatwaves worldwide Based on the temperature records and concurrent aerosol light scattering data, the whole study period was categorized into two stages according to CMA's criteria of the daily T_{max} records and the Excess Heat Factor (EHF) metric proposed by Nairn and Fawcett (2014) (Fig. S2a): (1) the normally hot period (with the daily maximum temperature seldomly above 35°C) from 29 July to 6 August (markedsimply labeled as P1); (2) the heatwavedominated period from August 7-19 (marked as P2) characterized with the consistently occurrence of T_{max} exceeding 38 °C (approximately the last 25th percentile of temperature records for the whole observation period; Fig. S2b). the heatwavedominated cleaner period (persistent occurrence of the hourly temperature over 40°C,

and the hourly total scattering coefficient at 525 nm below 100 Mm⁻¹) during 7-19

165 August 2022 (marked as P2).

2.2 Instrumentation and methods

166

167

189

190

2.2.1 Measurements of aerosol optical hygroscopicity

168 The humidified nephelometer system, consisting of two three-wavelength (i.e., 169 450, 525, and 635 nm) nephelometers (Model Aurora 3000, Ecotech Inc.) and a 170 humidification unit, was used to determine the aerosol light scattering enhancement 171 factor, f(RH). Ambient air was firstly dried through a Nafion dryer (model MD-700, 172 Perma Pure LLC) to ensure RH <35%, then split into two streams for both dry and 173 humidified nephelometers operated in parallel. The flowrate for each nephelometer was 174 <u>2.6 LPM.</u> Briefly, tThe aerosol scattering $(\sigma_{sca,\lambda})$ and backscattering coefficients $(\sigma_{bsca,\lambda})$ 175 λ) were detected in a dry state (RH <3.05%) and at a fixed-controlled RH level of 85% 176 ± 1%, respectively, with the humidification efficiency regulated automatically by a 177 temperature-controlled water bath. More details on the home-built humidified 178 nephelometer system are available in Kuang et al. (2017, 2020) and Xue et al. (2022). 179 Hence, f(RH) could be calculated as the ratio of the aerosol scattering coefficient 180 at a predefined RH ($\sigma_{sca, RH}$) to the dry ($\sigma_{sca, dry}$) state, i.e., $f(RH) = \sigma_{sca, RH} / \sigma_{sca, dry}$ 181 (Covert et al., 1972). In this study, the f(RH) discussed is mainly targeted for the 525 182 nm wavelength, unless otherwise specified. More information about the measurement 183 of humidified nephelometer system was illustrated in S2 of the supplement. In additional to f(RH), aerosol optical parameters, such as scattering Ångström 184 exponent (SAE; Schuster et al., 2006) and hemispheric backscattering fraction (HBF; 185 Collaud Coen et al., 2007), were calculated as below: 186

$$SAE_{\lambda 1/\lambda 2} = \frac{-\ln(\sigma_{sca, \lambda 1}/\sigma_{sca, \lambda 2})}{\ln(\lambda 1/\lambda 2)}$$
 (1)

$$HBF_{\lambda} = \frac{\sigma_{bsca, \lambda}}{\sigma_{sca, \lambda}} \tag{2}$$

where $\sigma_{sca, \lambda}$ and $\sigma_{bsca, \lambda}$ represent the aerosol scattering and backscattering coefficients at a specific wavelength λ (e.g., $\lambda 1$, $\lambda 2$), respectively.

Both HBF and SAE reflect crucial optical properties of aerosols, e.g., an elevated HBF (or SAE) generally signifies a higher concentration (or a smaller particle size) of fine particles within the aerosol population (Jefferson et al., 2017; Kuang et al., 2017; Luoman et al., 2019). The HBF and SAE discussed in this study are targeted for the dry condition, unless otherwise specified. Based on the measurements with the humidified nephelometer system, the equivalent aerosol liquid water content (ALWC) and the corresponding fraction of ALWC (f_W) can also be obtained (Kuang et al, 2018; see <u>Sect.</u> S2 of the supplement).

The SMPS-measured concurrent particle number size distributions were further utilized to calculate the aerosol effective radius (R_{eff}) and representative parameters for NPF events, e.g., the <u>formation rate (FR) and growth rate (GR)</u> of new particle, condensation sink (CS) and coagulation sink (CoagS) (<u>Dal Maso et al., 2005</u>; Kulmala et al., 2012). More details are provided in the supplement (Sect. S5).

Results of the offline chemical analysis with TSP filter samples are provided in Sect. S3 and Fig. S3. It should be noted that certain secondary organics and crustal elements (e.g., Ca²⁺, Mg²⁺) that could exhibit a broader size distribution may contribute to the observed discrepancy in the total mass concentration between the 24-h TSP samples and daily mean PM_{2.5} (of similar temporal variations; Fig.S3) (Duan et al., 2024; Kim et al., 2020; Xu et al., 2021). Nonetheless, previous studies reported that key components such as SNA (i.e., SO₄²⁻, NO₃⁻, and NH₄⁺) and primary organics of PM_{2.5} (or PM₁₀) were predominantly concentrated within the submicron size range (An et al., 2024; Bae et al., 2019; Chen et al., 2019; Duan et al., 2024; Kim et al., 2020; Xu et al., 2024). While the use of TSP samples contains some uncertainties, the bulk chemical information remains reasonable for characterizing the optical and hygroscopic properties of PM_{2.5}. The descriptions of simultaneous meteorological and air quality data can be found in Sect. S4, and the 48-h backward trajectory analysis was given in Sect. S5 of the supplement.

2.2.2 Determination of the aerosol direct radiative forcing (ADRF) enhancement factor

- Given the high sensitivity of aerosol optical properties (e.g., f(RH)) to the changes in RH under real atmospheric conditions, the influence of RH, or rather the aerosol hygroscopicity, on ADRF can be quantitatively estimated with the radiative transfer model by the following equation (Chylek and Wong, 1995; Kotchenruther et al., 1999; L. Zhang et al., 2015):
- $\Delta F_{R}(RH) = -(S_{0}/4) \times [T_{a}^{2} \times (1 A_{C})] \times [2 \times (1 R_{s})^{2} \times \beta(RH) \times \tau_{s} 4 \times R_{s} \times \tau_{a}]$ (3)
 - where S_0 is the solar constant, T_a is the atmosphere transmittance, A_C is the fractional cloud amount, R_s is the albedo of the underlying surface, $\beta(RH)$ is the upscattering fraction at a defined RH, τ_s and τ_a are the optical thicknesses of the aerosol layer due to light scattering and light absorption, respectively, which can be expressed as follows (Kotchenruther et al., 1999):

231
$$\tau_s = M \times \alpha_s \times f(RH), \tau_a = M \times \alpha_a \tag{4}$$

- where M is the column burden of aerosol (unit: gm⁻²), α_s is the mass scattering efficiency (MSE), and α_a is the mass absorption efficiency (MAE). The direct radiative forcing is usually calculated with the assumption that the absorption enhancement is negligible, in comparison to the aerosol scattering enhancement (Xia et al., 2023).
- Hence, the dependence of ADRF on RH (i.e., $f_{RF}(RH)$) can be estimated by equation (5) (Chylek and Wong, 1995; Kotchenruther et al., 1999; L. Zhang et al., 2015):

238
$$f_{RF}(RH) = \frac{\Delta F_R(RH)}{\Delta F_R(dry)} = \frac{(1 - R_s)^2 \times \beta(RH) \times \alpha_s \times f(RH) - 2 \times R_s \times \alpha_a}{(1 - R_s)^2 \times \beta(dry) \times \alpha_s \times f(dry) - 2 \times R_s \times \alpha_a}$$
(5)

where the constant parameters used were $R_s = 0.15$, $\alpha_a = 0.3 \text{ m}^2 \cdot \text{g}^{-1}$ (Hand and Malm, 2007; Fierz-Schmidhauser et al., 2010). It should be noted that the assumed constant α_a might introduce some uncertainty in the calculated $f_{RF}(RH)$, given the fact that the contribution of absorption by brown carbon was unknown, although the mass fraction of BC in TSP remained almost constant (i.e., $4.6\% \pm 1.1\%$, Fig. S23) during the observation period. The parameter α_s was calculated by dividing $\sigma_{sca, 525}$ in the dry condition by the mass concentration of PM_{2.5} (i.e., $\alpha_s = \sigma_{sca, 525}$ / PM_{2.5}). β could be

calculated empirically from the measured HBF: $\beta = 0.0817 + 1.8495 \times HBF - 2.9682 \times HBF^2$ (Delene and Ogren, 2002).

Results of the offline chemical analysis with TSP filter samples are provided in S3. Given that the particle number and mass size distributions of components such as sulfate and organics from diverse emission sources were primarily concentrated within the submicron size range (An et al., 2024), the bulk chemical compositions of TSP could provide a reasonably good reference for the characterization of NPF and related optical and hygroscopic properties of PM_{2.5}. It should be noted that the corresponding mass fraction of some components (e.g., crustal materials) likely biased for larger particles. The simultaneous meteorological and air quality data can be found in S4.

3 Results and discussion

246

247

248

249

250

251

252

253

254

255

256

257

258

259

260

261

262

263

264

265

266

267

268

269

270

271

272

273

3.1 Overview of the aerosol optical hygroscopicity and PNSD measurements

Figure- 1 displayed the time series of the measured aerosol scattering coefficients, f(RH), PNSD, and the corresponding meteorological conditions and air pollutants during the study period. A sharp decrease in aerosol scattering coefficients and PM_{2.5}, accompanied with the continuous excellent visibility over 20 km was observed after August 6, indicating a markedly cleaner environment during P2 in comparison to P1 in summer 2022 of Chongqing. This could be largely attributed to the reduction in anthropogenic emissions (e.g., NO₂, CO₂, except SO₂) from limited outdoor activities influenced by the heatwaves in P2, as well as partly suspended industries and transportation to alleviate the power shortage issue (Chen et al., 2024). Notably, the increased wind speed and enhanced mixing layer height (MLH) also enabled a more favorable atmospheric diffusion condition in P2, facilitating the dilution of surface air pollutants (Zhang et al., 2008). However, a higher mass concentration of SO₂ was observed in the P2 period, likely due to a surge in electricity demand and resulted higher emissions from power plants operating almost at full capacity during the heatwave (Su, 2021; Teng et al., 2022). Moreover, significant discrepancies in the aerosol optical and hygroscopic properties were observed under different synoptic conditions (Table S2).

Both HBF and SAE were higher during the P2 period, aligning with the smaller $R_{\rm eff}$ (Table S2). The f(RH) was found to be largerrelatively higher (p < 0.05) in heatwave days, with the mean values of $1.6\underline{1} \pm 0.1\underline{2}$ and $1.7\underline{1} \pm 0.2\underline{15}$ during the P1 and P2 periods, respectively. Differently, ALWC was more abundant during the normally hot P1 period than the heatwave-dominated P2 period₅. This is likely due to that the derivation algorithm of ALWC utilized in this study (Kuang et al., 2018) was partly dependent on (e.g., positively correlated) the dry aerosol scattering coefficient, or rather the aerosol volume concentration in the dry condition (refer to Sect. S3 and Fig. S11 of the supplement). The mean $\sigma_{sca,525}$ for P2 was about 46.8% of that for the P1 period, and the corresponding mean level of ALWC was approximately 55.8% of that for P1. This partly agrees with the stronger aerosol optical hygroscopicity with a marginally higher f_W during the P2 period, highlighting a complex interaction between the optical enhancement and aerosol physicochemical properties.

The particle number size distribution data suggested that NPF events appeared in about half the number of observation days (Fig. 1i), with the an overall occurrance frequency of 52.4% (Fig. S4a) during the P2 period (53.8%) slightly higher than that of P1 (44.4%). This suggests the rather frequent summer NPF events in Chongqing, notably higher than those observed in other regions of the world, e.g., Beijing (16.7%, Deng et al., 2020; ~20%, Wang et al., 2013), Dongguan (4%, Tao et al., 2023), Hyytiälä (<40%, Dada et al., 2017) and LiLLE (<20%, Crumeyrolle et al., 2023). Moreover, the frequent NPF events during heatwaves formed substantially ultrafine particles that are of less contribution to aerosol optical properties in comparison to large particles, partially explaining the significantly lower levels of total scattering coefficients observed during the P2 period. It should be noted that the hourly $\sigma_{sca, 525}$ values during the P2 period were exclusively below 100 Mm⁻¹ (approximately the last 10th percentile of $\sigma_{sca, 525}$ data, regarded as the threshold value of relatively polluted cases; Fig. S2c), suggesting a much cleaner environment compared to the relatively polluted P1 period. Correspondingly, NPF events occurring during the relatively polluted P1 period (as detailed in section 3.2) were defined as NPF_P, while cases during the cleaner and heatwave-dominated P2 period were classified as NPF_{C, HW}.

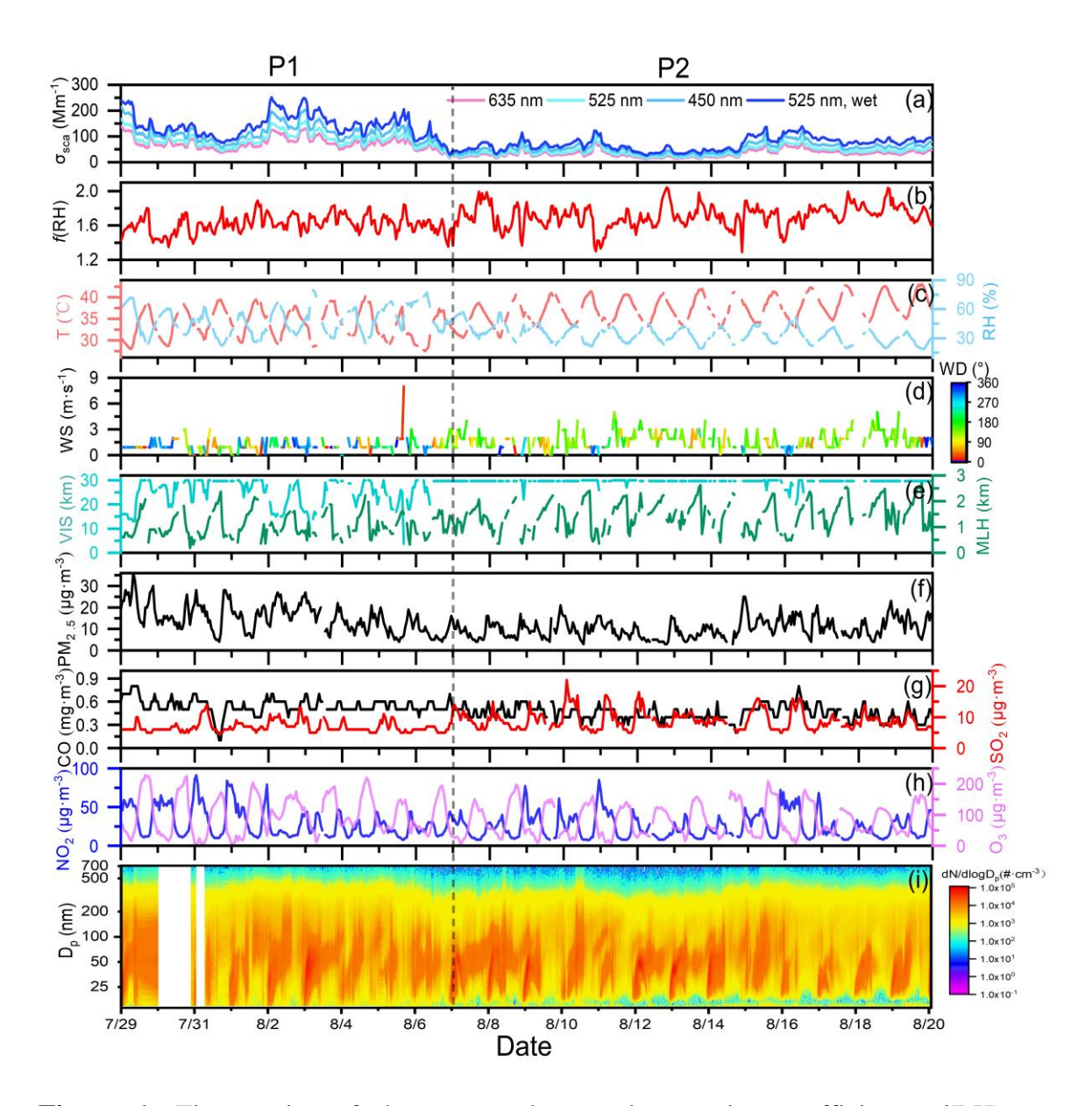
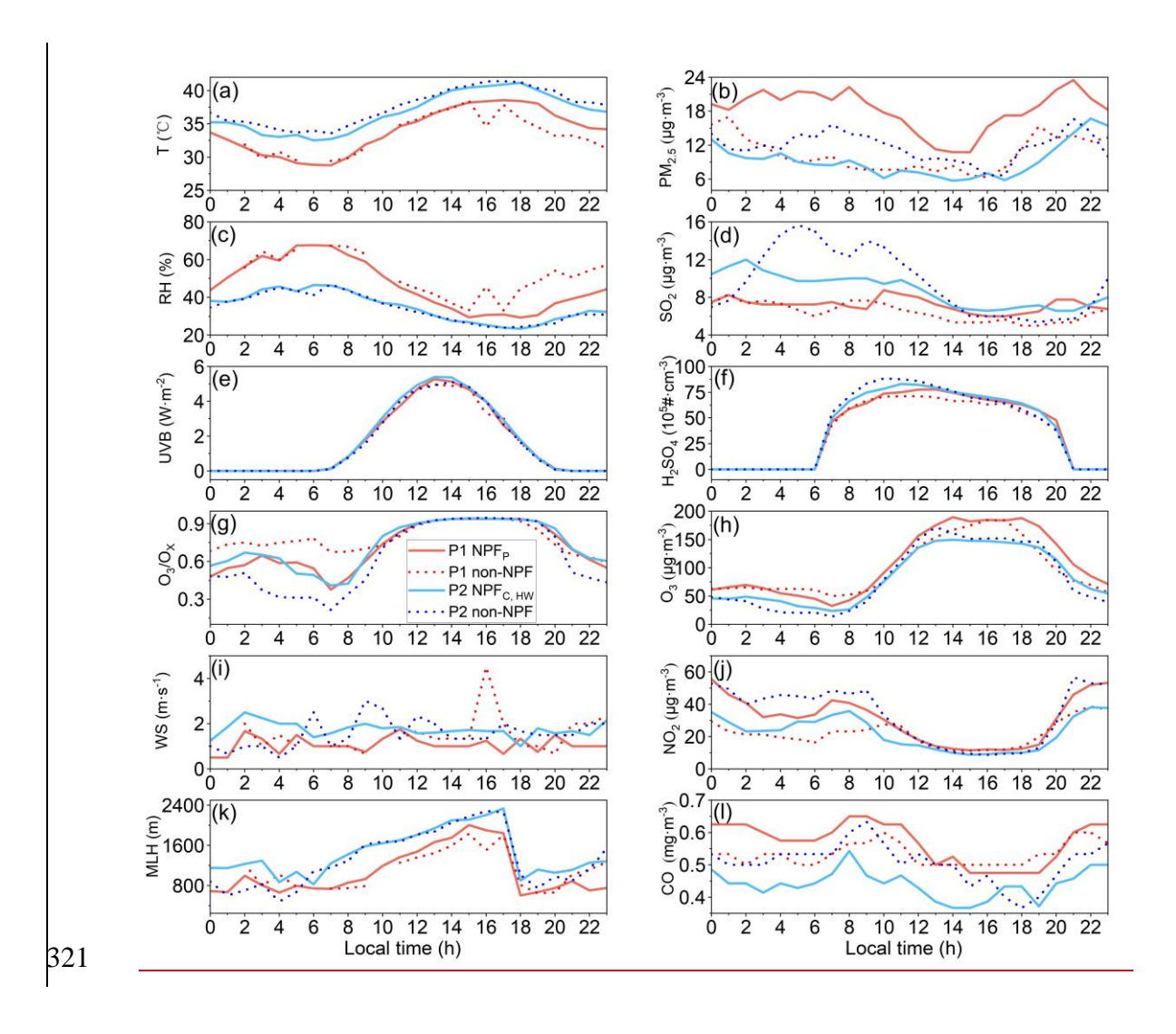


Figure 1. Time series of the measured aerosol scattering coefficients, f(RH), meteorological conditions, air pollutants, and particle number size distribution during the study period.

3.2 Characteristics of NPF events in different periods

Aside from gaseous precursors (e.g., SO₂, volatile organic compounds), meteorological conditions also play a key role in the occurrence of NPF events. In brief, NPF events are more likely to appear under sunny and clean conditions (Bousiotis et al., 2021; Crumeyrolle et al., 2023; Deng et al., 2021; Wang et al., 2017). The backward trajectory analysis revealed that the southerly breeze was predominant during the study period (Fig. S4b). Although the surface wind vector slightly varied between the P1 and

P2 periods, this consistency in air mass origins suggests that some other factors (e.g., changes in environmental conditions and emissions of gaseous precursors under heatwaves) could have played a crucial role in modulating NPF events. To further explore the characteristics of NPF events in different periods, the time-averaged diurnal variations of meteorological parameters and air pollutant concentrations during both NPF events and non-event days are presented in Fig. 2.



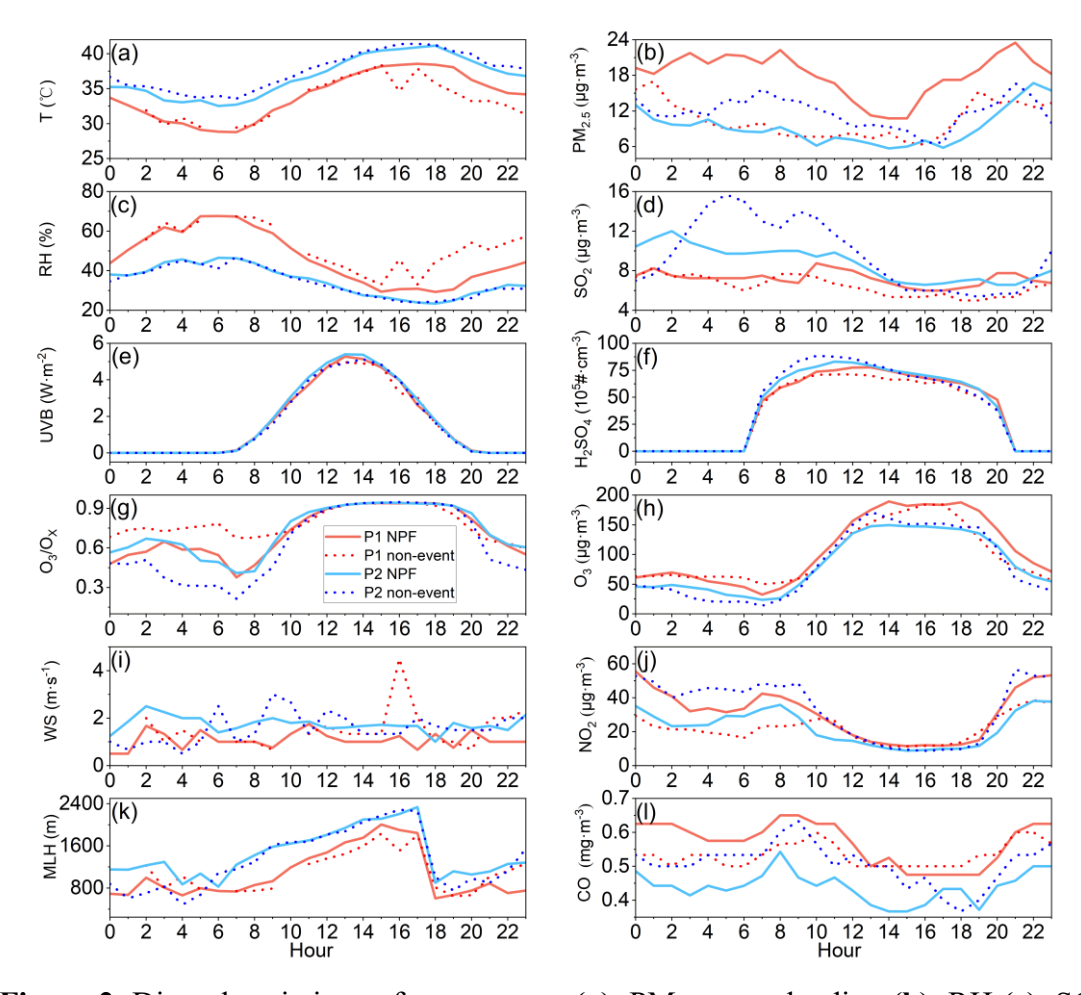


Figure 2. Diurnal variations of temperature (a), PM_{2.5} mass loading (b), RH (c), SO₂ (d), UVB (e), H₂SO₄ (f), O₃/O_X (g), O₃ (h), WS (i), NO₂ (j), MLH (k) and CO (l) during P1 (red) and P2 (blue) NPF events (solid line), as well as the corresponding non-event days (dash line).

As stated in Sect.3.1, NPF events during the P1 period tended to occur in relatively polluted environments compared to that of P2 NPF_{C. HW} events, as evidenced by the <u>frequent occurrence of higher $\sigma_{sea, 525} > 100 \text{ Mm}^{-1}$ </u>, increased air pollutant concentrations and lower visibility levels during P1 (Table S2, Fig. 1). <u>Additionally, the mean CS of the NPF_P events was above 0.015 s⁻¹ (Table S2), which could be considered as the "polluted" NPF cases (Shang et al., 2023). On P2 NPF_{C, HW} event days, the overall mean $\sigma_{sea, 525}$ was 33.2 ± 11.7 Mm⁻¹, decreased by 68.0% (39.3%) in comparison to that for P1 NPF_P event days (P2 non-event days). In addition, the mean PM_{2.5} concentration was even lower than 10.0 μ g·m⁻³, and the corresponding visibility level <u>was almost maintained at 30 km (Fig. 1e) was almost reaching the upper detection limit of 30 km</u>.</u>

All the above implies that the P2 NPF_{C, HW} events were generally accompanied with a much cleaner environment. It is notable that the increase in SO₂ concentration after 9:00 LT (Fig. 2d), along with the significant decrease in PM_{2.5} mass loadings thereby lowered CS or CoagS after 8:00 LT during P1 NPF_P events (Fig. 2b), likely favored the occurrence of NPF events. The higher gas-phase sulfuric acid (i.e., H₂SO₄, as estimated with the UVB and SO₂ concentration, Lu et al., 2019, S4) on the same NPF event-days (Fig. 2f), further suggesting that sulfuric acid concentration was a critical factor for the occurrence of P1 NPF_P events.

337

338

339

340

341

342

343

344

345

346

347

348

349

350

351

352

353

354

355

356

357

358

359

360

361

362

363

364

365

Meanwhile, tThe diurnal evolutions of meteorological conditions (e.g., T, RH, MLH) for NPF events were distinct between P1 and P2 periods, although relatively insignificant differences were observed for both NPF events and non-event days within a same period (Fig. 2). This mightlikely suggests that meteorological factors might not be the predominant determining factor of NPF occurrence during the heatwaves of 2022 summer in urban Chongqing, while NPF could be accompanied with quite different meteorological conditions depending on gaseous precursors and preexisting condensation sinks. For instance, the heatwave-influenced NPF_{C. HW} events were typically of clean-type NPF, characterized with lower background aerosol loading, higher temperature and favorable atmospheric dispersion capacity with the higher MLH. However, it is reported that excessive heat can increase the evaporation rate of critical acid-base clusters during the nucleation process and reduce the stability of initial molecular clusters (Bousiotis et al., 2021; Kurtén et al., 2007; Zhang et al., 2012), in line with a recent study that NPF events were weaker during heatwaves in Siberian boreal forest due to the unstable clusters (Garmash et al., 2024). On the other hand, the emission rate of biogenic VOCs (BVOCs, e.g., isoprene, monoterpene) from nearby plants and trees would decrease when temperature exceeded around 40 °C (Guenther et al., 1993; Pierce and Waldruff, 1991), despite that BVOCs plays a key role in the nucleation mechanism of NPF (Wang et al., 2017; Zhang et al., 2004). Hence, the even higher temperature (e.g., T >40 °C) likely hindered suppressed the occurrence nucleation processes and the subsequent growth of nucleation mode particles NPF during on P2

non-event days-of the P2 period (Fig. S6b2), in spite of higher concentrations of SO₂ and H₂SO₄.

366

367

368

369

370

371

372

373

374

375

376

377

378

379

380

381

382

383

384

385

386

387

388

389

390

391

392

393

394

395

To further investigate the effect of heatwave on NPF events, the diurnal variations of PNSD, Reff and particle mode diameter (D_{mode}) were shown in Fig. S6. aAerosol number and volume concentrations, as well as Reff, for different modes were illustrated in Fig. S47, and the relationship between temperature and the duration of NPF events was displayed in Fig. S58. The NPF events influenced byunder heatwaves usually initiated earlier (Fig. S58), with the number concentration of nucleation mode particles (N_{Nuc.}) in P2 NPF_{C, HW} cases peaked about an hour earlier (whilst relatively lower) in comparison to P1NPF_P event days (Fig. S47a). The D_{mode} on P2 NPF_{C, HW} days also reached its minimum earlier than that on P1 NPF_P days (Fig. S6). Since the sunrise and sunset time did not significantly vary within the study period (i.e., less than a half hour discrepancy), heatwaves likely provided more favorable conditions (e.g., enhanced volatile gaseous emissions, low RH; Bousiotis et al., 2021; Hamed et al., 2007; Wang et al., 2024) for the occurrence of NPF events in urban Chongqing. accelerate the attainment of the temperature threshold of NPF events, as This is supported evidenced by the earlier start time of NPF_{C, HW} start time corresponding to higher temperature ranges (Fig. S58). Furthermore, the end time of subsequent particle growth during P2 period was even later (i.e., $\sim 21:00$ LT) than that of P1 cases (Fig. S $\frac{58}{1}$). Given that the lower GR growth rates of new particles were generally lower during P2 NPF_{C, HW} events (Table S2), these explosively formed new particles could persist longer in the warmer atmosphere and probably undergo aging processes with a relatively higher oxidation degree. This is supported by the commonly higher ratios of secondary organic carbon (SOC) to organic carbon (OC) (i.e., SOC/OC >0.5) during the P2-NPF_{C, HW} event days (Fig. S23b). <u>In addition, aerosol R_{eff} was significantly smaller on the NPF_{C, HW} days</u> under heatwave conditions. The Reff and Dmode nearly kept at a same level below/approaching 50 nm during the subsequent growth on the P2 NPF_{C, HW} days, while the R_{eff} was generally above 50 nm and larger than D_{mode} for both P1 NPF_P cases and non-event days (Fig. S6). The diurnal patterns of aerosol volume concentrations for different size modes were similar to that of aerosol number concentrations during NPF

events (Fig. S47b1-b3). It is worth noting that However, both the R_{eff} of Aitken mode particles (R_{Ait.}) and accumulation mode particles (R_{Acc.}) were smaller during P2 NPF_C.

HW events than that of P1 NPF_P events (Fig. S47c2-c3), which may further influence size-dependent aerosol optical and hygroscopic properties (e.g., σ_{sca, 525}, HBF, SAE, f(RH)). The decrease in R_{Ait.} and R_{Acc.} during heatwaves could be attributed to three factors: (1) evaporation of the outer layer of particles and unstable clusters due to extremely high temperature heatwaves (Bousiotis et al., 2021; Cusack et al., 2013; Deng et al., 2020; Garmash et al., 2024; Li et al., 2019); (2) lower FR and GR of particles under athe cleaner environment (Table S2); (3) reduced emissions of larger primary particles during the P2 period.

3.3 Characteristics of the aerosol optical and hygroscopic properties duringon different types of NPF eventdays

Diurnal variations of the aerosol optical and hygroscopic parameters during different NPF event_days were shown in Fig. 3, and the corresponding results for non-event days can refer to Fig. S69. Generally, $\sigma_{sca, 525}$ possessed a similar bimodal diurnal pattern to that of the accumulation mode aerosol volume concentration (V_{Acc.}) (Fig. S47b3), as supported by the positive correlation between $\sigma_{sca, 525}$ and SMPS-measured aerosol volume concentration (Fig. S811). This is also consistent with the Mie theory, with a stronger increase in the scattering efficiency for accumulation mode particles (Titos et al., 2021). The diurnal pattern of $\sigma_{sca, 525}$ also varied distinctly between different NPF eventdays. Specifically, a minor peak of $\sigma_{sca, 525}$ around 12:00 LT (Fig. 3a) was influenced by the newly formed particles during P2 NPF_{C, HW} events, which contributed more significantly to the aerosol number and volume concentrations within 100 nm size ranges in prettymarkedly clean environments (Fig. S35c1, gc2). Instead of a noontime peak, $\sigma_{sca, 525}$ was observed with an early peak around the morning rush hours and a maximum value similarly occurred at the nighttime on P1 NPFp event-days.

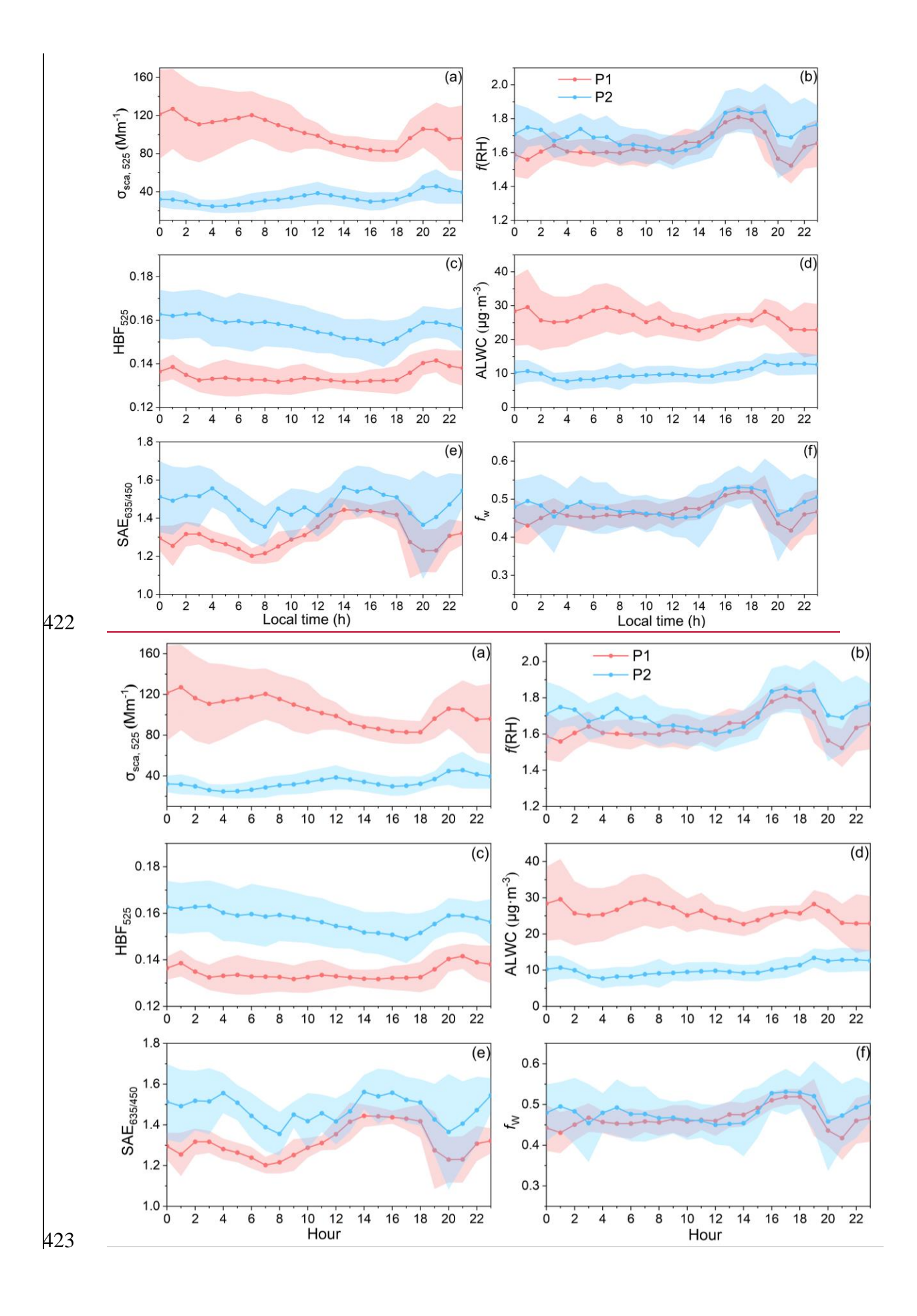


Figure 3. Diurnal variations of $\sigma_{sca, 525}$ (a), f(RH) (b), HBF₅₂₅ (c), ALWC (d), SAE_{635/450} (e) and f_W (f) on NPF event days during P1 (red line) and P2 (blue line) periods. The shaded areas stand for the corresponding $\pm 1\sigma$ standard deviations.

424

425

426

427

428

429

430

431

432

433

434

435

436

437

438

439

440

441

442

443

444

445

446

447

448

449

450

451

452

453

Both HBF and SAE during on P2 NPF_{C, HW} event days were significantly higher than that of P1 NPF_P cases (Fig. 3c, e), largely due to the smaller R_{eff} during P2 heatwave-dominated NPF events observed during heatwave-dominated period (Table S2). Moreover, the correlation between HBF (or SAE) and particle size in each mode was relatively weaker on NPF event days than on non-event days, especially for NPF_{C, HW}P2 NPF eventdays (Fig. S103). A strongest negative correlation was found between HBF and Reff of the accumulation mode in comparison to other modes, highlighting that HBF is more sensitive to the size distribution of accumulation mode particles (Collaud Coen et al., 2007). Given that NPF would largely enhance the abundance of both nucleation and Aitken mode aerosols, no significant variation in HBF was observed during the daytime due to the weakened correlation between HBF and RAcc. of NPF events. SAE is commonly used as an indicator of particle size distribution, almost decreasing monotonously with the increase of aerosol size within 1 μm (Kuang et al., 2017, 2018; Luoma et al., 2019). Accordingly, SAE decreased over the morning and evening rush hours when coarse particles (e.g., aged particles, road dust, automobile exhaust) generated during anthropogenic activities, accompanied with an increase in CO that is taken as the proxy for primary emissions (Fig. 21) (Yarragunta et al., 2020). On the contrary, the abundant ultrafine particles formed during NPF events led to a continuous increase in SAE during the day.

f(RH) exhibited a similar diurnal pattern on the P1 and P2 NPF event days (Fig. 3b). During the daytime, f(RH) remained relatively stable and gradually increased until peaking around 16:00-18:00 LT, with a generally higher f(RH) particularly after 15:00 LT during P2 NPF_{C, HW} eventdays than that of P1 cases. The insignificant fluctuation of relatively lower f(RH) levels before the noon could be attributed to the continuous development of the mixing layer (Fig. 2k), leading to an efficient mixing of particles in the nocturnal residual layer with anthropogenic emissions near the ground. Additionally, photochemical reactions in the afternoon facilitated the formation of more hygroscopic

secondary aerosols with a higher oxidation level (Liu et al., 2014; R. Zhang et al., 2015). The diurnal patterns of O₃ and the O₃/O_X ratio (i.e., an indicator of atmospheric oxidation capacity, where $O_X = O_3 + NO_2$, Tian et al., 2021) also showed similar trends (Fig. 2g, 2h). The presence of black carbon (BC) mixed with organic compounds (e.g., from traffic emissions and residential cooking activities) explained the rapid decrease in f(RH) during the evening rush hours (Liu et al., 2011). Furthermore, the daily mean f(RH) during for NPF event days was higher than that of non-event days (Table S2), particularly after the ending of NPF events around 12:00 LT. Given that newly formed particles were too small to significantly impact the total light scattering (Fig. S710), this indicates that the atmospheric conditions conducive to the occurrence of NPF may promote further growth (e.g., via photooxidation or atmospheric aging processes) of pre-existing particles and newly formed ones, leading to enhanced aerosol optical hygroscopicity as clued from the concurrent variations of ALWC and f_W in urban Chongqing during hot summer (Asmi et al., 2010; Wang et al., 2019; Wu et al., 2016). The diurnal pattern of ALWC closely mirrored the variation in $\sigma_{sca, 525}$, while f_W followed the similar evolution of f(RH). This suggests that ALWC was more sensitive to changes in the aerosol volume concentration, as determined by the corresponding retrieval algorithm (Kuang et al., 2018). The relatively higher fw levels were slightly higher during NPF days in comparison to that of non-event days (Table S2). This difference was more pronounced in the afternoon of NPF days (e.g., even exceeded 50% sometimes; Fig. 3f), verified the enhancement of aerosol hygroscopicity during NPF eventsthe subsequent growth and atmospheric aging of both pre-existing and newly formed particles in comparison to that of non-event days.

454

455

456

457

458

459

460

461

462

463

464

465

466

467

468

469

470

471

472

473

474

475

476

477

478

479

480

481

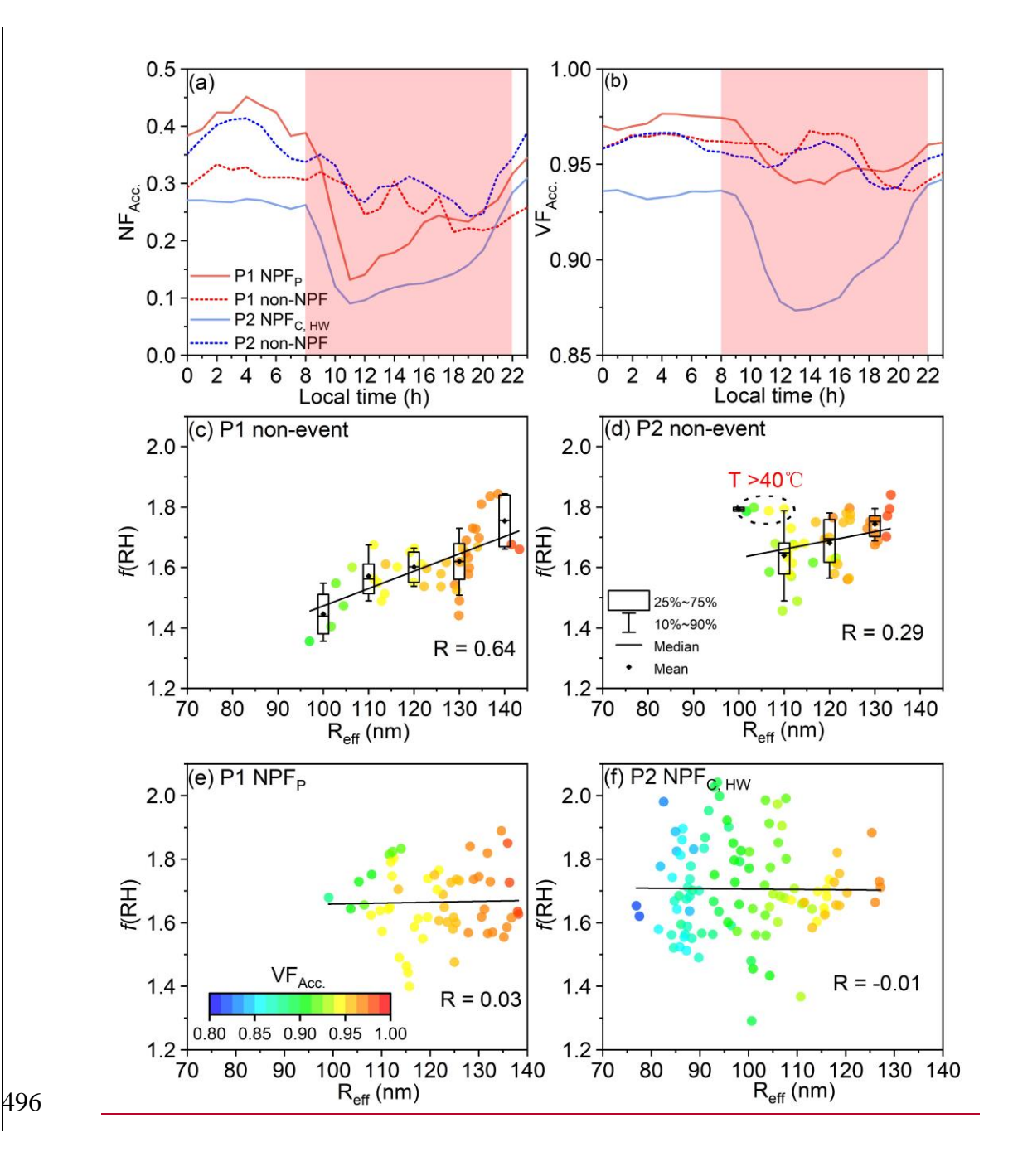
482

3.4 Heatwave-induced divergent changes in aerosol optical hygroscopicity

To further explore the impacts of heatwaves on *f*(RH) during diverse NPF events, data mainly within the time window of 08:00-22:00<u>LT</u> (i.e., typically covered the complete process of NPF and subsequent growth, while excluded higher RH conditions at night) were utilized for the following discussion.

A positive correlation between f(RH), R_{eff} and the volume fraction of accumulation

mode particles (VF_{Acc.}) was found on non-event days (Fig. 4c-d), when the aerosol size distribution was undisturbed by newly formed ultrafine particles and the corresponding VF_{Acc.} maintained around a relatively high level of 0.95 (Fig. 4a-b). The notably positive correlation between *f*(RH) and R_{eff} could be linked to the secondary formation of hygroscopic particles within the accumulation mode, primarily via photochemical reactions and further intensified by heatwaves during the non-event day particularly of the P2 period (Gu et al., 2023; Liu et al., 2014; R. Zhang et al., 2015; Zhang et al., 2024). Consequently, *f*(RH) at a specific R_{eff} was generally higher during the P2 period in comparison to that of P1 (Fig. 4c-d), also with high *f*(RH) levels observed for smaller size cases of R_{eff} <110 nm under some extremely high temperature conditions (T>40 °C, as highlighted by the red dashed circle in Fig. 4d). The higher SOC/OC on P2 non-event days further demonstrated the stronger secondary aerosol formation in comparison to P1 non-event days (Fig. S23b).



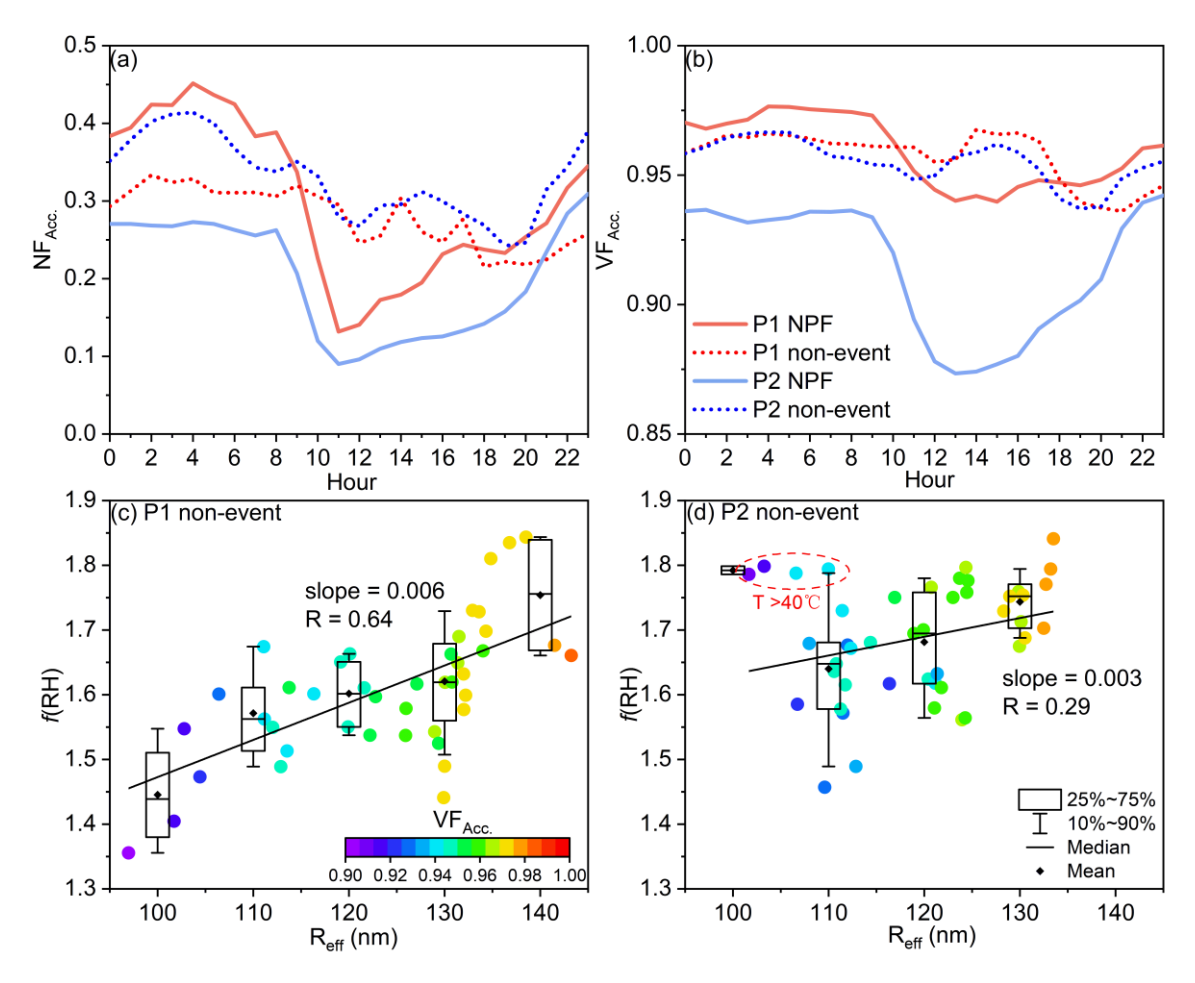


Figure 4. Diurnal variations of (a) the number fraction (NF_{Acc.}) and (b) volume fraction of accumulation mode particles (VF_{Acc.}) on P1 (red) and P2 (blue) NPF event days (solid line), as well as non-event days (dash line). The time window of 08:00-22:00 LT was shaded in red. The relationship of f(RH) with R_{eff} and VF_{Acc.} (as indicated by the colored dots) on P1 (c) and P2 non-event days (d), as well as on P1 (e) and P2 (f) NPF days during the 08:00-22:00 LT time window.

Nevertheless, *f*(RH) was almost independent of the two parameters (i.e., R_{eff} and VF_{Acc.}) for NPF events (Fig. S11a1-a24e-f). This is mainly due to the explosive formation of ultrafine particles and subsequent growth duringon NPF eventdays, significantly altering aerosol size distributions and inducing large fluctuations in the number and volume fractions of accumulation mode particles (as shaded in Fig. 4a-b). Therefore, characterizing *f*(RH) with the corresponding R_{eff} of aerosol populations was no longer applicable. Alternatively, SAE was commonly used to estimate or parameterize *f*(RH) (Titos et al., 2014; Xia et al., 2023; Xue et al., 2022), in line with

the similar diurnal patterns of f(RH) and SAE observed in this study. Figure 5 demonstrated a significantly positive correlation between f(RH) and SAE during NPF events in comparison to non-event days, with a similar slope of approximately 0.65 suggesting the consistent variation of f(RH) with SAE across both periods. As larger particles contributed higher to the aerosol volume concentrations (Fig. S35), the decrease of SAE also corresponded to an increase in $\sigma_{sca, 525}$ (Fig. 5a23, b23). In this sense Given that larger $\sigma_{sca, 525}$ values typically indicate the condition of a higher aerosol <u>loading</u>, f(RH) increased with SAE whereas decreased with $\sigma_{sca, 525}$, or rather the pollution level, during NPF eventdays. Meanwhile, tThe cleaner environment of P2 period generally possessed a lower CS (Table S2, as denoted by the size of circles in Fig. 5a2, b2), thereby in favor of the occurrence of NPF event. Such a positive (negative) correlation of f(RH) with SAE (CS) was more pronounced in heatwave-induced high temperature days during P2 period. Aerosol f(RH) and SAE exhibited a higher level on P2 NPF_{C, HW} days (as shown by the dash lines in Fig. 5), The possible reasons can be attributed to the following two aspects. One is related to the relatively smaller aerosol Ref (with a larger SAE) due to the lower FR and GR, likely influenced by the evaporation of newly-formed unstable clusters and particle coatings under heatwaves (Bousiotis et al., 2021; Cusack et al., 2013; Deng et al., 2020) during the subsequent growth of aerosols. Secondly, the higher temperature was normally associated with stronger photochemical oxidation, which could intensify the formation of secondary aerosol components with a higher hygroscopicity (Asmi et al., 2010; Gu et al., 2023; Liu et al., 2014; Wu et al., 2016; R. Zhang et al., 2015; Zhang et al., 2024). This is further supported by the relativeslightly higher levels of UVB (P1: $2.6 \pm 1.9 \ W \cdot m^{-2}$ versus P2: $2.7 \pm 2.0 \text{ W} \cdot \text{m}^{-2}$) and O_3/O_X (P1: 0.81 ± 0.17 versus P2: 0.82 ± 0.17) during P2 heatwave days, also in line with a recent study which demonstrated that heatwaves affected secondary organic aerosols (SOA) formation and aging by accelerating photooxidation in Beijing (Zhang et al., 2024). It is worth noting that f(RH) did not show a consistently higher level after the NPF_C. HW occurrence during P2 period, and it was slightly higher within the first few hours of NPF occurrence (i.e., ~ 12:00 -15:00 LT) during on P1 NPF_P event days (Fig. 3b). In fact,

512

513

514

515

516

517

518

519

520

521

522

523

524

525

526

527

528

529

530

531

532

533

534

535

536

537

538

539

540

aerosol optical hygroscopicity not fully corresponds to the bulk hygroscopicity primarily determined by aerosol chemical components, and the variability in aerosol optical features also plays a key role in f(RH). In this senseHence, the size-dependency of aerosol optical properties should be considered. The size-resolved $\sigma_{sca, 525}$ distribution and size-resolved cumulative frequency distribution (CFD) of $\sigma_{sca, 525}$ over different NPF eventsdays were calculated using the Mie theory, with good agreements between the theoretically calculated and measured $\sigma_{sca. 525}$ values (R² = 0.99). As shown in Fig. S710a and Fig. S912, new particles must grow into the accumulation mode size at least before they can exert a significant influence on the total scattering coefficient. The critical sizes corresponding to the cumulative frequency of 50% in $\sigma_{sca, 525}$ were 358.7 nm and 333.8 nm on P1 and P2 NPF days, respectively. This indicates that relatively smaller particles including the newly formed and grown ones mixed with preexisting and aged particles contributed a slightly higher portion to $\sigma_{sca, 525}$ during P2 NPF_{C, HW} events days, while the $\sigma_{sca, 525}$ of P1 NPF events was mainly contributed by larger particleones on P1 NPF_P days. Nevertheless, the Mie theory suggests that these smaller particles generally have a weaker enhancement in total scattering after hygroscopic growth, in comparison to larger size particles (Collaud Coen et al., 2007, Fig. S710a). Consequently, the changes in aerosol optical and hygroscopic properties necessitate consideration of both aerosol optical and chemical characteristics during different NPF events. Newly formed ultrafine particles contributed minor to aerosol optical properties The contribution of newly formed ultrafine particles to aerosol optical properties was insignificant within the first few hours of NPF occurrence, leading to a reduced enhancement in aerosol light scattering resulting in a lower f(RH) during the initial hours of P2 NPF_{C, HW} events compared to that of P1 NPF_P events (Fig. 3b), as evidenced characterized by a smaller Reff during for P2 NPF_{C, HW} events in comparison to P1 NPF events (Fig. S6). In contrast, the growth of pre-existing and newly formed particles into larger sizes would subsequently affect bulk aerosol optical properties, which was evidenced by the enhancement in aerosol extinction coefficient observed after NPF occurrence in a recent study (Sun et al., 2024). Specifically, particles could undergo a longer and more intensified photochemical aging process during NPF_{C, HW}

542

543

544

545

546

547

548

549

550

551

552

553

554

555

556

557

558

559

560

561

562

563

564

565

566

567

568

569

570

events as influenced by persistent heatwaves, which facilitated the secondary formation of hygroscopic aerosols and resulted in a higher *f*(RH) after 15:00 <u>LT</u> (Fig. 3b).

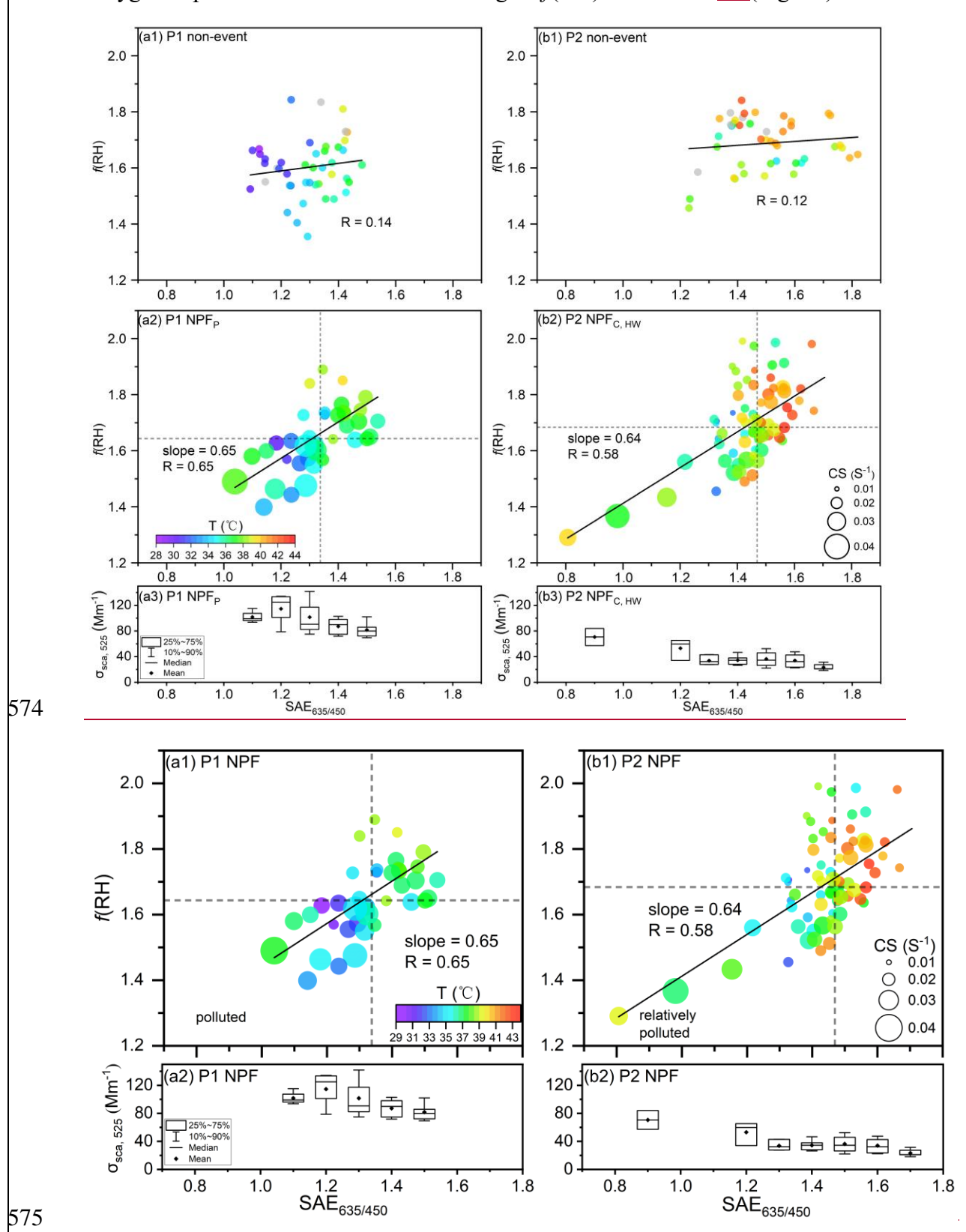


Figure 5. (a1) The relationship between f(RH) and $SAE_{635/450}$, as well as temperature (as indicated by the color of dots, missing values are represented in gray) and CS (as

576

denoted by the size of circles), on P1 non-event days (a1), NPF_P event days (a2) during the 08:00-22:00 LT time window. The vertical (horizontal) dash line represents the median value of SAE_{635/450} (f(RH)). (a23) The corresponding $\sigma_{sca, 525}$ under different SAE_{635/450} levels on P1 NPF_P event days. (b1-b23) The same but for P2 NPF event daysperiod.

3.5 f(RH)-induced changes in aerosol direct radiative forcing

The changes in f(RH) have significant implications for aerosol direct radiative forcing. Despite considerably lower $\sigma_{sca, 525}$ results during heatwaves, the corresponding mean $f_{RF}(RH)$ levels particularly for P2 NPF_{C. HW} event days were higher than that of the P1 cases (Fig. 6a). A robust positive correlation ($R^2 = 0.68$) was observed between f(RH) and aerosol radiative forcing enhancement factor, $f_{RF}(RH)$ (Fig. 6b). This is likely attributed to the enhanced $f_{RF}(RH)$ with the larger forward scattering ratio β , or rather higher HBF for smaller particle sizes, as supported by a generally negative correlation between $f_{RF}(RH)$ and $f_{RF}(RH)$ and $f_{RF}(RH)$ and $f_{RF}(RH)$ and $f_{RF}(RH)$ and $f_{RF}(RH)$ and $f_{RF}(RH)$ and smallest $f_{RF}(RH)$ is the highest $f_{RF}(RH)$ and $f_{RF}(RH)$ is the highest $f_{RF}(RH)$ and $f_{RF}(RH)$ is the highest $f_{RF}(RH)$ and $f_{RF}(RH)$ and $f_{RF}(RH)$ is the highest $f_{RF}(RH)$ and $f_{RF}(RH)$ and $f_{RF}(RH)$ is the highest $f_{RF}(RH)$ is the highest

The definition of *f*_{RF}(RH) in Eq.(5) implies the dependences of *f*_{RF}(RH) on both *f*(RH) and HBF-derived β(RH) and β(dry), or rather the ratio of HBF_{525, RH}/HBF₅₂₅. The mean HBF_{525, RH} was generally larger than HBF₅₂₅ in this study, specifically with the HBF_{525, RH}/HBF₅₂₅ ratios centered around 1.8 and even approached 2.5 on P2 NPF_{C, HW} event-days (Fig. 6c, Table S2). This could be different from the classical Mie theory with the spherical-particle premise, i.e., the observed light backscattering was enhanced after hydration likely resulted from the evolution in particle morphology that significantly influences their optical properties (Mishchenko 2009). The organic-rich particles might remain non-spherical even after water uptake due to the efficient evaporation of organic coatings under extremely hot weather conditions, as evidenced by a recent study that high temperature and RH conditions could accelerate the evaporation rate of SOA (Li et al., 2019). Meanwhile, Given that the backward scattering intensity of non-spherical particles is suggested to be much larger than its

spherical counterparts at scattering angles between 90° and 150° (Mishchenko 2009; 607 608 Yang et al., 2007) and that the HBF-derived asymmetry parameter (g) normally 609 correlates positively with the aerosol forward scattering (Andrews et al., 2006; Marshall 610 et al., 1995), the generally smaller g_{RH} results (in comparison to g) confirmed the 611 decrease (increase) in the forward (backward) light scattering after water uptake (Fig. 612 S10b), likely implying the change in the morphological structure of particles. This is 613 particularly evident for P2 NPF_{C, HW} days, with a much lower level of g_{RH} was observed 614 (Fig. S10b). Another possible reason is that although the abundant newly formed 615 particles were generally optically-insensitive, their contributions to $\sigma_{sca, 525}$ and 616 especially to σ_{bsca, 525} could be amplified upon humidification. Namely, even if these 617 hydrated particles remained small (e.g., below 100 nm), their HBF was significantly 618 higher than that of larger particles (Fig. S10a), thereby elevating the corresponding 619 HBF_{525, RH} levels during NPF events. Furthermore, ultrafine particles would 620 significantly contribute to both total light scattering and backscattering coefficients (Fig. 621 S7) after hygroscopic growth, if the aerosol population was large enough (e.g., during 622 NPF processes). These combined effects could potentially change particle morphology 623 and optical properties (e.g., elevated the HBF_{525, RH}) particularly during heatwave-624 influenced NPF_{C, HW} eventdays, characterized with the smallest aerosol R_{eff} (102.8 ± 625 12.4 nm) (Figure. S6), lowest number fraction of accumulation mode particles (0.20 \pm 626 0.10), and a higher SOC/OC ratio. The higher HBF₅₂₅, RH/HBF₅₂₅ ratios increased the 627 HBF-derived $\beta(RH)/\beta(dry)$ levels, in combination of the elevated f(RH), further 628 resulting in the highest $f_{RF}(RH)$ observed during P2 NPF_{C, HW} events. Given that 629 previously observed HBF_{525, RH} was typically lower than HBF₅₂₅ (Titos et al., 2021; Xia 630 et al., 2023; L. Zhang et al., 2015), the mean $f_{RF}(RH)$ results of this study ($f_{RF}(85\%)$) = 631 2.05 ± 0.24) were significantly higher than those observed in the Yangtze River Delta 632 $(f_{RF}(85\%) = 1.5, L. \text{ Zhang et al., } 2015), \text{ the North China Plain } (f_{RF}(80\%) = 1.6 \pm 0.2,$ 633 Xia et al., 2023), and some other regions in the world (Titos et al., 2021, Fig. 6d). It 634 should be noted that the reported $f_{RF}(RH)$ for the UGR site (Spain) was even higher, 635 likely due to the relatively larger HBF higher R_s and α_s used in the derivation of $f_{RF}(RH)$ 636 in that area (Titos et al., 2014; 2021).

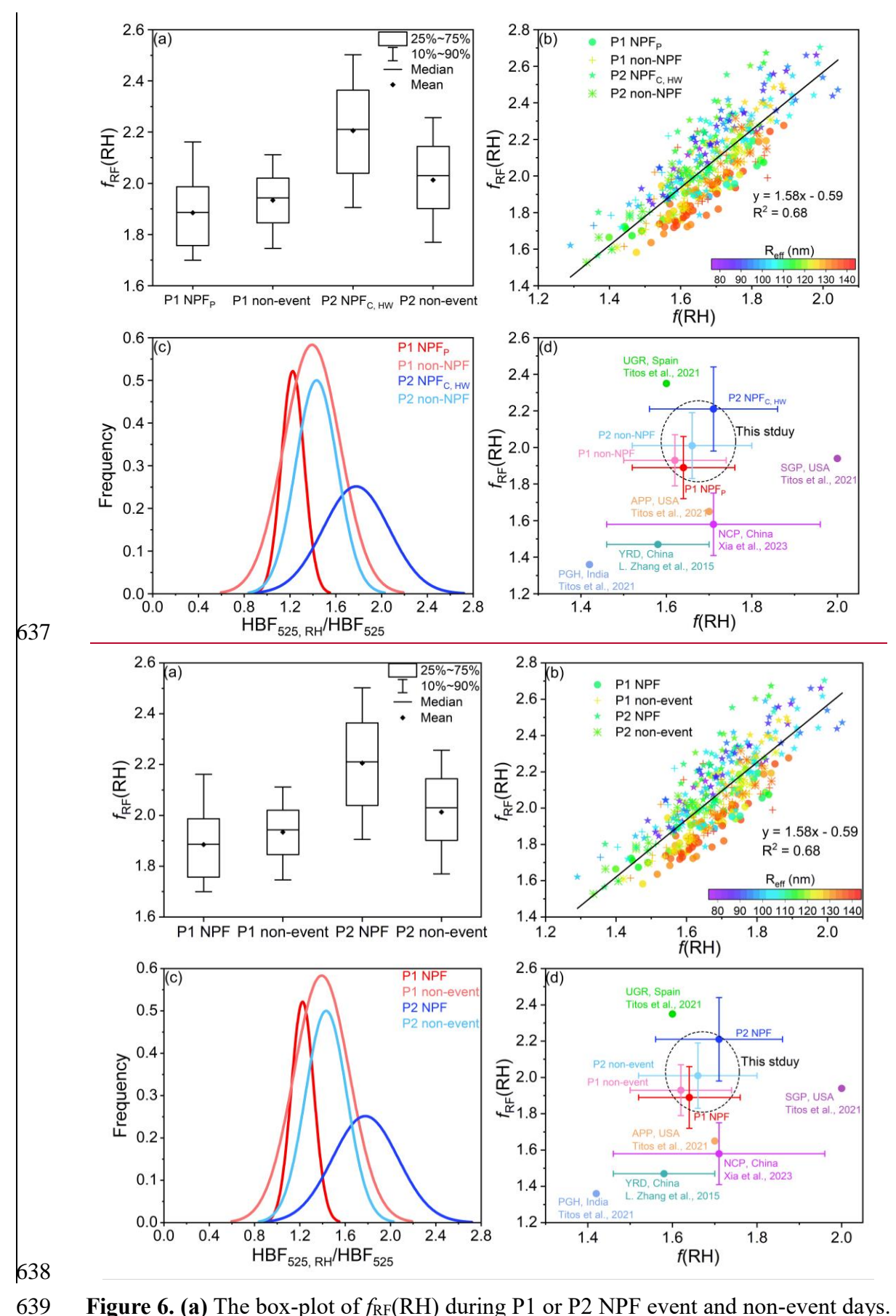


Figure 6. (a) The box-plot of $f_{RF}(RH)$ during P1 or P2 NPF event and non-event days. **(b)** The relationship between $f_{RF}(RH)$ and f(RH), as colored by the corresponding R_{eff} ,

during P1 or P2 NPF event—and non-event days (shown in different symbols). (c) Occurrence frequency of the ratio HBF_{525, RH}/HBF₅₂₅ ratios during P1 or P2 NPF event and non-event days. (d) The mean $f_{RF}(RH)$ under different f(RH) levels (the error bars stand for \pm one standard deviations corresponding to $f_{RF}(RH)$ and f(RH), respectively), along with the reported $f_{RF}(RH)$ and f(RH) data for other regions in the world.

641

642

643

644

645

646

647

648

649

650

651

652

653

654

655

656

657

658

659

660

661

662

663

664

665

666

667

668

669

670

A recent study has indicated that continuous reduction of PM_{2.5} mass loadings can increase the net solar radiation, thereby promoting NPF events (Zhao et al., 2021). Given the complexity and dynamic evolution of the atmospheric environment, these can further alter the intrinsic properties of aerosol particles (e.g., f(RH), HBF, morphology), potentially feeding back into aerosol-radiation interactions. Our findings suggest that NPF and growth events may elevate aerosol optical hygroscopicity in rather hot environments, e.g., the Basin area and tropical regions. Meanwhile, NPF serves as a crucial secondary transformation process in the atmosphere (Zhu et al., 2021). The favorable atmospheric diffusion capability ensured the mixing of newly formed particles into the upper boundary layer, where is colder and more humid than that near the surface during heatwaves (Jin et al., 2022). Hence, the enhancement of aerosol optical hygroscopicity during the subsequent growth of pre-existing and newly formed particles possibly exacerbates secondary pollution and even triggers haze events (Hao et al., 2024; Kulmala et al., 2021). On the other hand, a large number of studies have demonstrated that the new particles of higher hygroscopicity could contribute more to the activation of CCN (Ma et al., 2016; Ren et al., 2021; Rosati et al., 2022; Sun et al., 2024; Wu et al., 2015), thereby modulating the aerosol-cloud interactions and further the global climate (Ren et al., 2021; Sun et al., 2024; Wu et al., 2015Fan et al., 2016; Merikanto et al., 2006; Westervelt et al., 2013). Additionally, the simultaneous decrease in aerosol effective radius and possibly evaporation-induced non-spherical particle morphology further enhance the aerosol direct radiative forcing enhancement factor, potentially amplifying the cooling effect mainly caused by light scattering aerosols. This highlights the needs for further in-depth exploration on aerosol radiative impacts at weather extremes (e.g., heatwaves) with the changing climate, given the continuous reductions of anthropogenic emissions and more intense

emissions of biogenic origins with the global warming. Besides, more detailed information on the evolution of particle morphology with the changing environment (e.g., varied temperature and RH) would enrich insights into the aerosol radiative forcing.

4 Conclusions and implications

A rare heatwave event raged NPF events frequently occurred in throughout urban Chongqing of southwest China in the summer of 2022, accompanied withwhich significantly influenced aerosol physicochemical properties and atmospheric processes (e.g., NPF and subsequent growth) continuous heatwaves. Concurrent measurements of aerosol optical and hygroscopic properties, PNSD, and bulk chemical compositions were conducted to elucidate explore the mechanisms behind the variations in aerosol optical hygroscopicity during different NPF events under diverse weather conditions and non-event days.

NPF events exhibited distinct characteristics during the normally hot (P1, relatively polluted) and heatwaves-dominated (P2, quite clean) periods. NPF_P within P1 period was favored by the decrease in background aerosol loading and the higher abundance of H₂SO₄. NPF_{C, HW} events that occurred during the heatwave P2 period were characterized with relatively lower CS, CoagS, FR and GR, as well as a-smaller R_{eff} and D_{mode}, than P1 NPF_P cases. In comparison to the P1 NPF_P events, heatwaves initiated—NPF_{C, HW} occurred approximately one hour earlier and prolonged—the subsequent growth was longer during P2, likely intensifying the photochemical oxidation due to heatwave-indufluenced aging processes and modulating the evolution of aerosol size distributions differently.

Furthermore, significant differences in aerosol optical and hygroscopic properties were observed between the normally hot and heatwave-dominated NPF days. Heatwaves also significantly influenced the aerosol optical and hygroscopic properties. Distinct diurnal patterns of $\sigma_{sea, 525}$ were observed for different types of NPF events,

with aThe newly formed and grown particles mixed with pre-existing aerosols contributed a minor σ_{sca, 525} noontime peak occurred inon the much cleaner P2 NPF_C, HW days, while the σ_{sca, 525} instead of peaked earlier around the morning rush hours on P1 NPF_P event days. HBF and SAE were significantly higher on P2 NPF_{C, HW} event days, primarily due to the relatively smaller R_{eff} for heatwave-influenced NPF_{C, HW} cases. f(RH) remained relatively stable during the daytime of NPF event days and peaked around 16:00-18:00 LT₅. Specifically, aerosol optical hygroscopicity tended to be higher during the subsequent growth and aging of both pre-existing particles and newly formed ones on P2 NPF_{C, HW} days than that for P1 NPF_P days, likely due to the intensive photochemical reactions and accordingly enhanced formation of more hygroscopic secondary aerosols which aligned with the higher f_W levels. These secondary components could be more abundant due to heatwave induced stronger photooxidation, further resulting in a higher f(RH) particularly during the subsequent growth of pre-existing particles and newly formed ultrafine ones during P2 NPF_{C, HW} events in comparison to that of P1 NPF_P cases.

Compared with non-event cases, the generally higher levels of daily mean *f*(RH) suggested that the aerosol optical hygroscopicity was enhanced duringon NPF eventdays in hot summer of urban Chongqing. A significantly positive (negative) correlation between *f*(RH) and SAE (CS, σ_{sca, 525}, or rather the pollution level) was observed on NPF days for both periods, with a more pronounced correlation during heatwave influenced NPF events. accompanied by higher *f*(RH) and SAE values on NPF_{C, HW} days. This was likely due to the evaporation of both unstable clusters and particle coatings under heatwaves (Bousiotis et al., 2021; Cusack et al., 2013; Deng et al., 2020; Garmash et al., 2024), thereby reducing aerosol sizes (e.g., R_{eff}, D_{mode}) whereas increasing SAE. Moreover, heatwave-influenced stronger photooxidation enhanced the formation of more hygroscopic secondary components during the subsequent growth/aging processes of both pre-existing and newly formed particles on P2 NPF_{C, HW} days in comparison to that of P1 NPF_P cases. The aerosol light scattering or volume concentration was mainly contributed by the larger accumulation-mode particles, while more ultrafine particles dominated the size distribution especially for

the initial stage of heatwave-influenced NPF_{C, HW} events, further leading to a diminished aerosol scattering enhancement capabilitylower f(RH) following the NPF occurrence (i.e., ~ 12:00 -15:00 LT) in comparison to P1 NPF_P eventdays.

Changes in f(RH) havecould potentially impact significant implications for the aerosol direct radiative forcing. A robust positive (negative) correlation existed between $f_{RF}(RH)$ and f(RH) (R_{eff}). Despite a lower $\sigma_{sca, 525}$ during heatwaves, the corresponding mean $f_{RF}(RH)$ was relatively higher and the maximum value of $2.2\underline{1} \pm 0.2\underline{3}$ was observed on P2 NPF_{C, HW} event days, associated with the highest f(RH) ($1.7\underline{1} \pm 0.2\underline{13}$), smallest R_{eff} (102.8 ± 12.4 nm), and highest HBF₅₂₅, R_{H} /HBF₅₂₅ ratios ($1.8\underline{78} \pm 0.3\underline{29}$). The above highlights that heatwaves could influence the NPF and atmospheric processing (although with a decreased aerosol effective radius R_{eff} and D_{mode} likely due to evaporation-resulted non-spherical particle morphology under persistently high temperature conditions), thereby enhancing aerosol optical hygroscopic growth and potentially reducing the net solar radiation directly especially in hot summer. Further explorations on detailed molecular-scale characterizations (e.g., molecular structures and compositions of newly and secondary formed particles, as well as particle morphology) and aerosol radiative impacts including the aerosol-cloud interactions of weather extremes (e.g., heatwaves) with the changing climate are highly recommended.

Data availability. Data will be available upon request.

Author contributions. YH and PL: Methodology, Investigation, Data analysis, Formal analysis, Visualization, Validation, Writing – original draft & editing. YG and ZW: Methodology, Investigation, Formal analysis. MT, YC, HX and WH: Data curation, Methodology. FW and YL: Investigation. YK: Methodology, Data analysis, Writing – review & editing. JC: Conceptualization, Methodology, Funding acquisition, Data curation, Writing – review & editing, Supervision.

- 757 **Competing interests.** The authors declare no competing financial interest.
- 758
- 759 **Acknowledgement.** This work was supported by the National Natural Science
- 760 Foundation of China (No. 42105075), Venture and Innovation Support Program for
- 761 Chongqing Overseas Returnees (No. cx2021021). We thank Biao Xue for the
- 762 technical support on the utilization and maintenance of the humidified
- nephelometer system. We also thank Ziqian Wang for the TSP filter sample
- 764 collection and Jiawei Zhou for the corresponding offline chemical analysis.
- 765

766

References

- 767 An, J., Lu, Y., Huang, D. D., Ding, X., Hu, Q., Yan, R., Qiao, L., Zhou, M., Huang, C.,
- Wang, H., Fu, Q., Yu, F., and Wang, L.: Sectoral Size Resolved Particle Number
- 769 Emissions With Speciation: Emission Profile Based Quantification and a Case Study
- 770 in the Yangtze River Delta Region, China, J. Geophys. Res. Atmos., 1-22,
- 771 https://doi.org/10.1029/2024JD041234, 2024.
- Andrews, E., Sheridan, P. J., Fiebig, M., McComiskey, A., Ogren, J. A., Arnott, P.,
- Covert, D., Elleman, R., Gasparini, R., Collins, D., Jonsson, H., Schmid, B., and Wang,
- J.: Comparison of methods for deriving aerosol asymmetry parameter, J. Geophys. Res.
- 775 Atmos., 111, 1–16, https://doi.org/10.1029/2004JD005734, 2006.
- Asmi, E., Frey, A., Virkkula, A., Ehn, M., Manninen, H. E., Timonen, H., Tolonen-
- Kivimaki, O., Aurela, M., Hillamo, R., and Kulmala, M.: Hygroscopicity and chemical
- composition of antarctic sub-micrometre aerosol particles and observations of new
- particle formation, Atmos. Chem. Phys., 10, 4253–4271, https://doi.org/10.5194/acp-
- 780 10-4253-2010, 2010.
- 781 <u>Bae, M. S., Lee, T., Schauer, J. J., Park, G., Son, Y. B., Kim, K. H., Cho, S. S., Park, S.</u>
- 782 S., Park, K., and Shon, Z. H.: Chemical Characteristics of Size-Resolved Aerosols in
- Coastal Areas during KORUS-AQ Campaign; Comparison of Ion Neutralization Model,

- Asia-Pacific J. Atmos. Sci., 55, 387–399, https://doi.org/10.1007/s13143-018-00099-1,
- 785 **2019**.
- 786 Bousiotis, D., Brean, J., Pope, F. D., Dall'Osto, M., Querol, X., Alastuey, A., Perez, N.,
- Petäjä, T., Massling, A., Klenø Nøjgaard, J., Nordstrøm, C., Kouvarakis, G., Vratolis,
- 788 S., Eleftheriadis, K., Niemi, J. V., Portin, H., Wiedensohler, A., Weinhold, K., Merkel,
- 789 M., Tuch, T., and Harrison, R. M.: The effect of meteorological conditions and
- atmospheric composition in the occurrence and development of new particle formation
- 791 (NPF) events in Europe, Atmos. Chem. Phys., 21, 3345–3370,
- 792 https://doi.org/10.5194/acp-21-3345-2021, 2021.
- 793 Brooke Anderson, G. and Bell, M. L.: Heat waves in the United States: Mortality risk
- during heat waves and effect modification by heat wave characteristics in 43 U.S.
- 795 communities, Environ. Health Perspect., 119, 210–218,
- 796 https://doi.org/10.1289/ehp.1002313, 2011.
- 797 Chen, J., Zhao, C. S., Ma, N., and Yan, P.: Aerosol hygroscopicity parameter derived
- 798 from the light scattering enhancement factor measurements in the North China Plain,
- 799 Atmos. Chem. Phys., 14, 8105–8118, https://doi.org/10.5194/acp-14-8105-2014, 2014.
- 800 Chen, Q., Mu, Z., Song, W., Wang, Y., Yang, Z., Zhang, L., and Zhang, Y. L.: Size-
- 801 Resolved Characterization of the Chromophores in Atmospheric Particulate Matter
- From a Typical Coal-Burning City in China, J. Geophys. Res. Atmos., 124, 10546–
- 803 10563, https://doi.org/10.1029/2019JD031149, 2019.
- Chen, T., Wang, T., Xue, L., and Brasseur, G.: Heatwave exacerbates air pollution in
- 805 China through intertwined climate-energy-environment interactions, Sci. Bull., 69,
- 806 <u>2765–2775</u>, https://doi.org/10.1016/j.scib.2024.05.018, 2024.
- 807 China Meteorological Administration, 2022. China Climate Bulletin 2022.
- 808 https://www.cma.gov.cn/zfxxgk/gknr/qxbg/202303/t20230324_5396394.html.
- Accessed on 23 March 2023. (in Chinese).

- 810 Cho Cheung, H., Chung-Kuang Chou, C., Siu Lan Lee, C., Kuo, W. C., and Chang, S.
- 811 C.: Hygroscopic properties and cloud condensation nuclei activity of atmospheric
- aerosols under the influences of Asian continental outflow and new particle formation
- 813 at a coastal site in eastern Asia, Atmos. Chem. Phys., 20, 5911-5922,
- 814 https://doi.org/10.5194/acp-20-5911-2020, 2020.
- 815 Chylek, P. and Wong, J.: Effect of absorbing aerosols on global radiation budget,
- 816 Geophys. Res. Lett., 22, 929–931, https://doi.org/10.1029/95GL00800, 1995.
- 817 Collaud Coen, M., Weingartner, E., Nyeki, S., Cozic, J., Henning, S., Verheggen, B.,
- 818 Gehrig, R., and Baltensperger, U.: Long-term trend analysis of aerosol variables at the
- 819 high-alpine site Jungfraujoch, J. Geophys. Res. Atmos., 112,
- 820 https://doi.org/10.1029/2006JD007995, 2007.
- 821 Covert, D. S., Charlson, R. J., and Ahlquist, N. C.: A Study of the Relationship of
- 822 Chemical Composition and Humidity to Light Scattering by Aerosols, J. Appl.
- 823 Meteorol., 11, 968–976, https://doi.org/10.1175/1520-
- 824 0450(1972)011<0968:asotro>2.0.co;2, 1972.
- 825 Crumeyrolle, S., Kontkanen, J. S. S., Rose, C., Velazquez Garcia, A., Bourrianne, E.,
- 826 Catalfamo, M., Riffault, V., Tison, E., Ferreira De Brito, J., Visez, N., Ferlay, N., Auriol,
- 827 F., and Chiapello, I.: Measurement report: Atmospheric new particle formation at a
- 828 peri-urban site in Lille, northern France, Atmos. Chem. Phys., 23, 183-201,
- 829 https://doi.org/10.5194/acp-23-183-2023, 2023.
- 830 Cusack, M., Alastuey, A., and Querol, X.: Case studies of new particle formation and
- 831 evaporation processes in the western Mediterranean regional background, Atmos.
- 832 Environ., 81, 651–659, https://doi.org/10.1016/j.atmosenv.2013.09.025, 2013.
- Dada, L., Paasonen, P., Nieminen, T., Buenrostro Mazon, S., Kontkanen, J., Peräkylä,
- O., Lehtipalo, K., Hussein, T., Petäjä, T., Kerminen, V. M., Bäck, J., and Kulmala, M.:
- 835 Long-term analysis of clear-sky new particle formation events and nonevents in

- 836 Hyytiälä, Atmos. Chem. Phys., 17, 6227–6241, https://doi.org/10.5194/acp-17-6227-
- 837 2017, 2017.
- Dal Maso, M., Kulmala, M., Riipinen, I., Wagner, R., Hussein, T., Aalto, P. P., and
- Lehtinen, K. E. J.: Formation and growth of fresh atmospheric aerosols: Eight years of
- aerosol size distribution data from SMEAR II, Hyytiälä, Finland, Boreal Environ. Res.,
- 841 10, 323–336, 2005.
- Delene, D. J. and Ogren, J. A.: Variability of aerosol optical properties at four North
- 843 American surface monitoring sites, J. Atmos. Sci., 59, 1135–1150,
- 844 https://doi.org/10.1175/1520-0469(2002)059<1135:VOAOPA>2.0.CO;2, 2002.
- Deng, C., Cai, R., Yan, C., Zheng, J., and Jiang, J.: Formation and growth of sub-3 nm
- particles in megacities: Impact of background aerosols, Faraday Discuss., 226, 348–
- 847 363, https://doi.org/10.1039/d0fd00083c, 2021.
- 848 Deng, C., Fu, Y., Dada, L., Yan, C., Cai, R., Yang, D., Zhou, Y., Yin, R., Lu, Y., Li,
- X., Qiao, X., Fan, X., Nie, W., Kontkanen, J., Kangasluoma, J., Chu, B., Ding, A.,
- Kerminen, V. M., Paasonen, P., Worsnop, D. R., Bianchi, F., Liu, Y., Zheng, J., Wang,
- 851 L., Kulmala, M., and Jiang, J.: Seasonal characteristics of new particle formation and
- 852 growth in urban Beijing, Environ. Sci. Technol., 54, 8547–8557,
- 853 https://doi.org/10.1021/acs.est.0c00808, 2020.
- 854 Duan, J., Huang, R. J., Wang, Y., Xu, W., Zhong, H., Lin, C., Huang, W., Gu, Y.,
- Ovadnevaite, J., Ceburnis, D., and O'Dowd, C.: Measurement report: Size-resolved
- secondary organic aerosol formation modulated by aerosol water uptake in wintertime
- haze, Atmos. Chem. Phys., 24, 7687–7698, https://doi.org/10.5194/acp-24-7687-2024,
- 858 2024.
- 859 Fan, J., Wang, Y., Rosenfeld, D., and Liu, X.: Review of aerosol-cloud interactions:
- Mechanisms, significance, and challenges, J. Atmos. Sci., 73, 4221–4252,
- 861 <u>https://doi.org/10.1175/JAS-D-16-0037.1, 2016.</u>

- 862 Fierz-Schmidhauser, R., Zieger, P., Gysel, M., Kammermann, L., Decarlo, P. F.,
- Baltensperger, U., and Weingartner, E.: Measured and predicted aerosol light scattering
- 864 enhancement factors at the high alpine site Jungfraujoch, Atmos. Chem. Phys, 10,
- 865 2319–2333, 2010.
- Garmash, O., Ezhova, E., Arshinov, M., Belan, B., Lampilahti, A., Davydov, D., Räty,
- M., Aliaga, D., Baalbaki, R., Chan, T., Bianchi, F., Kerminen, V. M., Petäjä, T., and
- Kulmala, M.: Heatwave reveals potential for enhanced aerosol formation in Siberian
- boreal forest, Environ. Res. Lett., 19, https://doi.org/10.1088/1748-9326/ad10d5, 2024.
- 870 Gu, Y., Huang, R. J., Duan, J., Xu, W., Lin, C., Zhong, H., Wang, Y., Ni, H., Liu, Q.,
- Xu, R., Wang, L., and Li, Y. J.: Multiple pathways for the formation of secondary
- organic aerosol in the North China Plain in summer, Atmos. Chem. Phys., 23, 5419—
- 873 5433, https://doi.org/10.5194/acp-23-5419-2023, 2023.
- Guenther, A. B., Monson, R. K., and Fall, R.: Isoprene and monoterpene emission rate
- variability: Observations with eucalyptus and emission rate algorithm development, J.
- 876 Geophys. Res. Atmos., 96, 10799–10808, https://doi.org/10.1029/91jd00960, 1991.
- 677 Guo, X., Huang, J., Luo, Y., Zhao, Z., and Xu, Y.: Projection of heat waves over China
- for eight different global warming targets using 12 CMIP5 models, Theor. Appl.
- 879 Climatol., 128, 507–522, https://doi.org/10.1007/s00704-015-1718-1, 2016.
- Hamed, A., Joutsensaari, J., Mikkonen, S., Sogacheva, L., Dal Maso, M., Kulmala, M.,
- Cavalli, F., Fuzzi, S., Facchini, M. C., Decesari, S., Mircea, M., Lehtinen, K. E. J., and
- Laaksonen, A.: Nucleation and growth of new particles in Po Valley, Italy, Atmos.
- 883 Chem. Phys., 7, 355–376, https://doi.org/10.5194/acp-7-355-2007, 2007.
- Hamed, A., Korhonen, H., Sihto, S. L., Joutsensaari, J., Jrvinen, H., Petäjä, T., Arnold,
- F., Nieminen, T., Kulmala, M., Smith, J. N., Lehtinen, K. E. J., and Laaksonen, A.: The
- role of relative humidity in continental new particle formation, J. Geophys. Res. Atmos.,
- 887 116, 1–12, https://doi.org/10.1029/2010JD014186, 2011.

- Hand, J. L. and Malm, W. C.: Review of aerosol mass scattering efficiencies from
- 889 ground-based measurements since 1990, J. Geophys. Res. Atmos., 112,
- 890 https://doi.org/10.1029/2007JD008484, 2007.
- Hao, Y., Gou, Y., Wang, Z., Huang, W., Wan, F., Tian, M., and Chen, J.: Current
- challenges in the visibility improvement of urban Chongqing in Southwest China: From
- the perspective of PM2.5-bound water uptake property over 2015–2021, Atmos. Res.,
- 894 300, 107215, https://doi.org/10.1016/j.atmosres.2023.107215, 2024.
- Hao, Z., Chen, Y., Feng, S., Liao, Z., An, N., and Li, P.: The 2022 Sichuan-Chongqing
- spatio-temporally compound extremes: a bitter taste of novel hazards, Sci. Bull., 68,
- 897 1337–1339, https://doi.org/10.1016/j.scib.2023.05.034, 2023.
- Hauser, M., Orth, R., and Seneviratne, S. I.: Role of soil moisture versus recent climate
- change for the 2010 heat wave in western Russia, Geophys. Res. Lett., 43, 2819–2826,
- 900 https://doi.org/10.1002/2016GL068036, 2016.
- 901 Jefferson, A., Hageman, D., Morrow, H., Mei, F., and Watson, T.: Seven years of
- aerosol scattering hygroscopic growth measurements from SGP: Factors influencing
- 903 water uptake, J. Geophys. Res. Atmos., 122, 9451–9466,
- 904 https://doi.org/10.1002/2017JD026804, 2017.
- 905 Jin, X., Li, Z., Wu, T., Wang, Y., Cheng, Y., Su, T., Wei, J., Ren, R., Wu, H., Li, S.,
- 206 Zhang, D., and Cribb, M.: The different sensitivities of aerosol optical properties to
- particle concentration, humidity, and hygroscopicity between the surface level and the
- 908 upper boundary layer in Guangzhou, China, Sci. Total Environ., 803, 150010,
- 909 https://doi.org/10.1016/j.scitotenv.2021.150010, 2022.
- 910 Kerminen, V. M., Chen, X., Vakkari, V., Petäjä, T., Kulmala, M., and Bianchi, F.:
- 911 Atmospheric new particle formation and growth: Review of field observations, Environ.
- 912 Res. Lett., 13, https://doi.org/10.1088/1748-9326/aadf3c, 2018.

- Kim, N., Yum, S. S., Park, M., Park, J. S., Shin, H. J., and Ahn, J. Y.: Hygroscopicity
- of urban aerosols and its link to size-resolved chemical composition during spring and
- 915 summer in Seoul, Korea, Atmos. Chem. Phys., 20, 11245–11262,
- 916 https://doi.org/10.5194/acp-20-11245-2020, 2020.
- 917 Kotchenruther, R. A., Hobbs, P. V., and Hegg, D. A.: Humidification factors for
- atmospheric aerosols off the mid-Atlantic coast of the United States, J. Geophys. Res.
- 919 Atmos., 104, 2239–2251, https://doi.org/10.1029/98JD01751, 1999.
- 920 Kuang, Y., He, Y., Xu, W., Zhao, P., Cheng, Y., Zhao, G., Tao, J., Ma, N., Su, H.,
- Page 21 Zhang, Y., Sun, J., Cheng, P., Yang, W., Zhang, S., Wu, C., Sun, Y., and Zhao, C.:
- 922 Distinct diurnal variation in organic aerosol hygroscopicity and its relationship with
- 923 oxygenated organic aerosol, Atmos. Chem. Phys., 20, 865–880,
- 924 https://doi.org/10.5194/acp-20-865-2020, 2020.
- 925 Kuang, Y., Zhao, C. S., Zhao, G., Tao, J. C., Xu, W., Ma, N., and Bian, Y. X.: A novel
- 926 method for calculating ambient aerosol liquid water content based on measurements of
- 927 a humidified nephelometer system, Atmos. Meas. Tech., 11, 2967–2982,
- 928 https://doi.org/10.5194/amt-11-2967-2018, 2018.
- 929 Kuang, Y., Zhao, C., Tao, J., Bian, Y., Ma, N., and Zhao, G.: A novel method for
- 930 deriving the aerosol hygroscopicity parameter based only on measurements from a
- 931 humidified nephelometer system, Atmos. Chem. Phys., 17, 6651–6662,
- 932 https://doi.org/10.5194/acp-17-6651-2017, 2017.
- 833 Kulmala, M., Dada, L., Daellenbach, K. R., Yan, C., Stolzenburg, D., Kontkanen, J.,
- Ezhova, E., Hakala, S., Tuovinen, S., Kokkonen, T. V., Kurppa, M., Cai, R., Zhou, Y.,
- 935 Yin, R., Baalbaki, R., Chan, T., Chu, B., Deng, C., Fu, Y., Ge, M., He, H., Heikkinen,
- 936 L., Junninen, H., Liu, Y., Lu, Y., Nie, W., Rusanen, A., Vakkari, V., Wang, Y., Yang, G.,
- 937 Yao, L., Zheng, J., Kujansuu, J., Kangasluoma, J., Petaja, T., Paasonen, P., Jarvi, L.,
- Worsnop, D., Ding, A., Liu, Y., Wang, L., Jiang, J., Bianchi, F., and Kerminen, V. M.:
- 939 Is reducing new particle formation a plausible solution to mitigate particulate air

- pollution in Beijing and other Chinese megacities?, Faraday Discuss., 226, 334–347,
- 941 https://doi.org/10.1039/d0fd00078g, 2021.
- 842 Kulmala, M., Petäjä, T., Nieminen, T., Sipilä, M., Manninen, H. E., Lehtipalo, K., Dal
- 943 Maso, M., Aalto, P. P., Junninen, H., Paasonen, P., Riipinen, I., Lehtinen, K. E. J.,
- Laaksonen, A., and Kerminen, V. M.: Measurement of the nucleation of atmospheric
- 945 aerosol particles, Nat. Protoc., 7, 1651–1667, https://doi.org/10.1038/nprot.2012.091,
- 946 2012.
- 947 Kulmala, M.: How Particles Nucleate and Grow, Science, 302, 1000-1001,
- 948 https://doi.org/10.1126/science.1090848, 2003.
- 949 Kurtén, T., Torpo, L., Ding, C. G., Vehkamäki, H., Sundberg, M. R., Laasonen, K., and
- 950 Kulmala, M.: A density functional study on water-sulfuric acid-ammonia clusters and
- 951 implications for atmospheric cluster formation, J. Geophys. Res. Atmos., 112, 1–7,
- 952 https://doi.org/10.1029/2006JD007391, 2007.
- Li, Y., Ding, Y., and Li, W.: Observed trends in various aspects of compound heat waves
- 954 across China from 1961 to 2015, J. Meteorol. Res., 31, 455–467,
- 955 https://doi.org/10.1007/s13351-017-6150-2, 2017.
- 956 Li, Z., Tikkanen, O. P., Buchholz, A., Hao, L., Kari, E., Yli-Juuti, T., and Virtanen, A.:
- 957 Effect of Decreased Temperature on the Evaporation of α-Pinene Secondary Organic
- 958 Aerosol Particles, ACS Earth Sp. Chem., 3, 2775–2785,
- 959 https://doi.org/10.1021/acsearthspacechem.9b00240, 2019.
- Liu, H. J., Zhao, C. S., Nekat, B., Ma, N., Wiedensohler, A., Van Pinxteren, D., Spindler,
- 961 G., Müller, K., and Herrmann, H.: Aerosol hygroscopicity derived from size-segregated
- chemical composition and its parameterization in the North China Plain, Atmos. Chem.
- 963 Phys., 14, 2525–2539, https://doi.org/10.5194/acp-14-2525-2014, 2014.
- Liu, P. F., Zhao, C. S., Göbel, T., Hallbauer, E., Nowak, A., Ran, L., Xu, W. Y., Deng,
- 965 Z. Z., Ma, N., Mildenberger, K., Henning, S., Stratmann, F., and Wiedensohler, A.:

- 966 Hygroscopic properties of aerosol particles at high relative humidity and their diurnal
- 967 variations in the north China plain, Atmos. Chem. Phys., 11, 3479-3494,
- 968 https://doi.org/10.5194/acp-11-3479-2011, 2011.
- 969 Lu, Y., Yan, C., Fu, Y., Chen, Y., Liu, Y., Yang, G., Wang, Y., Bianchi, F., Chu, B.,
- 270 Zhou, Y., Yin, R., Baalbaki, R., Garmash, O., Deng, C., Wang, W., Liu, Y., Petäjä, T.,
- 971 Kerminen, V. M., Jiang, J., Kulmala, M., and Wang, L.: A proxy for atmospheric
- 972 daytime gaseous sulfuric acid concentration in urban Beijing, Atmos. Chem. Phys., 19,
- 973 1971–1983, https://doi.org/10.5194/acp-19-1971-2019, 2019.
- Luoma, K., Virkkula, A., Aalto, P., Petäjä, T., and Kulmala, M.: Over a 10-year record
- of aerosol optical properties at SMEAR II, Atmos. Chem. Phys., 19, 11363–11382,
- 976 https://doi.org/10.5194/acp-19-11363-2019, 2019.
- 977 Ma, C. Sen, Ma, G., and Pincebourde, S.: Survive a Warming Climate: Insect Responses
- 978 to Extreme High Temperatures, Annu. Rev. Entomol., 66, 163-184,
- 979 https://doi.org/10.1146/annurev-ento-041520-074454, 2021.
- 980 Ma, N., Zhao, C., Tao, J., Wu, Z., Kecorius, S., Wang, Z., Groß, J., Liu, H., Bian, Y.,
- 81 Kuang, Y., Teich, M., Spindler, G., Muller, K., Van Pinxteren, D., Herrmann, H., Hu,
- 982 M., and Wiedensohler, A.: Variation of CCN activity during new particle formation
- 983 events in the North China Plain, Atmos. Chem. Phys., 16, 8593-8607,
- 984 https://doi.org/10.5194/acp-16-8593-2016, 2016.
- Marshall, S. F., Covert, D. S., and Charlson, R. J.: Relationship between asymmetry
- parameter and hemispheric backscatter ratio: implications for climate forcing by
- 987 aerosols, Appl. Opt., 34, 5–6, 1995.
- Merikanto, J., Spracklen, D. V, Mann, G. W., Pickering, S. J., and Carslaw, K. S.:
- Atmospheric Chemistry and Physics Impact of nucleation on global CCN, Atmos.
- 990 Chem. Phys, 9, 8601–8616, 2009.

- 991 Mishchenko, M. I.: Electromagnetic scattering by nonspherical particles: A tutorial
- 992 review, J. Quant. Spectrosc. Radiat. Transf., 110, 808-832,
- 993 https://doi.org/10.1016/j.jqsrt.2008.12.005, 2009.
- Nairn, J. R. and Fawcett, R. J. B.: The excess heat factor: A metric for heatwave
- intensity and its use in classifying heatwave severity, Int. J. Environ. Res. Public Health,
- 996 12, 227–253, https://doi.org/10.3390/ijerph120100227, 2014.
- 997 Petters, M. D. and Kreidenweis, S. M.: A single parameter representation of
- hygroscopic growth and cloud condensation nucleus activity, Atmos. Chem. Phys., 7,
- 999 1961–1971, https://doi.org/10.5194/acp-7-1961-2007, 2007.
- 1000 Pierce, T. E. and Waldruff, P. S.: Pc-beis: A personal computer version of the biogenic
- 1001 emissions inventory system, J. Air Waste Manag. Assoc., 41, 937-941,
- 1002 https://doi.org/10.1080/10473289.1991.10466890, 1991.
- 1003 Qi, X. M., Ding, A. J., Nie, W., Petäjä, T., Kerminen, V. M., Herrmann, E., Xie, Y. N.,
- Zheng, L. F., Manninen, H., Aalto, P., Sun, J. N., Xu, Z. N., Chi, X. G., Huang, X., Boy,
- 1005 M., Virkkula, A., Yang, X. Q., Fu, C. B., and Kulmala, M.: Aerosol size distribution
- and new particle formation in the western Yangtze River Delta of China: 2 years of
- measurements at the SORPES station, Atmos. Chem. Phys., 15, 12445–12464,
- 1008 https://doi.org/10.5194/acp-15-12445-2015, 2015.
- 1009 Quinn, P. K., Bates, T. S., Baynard, T., Clarke, A. D., Onasch, T. B., Wang, W., Rood,
- 1010 M. J., Andrews, E., Allan, J., Carrico, C. M., Coffman, D., and Worsnop, D.: Impact of
- particulate organic matter on the relative humidity dependence of light scattering: A
- 1012 simplified parameterization, Geophys. Res. Lett., 32, 1-4,
- 1013 https://doi.org/10.1029/2005GL024322, 2005.
- 1014 Ren, J., Chen, L., Fan, T., Liu, J., Jiang, S., and Zhang, F.: The NPF Effect on CCN
- Number Concentrations: A Review and Re-Evaluation of Observations From 35 Sites

- 1016 Worldwide, Geophys. Res. Lett., 48, 1–12, https://doi.org/10.1029/2021GL095190,
- 1017 2021.
- 1018 Rosati, B., Isokääntä, S., Christiansen, S., Jensen, M. M., Moosakutty, S. P., De Jonge,
- 1019 R. W., Massling, A., Glasius, M., Elm, J., Virtanen, A., and Bilde, M.: Hygroscopicity
- and CCN potential of DMS-derived aerosol particles, Atmos. Chem. Phys., 22, 13449—
- 1021 <u>13466</u>, https://doi.org/10.5194/acp-22-13449-2022, 2022.
- Salma, I., Thén, W., Aalto, P., Kerminen, V. M., Kern, A., Barcza, Z., Petäjä, T., and
- 1023 Kulmala, M.: Influence of vegetation on occurrence and time distributions of regional
- new aerosol particle formation and growth, Atmos. Chem. Phys., 21, 2861–2880,
- 1025 https://doi.org/10.5194/acp-21-2861-2021, 2021.
- Schuster, G. L., Dubovik, O., and Holben, B. N.: Angstrom exponent and bimodal
- 1027 aerosol size distributions, J. Geophys. Res. Atmos., 111, 1–14,
- 1028 https://doi.org/10.1029/2005JD006328, 2006.
- 1029 Shang, D., Hu, M., Tang, L., Fang, X., Liu, Y., Wu, Y., Du, Z., Cai, X., Wu, Z., Lou,
- 1030 S., Hallquist, M., Guo, S., and Zhang, Y.: Significant effects of transport on
- nanoparticles during new particle formation events in the atmosphere of Beijing,
- Particuology, 80, 1–10, https://doi.org/10.1016/j.partic.2022.12.006, 2023.
- Sharma, S. and Mujumdar, P.: Increasing frequency and spatial extent of concurrent
- 1034 meteorological droughts and heatwaves in India, Sci. Rep., 7, 1–9,
- 1035 https://doi.org/10.1038/s41598-017-15896-3, 2017.
- 1036 Shen, X. J., Sun, J. Y., Zhang, Y. M., Wehner, B., Nowak, A., Tuch, T., Zhang, X. C.,
- Wang, T. T., Zhou, H. G., Zhang, X. L., Dong, F., Birmili, W., and Wiedensohler, A.:
- First long-term study of particle number size distributions and new particle formation
- events of regional aerosol in the North China Plain, Atmos. Chem. Phys., 11, 1565–
- 1040 1580, https://doi.org/10.5194/acp-11-1565-2011, 2011.

- 1041 Su, Y. W.: The effects of extreme high temperature day off on electricity conservation,
- 1042 Weather. Clim. Soc., 13, 769–782, https://doi.org/10.1175/WCAS-D-20-0176.1, 2021.
- Sun, J., Hermann, M., Weinhold, K., Merkel, M., Birmili, W., Yang, Y., Flentje, H., Ries,
- L., Couret, C., Elsasser, M., Sohmer, R., Wirtz, K., Meinhardt, F., Schü, M., Bath, O.,
- Hellack, B., Kerminen, V., Kulmala, M., Ma, N., and Wiedensohler, A.: Measurement
- 1046 report : Contribution of atmospheric new particle formation to ultrafine particle
- 1047 concentration, cloud condensation nuclei and radiative forcing: Results from five-year
- 1048 observations in Central Europe, Atmos. Chem. Phys., 1–34,
- 1049 https://doi.org/10.5194/acp-24-10667-2024, 2024.
- Sun, X., Sun, Q., Zhou, X., Li, X., Yang, M., Yu, A., and Geng, F.: Heat wave impact
- on mortality in Pudong New Area, China in 2013, Sci. Total Environ., 493, 789–794,
- 1052 <u>https://doi.org/10.1016/j.scitotenv.2014.06.042, 2014.</u>
- Sun, Y., Song, L., Yin, H., Zhang, X., Stott, P., Zhou, B., and Hu, T.: 20. Human
- influence on the 2015 extreme high temperature events in Western China, Bull. Am.
- 1055 Meteorol. Soc., 97, S102–S106, https://doi.org/10.1175/BAMS-D-16-0158.1, 2016.
- Tan, J., Zheng, Y., Song, G., Kalkstein, L. S., Kalkstein, A. J., and Tang, X.: Heat wave
- impacts on mortality in Shanghai, 1998 and 2003, Int. J. Biometeorol., 51, 193–200,
- 1058 https://doi.org/10.1007/s00484-006-0058-3, 2007.
- 1059 Tang, M., Chan, C. K., Li, Y. J., Su, H., Ma, Q., Wu, Z., Zhang, G., Wang, Z., Ge, M.,
- 1060 Hu, M., He, H., and Wang, X.: A review of experimental techniques for aerosol
- 1061 hygroscopicity studies, Atmos. Chem. Phys., 19, 12631–12686,
- 1062 https://doi.org/10.5194/acp-19-12631-2019, 2019.
- 1063 Tao, L., Zhou, Z., Tao, J., Zhang, L., Wu, C., Li, J., Yue, D., Wu, Z., Zhang, Z., Yuan,
- 1064 Z., Huang, J., and Wang, B.: High contribution of new particle formation to ultrafine
- particles in four seasons in an urban atmosphere in south China, Sci. Total Environ.,
- 1066 889, https://doi.org/10.1016/j.scitotenv.2023.164202, 2023.

- Teng, M., Liao, H., Burke, P. J., Chen, T., and Zhang, C.: Adaptive responses: the effects
- of temperature levels on residential electricity use in China, Clim. Change, 172,
- 1069 https://doi.org/10.1007/s10584-022-03374-3, 2022.
- Tian, J., Wang, Q., Zhang, Y., Yan, M., Liu, H., Zhang, N., Ran, W., and Cao, J.: Impacts
- of primary emissions and secondary aerosol formation on air pollution in an urban area
- 1072 of China during the COVID-19 lockdown, Environ. Int., 150, 106426
- 1073 https://doi.org/10.1016/j.envint.2021.106426, 2021.
- 1074 Titos, G., Burgos, M. A., Zieger, P., Alados-Arboledas, L., Baltensperger, U., Jefferson,
- 1075 A., Sherman, J., Weingartner, E., Henzing, B., Luoma, K., O'Dowd, C., Wiedensohler,
- 1076 A., and Andrews, E.: A global study of hygroscopicity-driven light-scattering
- enhancement in the context of other in situ aerosol optical properties, Atmos. Chem.
- 1078 Phys., 21, 13031–13050, https://doi.org/10.5194/acp-21-13031-2021, 2021.
- 1079 Titos, G., Cazorla, A., Zieger, P., Andrews, E., Lyamani, H., Granados-Muñoz, M. J.,
- 1080 Olmo, F. J., and Alados-Arboledas, L.: Effect of hygroscopic growth on the aerosol
- light-scattering coefficient: A review of measurements, techniques and error sources,
- 1082 Atmos. Environ., 141, 494–507, https://doi.org/10.1016/j.atmosenv.2016.07.021, 2016.
- 1083 Titos, G., Jefferson, A., Sheridan, P. J., Andrews, E., Lyamani, H., Alados-Arboledas,
- 1084 L., and Ogren, J. A.: Aerosol light-scattering enhancement due to water uptake during
- 1085 the TCAP campaign, Atmos. Chem. Phys., 14, 7031–7043, https://doi.org/10.5194/acp-
- 1086 14-7031-2014, 2014.
- 1087 Wang, N., Du, Y., Chen, D., Meng, H., Chen, X., Zhou, L., Shi, G., Zhan, Y., Feng, M.,
- 1088 Li, W., Chen, M., Li, Z., and Yang, F.: Spatial disparities of ozone pollution in the
- Sichuan Basin spurred by extreme, hot weather, Atmos. Chem. Phys., 24, 3029–3042,
- 1090 <u>https://doi.org/10.5194/acp-24-3029-2024, 2024.</u>
- 1091 Titos, G., Lyamani, H., Cazorla, A., Sorribas, M., Foyo-Moreno, I., Wiedensohler, A.,
- 1092 and Alados-Arboledas, L.: Study of the relative humidity dependence of aerosol light-

- 1093 scattering in southern Spain, Tellus, Ser. B Chem. Phys. Meteorol., 66,
- 1094 https://doi.org/10.3402/tellusb.v66.24536, 2014.
- 1095 Wang, Y., Li, Z., Zhang, R., Jin, X., Xu, W., Fan, X., Wu, H., Zhang, F., Sun, Y., Wang,
- 1096 Q., Cribb, M., and Hu, D.: Distinct Ultrafine- and Accumulation-Mode Particle
- 1097 Properties in Clean and Polluted Urban Environments, Geophys. Res. Lett., 46, 10918–
- 1098 10925, https://doi.org/10.1029/2019GL084047, 2019.
- 1099 Wang, Z. B., Hu, M., Sun, J. Y., Wu, Z. J., Yue, D. L., Shen, X. J., Zhang, Y. M., Pei, X.
- 1100 Y., Cheng, Y. F., and Wiedensohler, A.: Characteristics of regional new particle
- formation in urban and regional background environments in the North China Plain,
- 1102 Atmos. Chem. Phys., 13, 12495–12506, https://doi.org/10.5194/acp-13-12495-2013,
- 1103 2013.
- 1104 Wang, Z., Wu, Z., Yue, D., Shang, D., Guo, S., Sun, J., Ding, A., Wang, L., Jiang, J.,
- Guo, H., Gao, J., Cheung, H. C., Morawska, L., Keywood, M., and Hu, M.: New
- particle formation in China: Current knowledge and further directions, Sci. Total
- Environ., 577, 258–266, https://doi.org/10.1016/j.scitotenv.2016.10.177, 2017.
- 1108 Westervelt, D. M., Pierce, J. R., Riipinen, I., Trivitayanurak, W., Hamed, A., Kulmala,
- 1109 M., Laaksonen, A., Decesari, S., and Adams, P. J.: Formation and growth of nucleated
- 1 particles into cloud condensation nuclei: Model-measurement comparison, Atmos.
- 1|111 Chem. Phys., 13, 7645–7663, https://doi.org/10.5194/acp-13-7645-2013, 2013.
- Wu, Z. J., Poulain, L., Birmili, W., Größ, J., Niedermeier, N., Wang, Z. B., Herrmann,
- 1113 H., and Wiedensohler, A.: Some insights into the condensing vapors driving new
- particle growth to CCN sizes on the basis of hygroscopicity measurements, Atmos.
- 1115 Chem. Phys., 15, 13071–13083, https://doi.org/10.5194/acp-15-13071-2015, 2015.
- Wu, Z. J., Zheng, J., Shang, D. J., Du, Z. F., Wu, Y. S., Zeng, L. M., Wiedensohler, A.,
- and Hu, M.: Particle hygroscopicity and its link to chemical composition in the urban

- atmosphere of Beijing, China, during summertime, Atmos. Chem. Phys., 16, 1123-
- 1119 1138, https://doi.org/10.5194/acp-16-1123-2016, 2016.
- 1120 Xia, C., Sun, J., Hu, X., Shen, X., Zhang, Y., Zhang, S., Wang, J., Liu, Q., Lu, J., Liu,
- 1121 S., and Zhang, X.: Effects of hygroscopicity on aerosol optical properties and direct
- radiative forcing in Beijing: Based on two-year observations, Sci. Total Environ., 857,
- 1123 159233, https://doi.org/10.1016/j.scitotenv.2022.159233, 2023.
- 1124 Xu, W. Y., Zhao, C. S., Ran, L., Deng, Z. Z., Liu, P. F., Ma, N., Lin, W. L., Xu, X. B.,
- Yan, P., He, X., Yu, J., Liang, W. D., and Chen, L. L.: Characteristics of pollutants and
- their correlation to meteorological conditions at a suburban site in the North China Plain,
- 1127 Atmos. Chem. Phys., 11, 4353–4369, https://doi.org/10.5194/acp-11-4353-2011, 2011.
- 1 28 Xu, W., Chen, C., Qiu, Y., Xie, C., Chen, Y., Ma, N., Xu, W., Fu, P., Wang, Z., Pan,
- 1 29 X., Zhu, J., Ngcg, N. L., and Sun, Y.: Size-resolved characterization of organic aerosol
- in the North China Plain: New insights from high resolution spectral analysis, Environ.
- 1|131 <u>Sci. Atmos., 1, 346–358, https://doi.org/10.1039/d1ea00025j, 2021.</u>
- 1|132 Xu, W., Kuang, Y., Xu, W., Zhang, Z., Luo, B., Zhang, X., Tao, J., Qiao, H., Liu, L.,
- 1 and Sun, Y.: Hygroscopic growth and activation changed submicron aerosol
- 1 | 134 composition and properties in the North China Plain, Atmos. Chem. Phys., 24, 9387–
- 1|135 9399, https://doi.org/10.5194/acp-24-9387-2024, 2024.
- 1136 Xue, B., Kuang, Y., Xu, W., and Zhao, P.: Joint increase of aerosol scattering efficiency
- and aerosol hygroscopicity aggravate visibility impairment in the North China Plain,
- 1138 Sci. Total Environ., 839, 141163, https://doi.org/10.1016/j.scitotenv.2022.156279,
- 1139 2022.
- Yang, P., Feng, Q., Hong, G., Kattawar, G. W., Wiscombe, W. J., Mishchenko, M. I.,
- Dubovik, O., Laszlo, I., and Sokolik, I. N.: Modeling of the scattering and radiative
- properties of nonspherical dust-like aerosols, J. Aerosol Sci., 38, 995-1014,
- 1143 https://doi.org/10.1016/j.jaerosci.2007.07.001, 2007.

- 1144 Yarragunta, Y., Srivastava, S., Mitra, D., and Chandola, H. C.: Source apportionment
- of carbon monoxide over India: a quantitative analysis using MOZART-4, Environ. Sci.
- Pollut. Res., 28, 8722–8742, https://doi.org/10.1007/s11356-020-11099-y, 2021.
- 1147 Zhang, L., Sun, J. Y., Shen, X. J., Zhang, Y. M., Che, H., Ma, Q. L., Zhang, Y. W., Zhang,
- 1148 X. Y., and Ogren, J. A.: Observations of relative humidity effects on aerosol light
- scattering in the Yangtze River Delta of China, Atmos. Chem. Phys., 15, 8439–8454,
- 1150 https://doi.org/10.5194/acp-15-8439-2015, 2015.
- 21151 Zhang, R., Khalizov, A. F., Pagels, J., Zhang, D., Xue, H., and McMurry, P. H.:
- 1152 Variability in morphology, hygroscopicity, and optical properties of soot aerosols
- during atmospheric processing, Proc. Natl. Acad. Sci. U. S. A., 105, 10291–10296,
- 1154 https://doi.org/10.1073/pnas.0804860105, 2008.
- 21155 Zhang, R., Khalizov, A., Wang, L., Hu, M., and Xu, W.: Nucleation and growth of
- 1156 nanoparticles in the atmosphere, Chem. Rev., 112, 1957–2011,
- 1157 https://doi.org/10.1021/cr2001756, 2012.
- Zhang, R., Suh, I., Zhao, J., Zhang, D., Fortner, E. C., Tie, X., Molina, L. T., and Molina,
- 1159 M. J.: Atmospheric new particle formation enhanced by organic acids, Science (80-.).,
- 304, 1487–1490, https://doi.org/10.1126/science.1095139, 2004.
- Zhang, R., Wang, G., Guo, S., Zamora, M. L., Ying, Q., Lin, Y., Wang, W., Hu, M., and
- Wang, Y.: Formation of Urban Fine Particulate Matter, Chem. Rev., 115, 3803–3855,
- 1163 https://doi.org/10.1021/acs.chemrev.5b00067, 2015.
- 1164 Zhang, Z., Xu, W., Zeng, S., Liu, Y., Liu, T., Zhang, Y., Du, A., Li, Y., Zhang, N., Wang,
- J., Aruffo, E., Han, P., Li, J., Wang, Z., and Sun, Y.: Secondary Organic Aerosol
- Formation from Ambient Air in Summer in Urban Beijing: Contribution of S/IVOCs
- 1167 and Impacts of Heat Waves, Environ. Sci. Technol. Lett.,
- 1168 https://doi.org/10.1021/acs.estlett.4c00415, 2024.

- Zhao, C., Yu, Y., Kuang, Y., Tao, J., and Zhao, G.: Recent Progress of Aerosol Light-
- scattering Enhancement Factor Studies in China, Adv. Atmos. Sci., 36, 1015–1026,
- 1171 https://doi.org/10.1007/s00376-019-8248-1, 2019.
- Zhao, S., Yu, Y., Li, J., Yin, D., Qi, S., and Qin, D.: Response of particle number
- concentrations to the clean air action plan: Lessons from the first long-term aerosol
- measurements in a typical urban valley in western China, Atmos. Chem. Phys., 21,
- 1175 14959–14981, https://doi.org/10.5194/acp-21-14959-2021, 2021.
- 1176 Zhu, Y., Shen, Y., Li, K., Meng, H., Sun, Y., Yao, X., Gao, H., Xue, L., and Wang, W.:
- 1177 Investigation of Particle Number Concentrations and New Particle Formation With
- 1178 Largely Reduced Air Pollutant Emissions at a Coastal Semi-Urban Site in Northern
- 1179 China, J. Geophys. Res. Atmos., 126, 1–20, https://doi.org/10.1029/2021JD035419,
- 1180 2021.
- Zieger, P., Weingartner, E., Henzing, J., Moerman, M., De Leeuw, G., Mikkilä, J., Ehn,
- 1182 M., Petäjä, T., Clémer, K., Van Roozendael, M., Yilmaz, S., Frieß, U., Irie, H., Wagner,
- 1183 T., Shaiganfar, R., Beirle, S., Apituley, A., Wilson, K., and Baltensperger, U.:
- 1184 Comparison of ambient aerosol extinction coefficients obtained from in-situ, MAX-
- DOAS and LIDAR measurements at Cabauw, Atmos. Chem. Phys., 11, 2603-2624,
- 1186 https://doi.org/10.5194/acp-11-2603-2011, 2011.

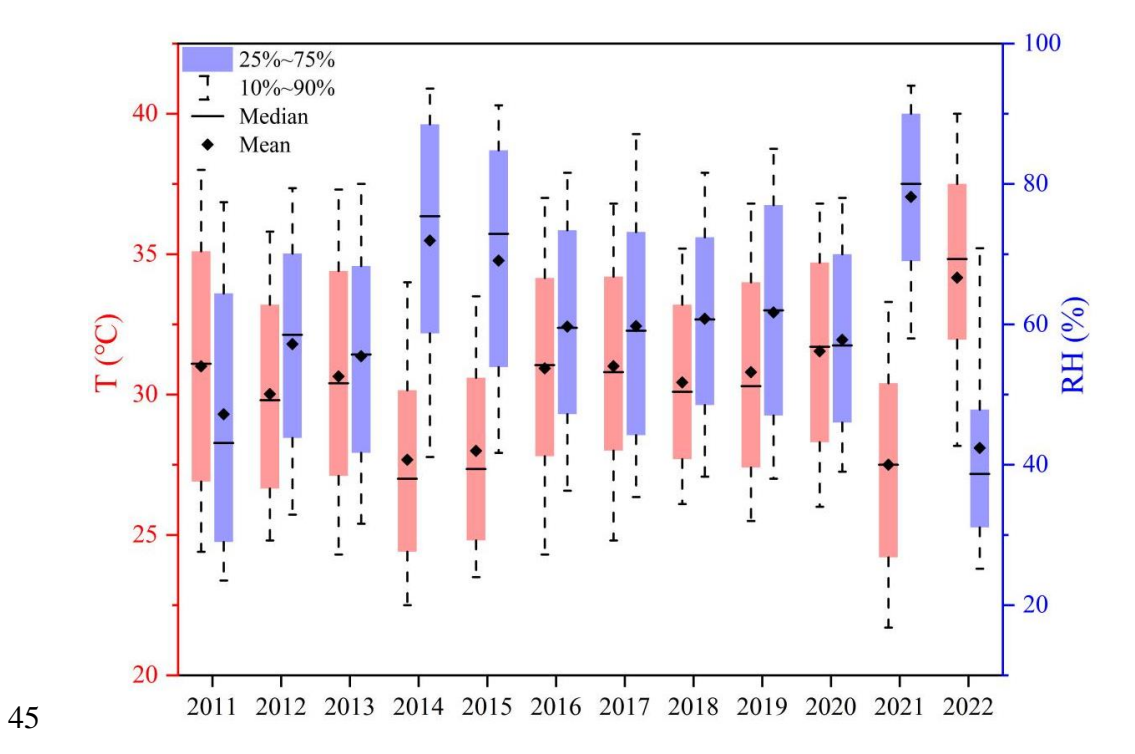
Supporting Information for

2	Divergent changes in aerosol optical hygroscopicity and new
3	particle formation induced by heatwaves
4 5 6 7	Yuhang Hao ^{1, a} , Peizhao Li ^{1, a} , Yafeng Gou ¹ , Zhenshuai Wang ¹ , Mi Tian ¹ , Yang Chen ² , Ye Kuang ³ , Hanbing Xu ⁴ , Fenglian Wan ¹ , Yuqian Luo ¹ , Wei Huang ⁵ , Jing Chen ^{1, 6, *}
8	¹ College of Environment and Ecology, Chongqing University, Chongqing 400045, China
9	² Center for the Atmospheric Environment Research, Chongqing Institute of Green and
10	Intelligent Technology, Chinese Academy of Sciences, Chongqing 400714, China
11	³ Institute for Environmental and Climate Research, Jinan University, Guangzhou
12	511443, China
13	⁴ Experimental Teaching Center, Sun Yat-sen University, Guangzhou 510275, China
14	⁵ National Meteorological Center, China Meteorological Administration, Beijing 100081,
15	China
16	⁶ Key Laboratory of Three Gorges Reservoir Region's Eco-Environment, Ministry of
17	Education, Chongqing University, Chongqing 400045, China
18 19 20	^a These authors contributed equally
21	Correspondence to: Jing Chen (chen.jing@cqu.edu.cn)
22	
23	
24	
25	Contents of this file
26	
27	Figures S1 to S143
28	Tables S1 to S2
29	References

S1. Site description

The observation site was located on the rooftop of a building (~15 m above the ground) in the main campus of Chongqing University (29.57°N, 106.46°E) in the urban center of Chongqing, southwest China. The site is characterized by a typical residential and commercial environment, mainly influenced by local emissions (e.g., traffic, cooking). All instruments were installed in an air-conditioned room, with the room temperature maintained about 25°C. The ambient air was sampled at a flowrate of 16.7 LPM through a PM_{2.5} impactor (model 2000-30EH, URG Inc.) and dried with a Nafion dryer (model MD-700, Perma Pure LLC), to achieve a low relative humidity level (RH <305%) prior to the online aerosol size distribution, optical and hygroscopic measurements. During the observation period, urban Chongqing suffered a rare heatwave. The mean temperature and relative humidity during the study period and the same period from 2011 to 2021 in urban Chongqing are given in Figure S1. Based on the method proposed by Nairn and Fawcett

- 43 (2014), the Excess Heat Factor (EHF) metric was accordingly calculated for this study
- 44 <u>(Figure S2a).</u>



46 **Figure S1.** The variation trends of annual temperature and RH during the study period in 2022 and the same period from 2011 to 2021 in urban Chongqing.

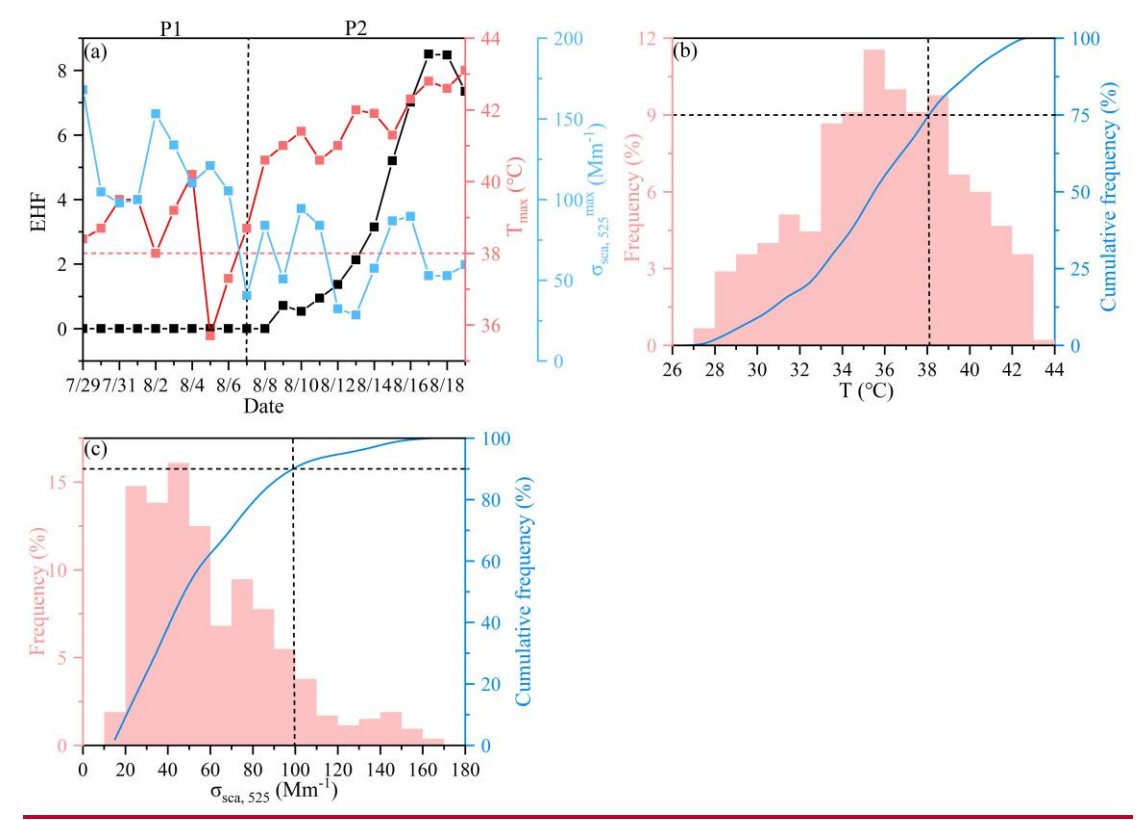


Figure S2. (a) Time series of calculated EHF, along with the daily maximum temperature (T_{max}) and dry $\sigma_{sca, 525}$ results, during the study period. The corresponding occurrence frequency and cumulative frequency of hourly (b) temperature and (c) $\sigma_{sca, 525}$ data records.

S2. Derivation of aerosol liquid water content (ALWC)

In this study, ALWC was determined as the discrepancy in aerosol volume concentration between the humidified and dry particles:

$$ALWC = V_{dry} \times (f v(RH) - 1)$$
(1)

where the dry aerosol volume concentration (V_{dry}) was estimated with the dry scattering coefficients at three wavelengths utilizing a machine learning method (Kuang et al., 2018). Given the dependence on aerosol hygroscopicity and size distribution, the aerosol volume growth factor ($f_V(RH)$) can be obtained from the observed f(RH) and SAE (a proxy of aerosol size distribution) with the humidified nephelometer system (Kuang et al., 2018). Accordingly, the fraction of aerosol water content (f_W) upon hydration could be expressed as:

$$f w = \frac{ALWC}{ALWC + V_{dry}}$$

Both dry and humidified nephelometers were calibrated before the measurement for the zero/span check with the particle-free air/standard gas (R134a), following standard calibration procedures. More detailed descriptions about the home-built humidified nephelometer system can refer to Kuang et al. (2017, 2020) and Xue et al. (2022).

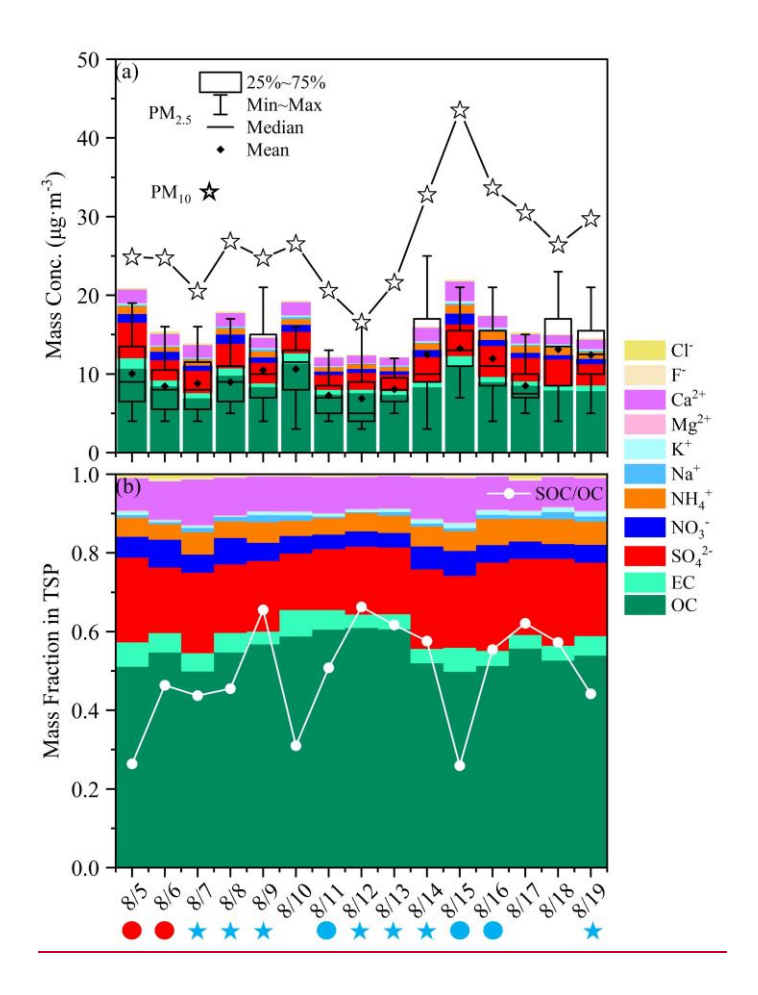
S3. Offline particle sampling and chemical analysis

69

71

88

70 Total suspended particle (TSP) filter samples were collected by a moderate volume air sampler at a flow rate of 200 L/min from August 5 to 19, 2022. Daily (from 9:30 a.m. 72 to 9:00 a.m. of the next day) integrated ambient TSP samples were collected on prebaked 73 (600°C, 5h) quartz-fiber filters (90 mm, Whatman) for water-soluble ions, organic carbon 74 (OC), and elemental carbon (EC) analysis. Water-soluble inorganic anions (i.e., SO_4^{2-} , NO_3^{-} , Cl^{-} and F^{-}) and cations (i.e., NH_4^{+} , 75 Na^+ , Mg^{2+} , Ca^{2+} and K^+) were quantified using an ion chromatograph analyzer (Dionex 600, 76 77 Dionex, USA) following standard procedures (Peng et al., 2019; Wang et al., 2018). 78 Elemental carbon (EC) and organic carbon (OC) in the collected TSP samples were 79 analyzed using a DRI Model 2015 Multi-wavelength Carbon Analyzer (Magee Scientific, 80 USA). The methodology for OC/EC analysis was based on the thermal-optical reflectance 81 (TOR) method following the Interagency Monitoring of Protected Visual Environments 82 (IMPROVE-A) protocol, as shown in Chow et al. (2007, 2011) and Peng et al. (2020). The 83 secondary organic carbon (SOC) can be estimated with the obtained OC and EC data 84 according to the EC-tracer method (Castro et al., 1999; Strader et al., 1999), details of 85 which was also available in our previous study (Hao et al., 2024). 86 The chemical components mass concentration and mass fraction in TSP, as well as 87 the PM_{2.5} (PM₁₀) mass concentration and the ratio of SOC/TOC during the study period are depicted in Figure S23.



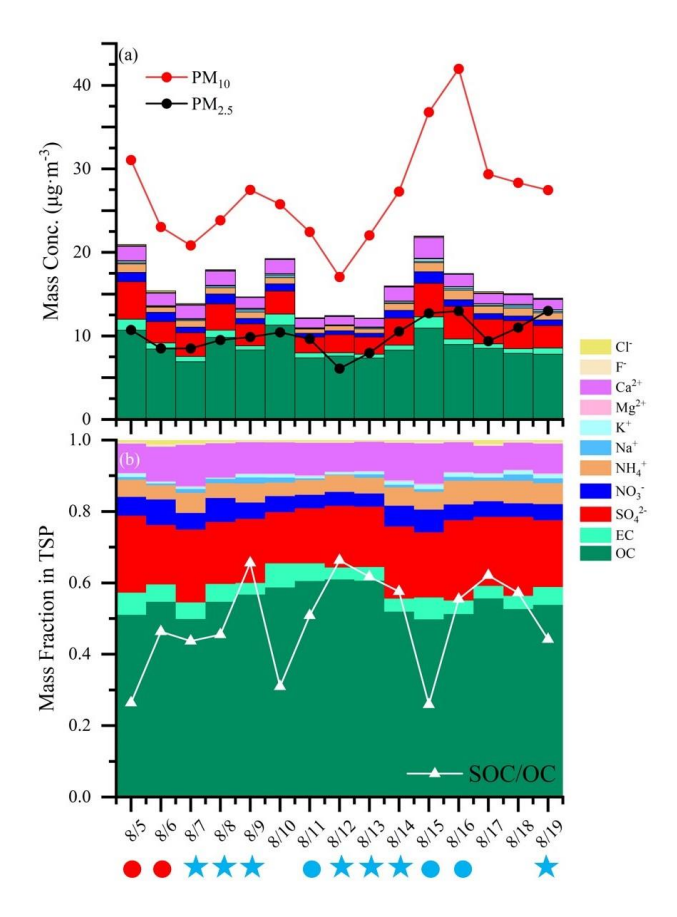


Figure S23. The mass concentration (a) and mass fraction (b) of chemical components in TSP (total suspended particulates) during the study period. The $\frac{\text{red}}{\text{red}}$ black $\frac{\text{stars}}{\text{stars}}$ box plots and white line stands for $\frac{\text{daily mean PM}_{10}}{\text{dates represent the P1 or P2 non-event days,}}$ and the blue stars represent the P2 NPF_{C, HW} days.

S4. Meteorological and air quality data

All the contemporary hourly meteorological datasets including relative humidity (RH), temperature (T), visibility (VIS), wind speed (WS), wind direction (WD), precipitation, and the mixing layer height (MLH) were obtained from the Integrated Surface Database from the U.S. National Centers for Environmental Information (https://ncdc.noaa.gov/isd) (Wan et al., 2023; Xu et al., 2020), and the mixing layer height (MLH) data were achieved from China Meteorological Administration in this study. Ultraviolet (UV) radiation data were downloaded from European Centre for Medium-Range Weather Forecasts (https://cds.climate.copernicus.eu/).

Hourly air pollutant datasets including $PM_{2.5}$, PM_{10} , NO_2 , SO_2 , CO and O_3 were achieved from the China National Environmental Monitoring Center (http://www.cnemc.cn/en). The gas-phase sulfuric acid, known as the most ubiquitous and key precursor for NPF, was estimated with the UVB (UVB = 5% UV, Fitsiou et al., 2021) and SO_2 concentration (Lu et al., 2019):

H₂SO₄ =
$$280.05 \times \text{UVB}^{0.14} \times \text{SO}_2^{0.40}$$
 (3)

S5. Particle number size distribution measurements

During the field observation, every 3-min PNSD and particle volume size distribution (PVSD) within the diameter range of 14.1–710.5 nm was measured by a SMPS, which consisted of a soft X-Ray neutralizer (model 30808, TSI Inc.), a differential mobility analyzer (model 3081, TSI Inc.), and a condensation particle counter (model 3775, TSI Inc.) (Dominick et al., 2018; Rissler et al., 2006). The SMPS was operated at a sheath/sample flow rate of 3.0/0.3 LPM, and the detected size range was 14.1-710.5 nm with 110 size bins. Data inversion of measured particle size distributions was achieved with the Aerosol Instrument Manager software (AIM, TSI Inc.), including the multiple charge and diffusion corrections (Denjean et al., 2015; Rosati et al., 2022).

The aerosol effective radius (R_{eff}) is a crucial parameter regulating optical properties (e.g., light scattering) of the aerosol population (Hansen and Travis, 1974; Grainger et al., 1995). It can be calculated with the measured size distribution as below (Hansen and Travis, 1974; Grainger et al., 1995):

$$R_{eff} = \frac{\int D_P^3 n(log D_P) dlog D_P}{\int D_P^2 n(log D_P) dlog D_P}$$

126 (4)

where $n(log D_P)$ is the particle number size distribution in log scale.

Using the measured PNSD data, NPF events were identified according to the criteria raised by Dal Maso et al. (2005), and the key parameters related to NPF events (e.g., formation rate (FR) and growth rate (GR) of new particles, condensation sink (CS) and coagulation sink (CoagS)) could be derived following the methodologies introduced by Dal Maso et al. (2005) and Kulmala et al. (2012). The specific dates for NPF and non-event elassifications were summarized in Table S1.

The specific dates for NPF and non-event classifications were summarized in Table S1, and the frequencies of NPF, non-event and Undefined days during both periods were shown in Figure S4a. By using the HYSPLIT (Hybrid Single-Particle Lagrangian Integrated Trajectory) 4 model developed by NOAA (Stein et al., 2015), the 48-h back trajectories of air masses at 500 m altitude above the observation site during this study period were calculated and visualized by MeteoInfoMap (version 3.9.9; Figure S4b) (Chen et al., 2021; Tian et al., 2021; Wang, 2014).

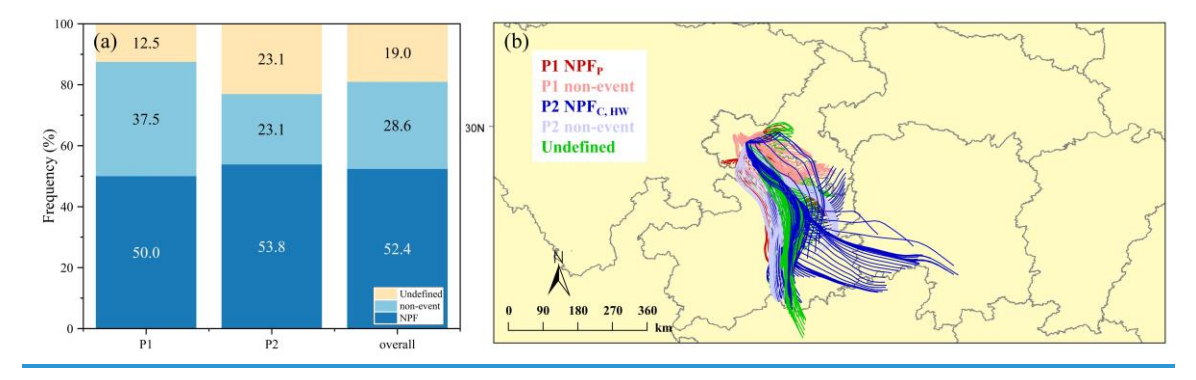
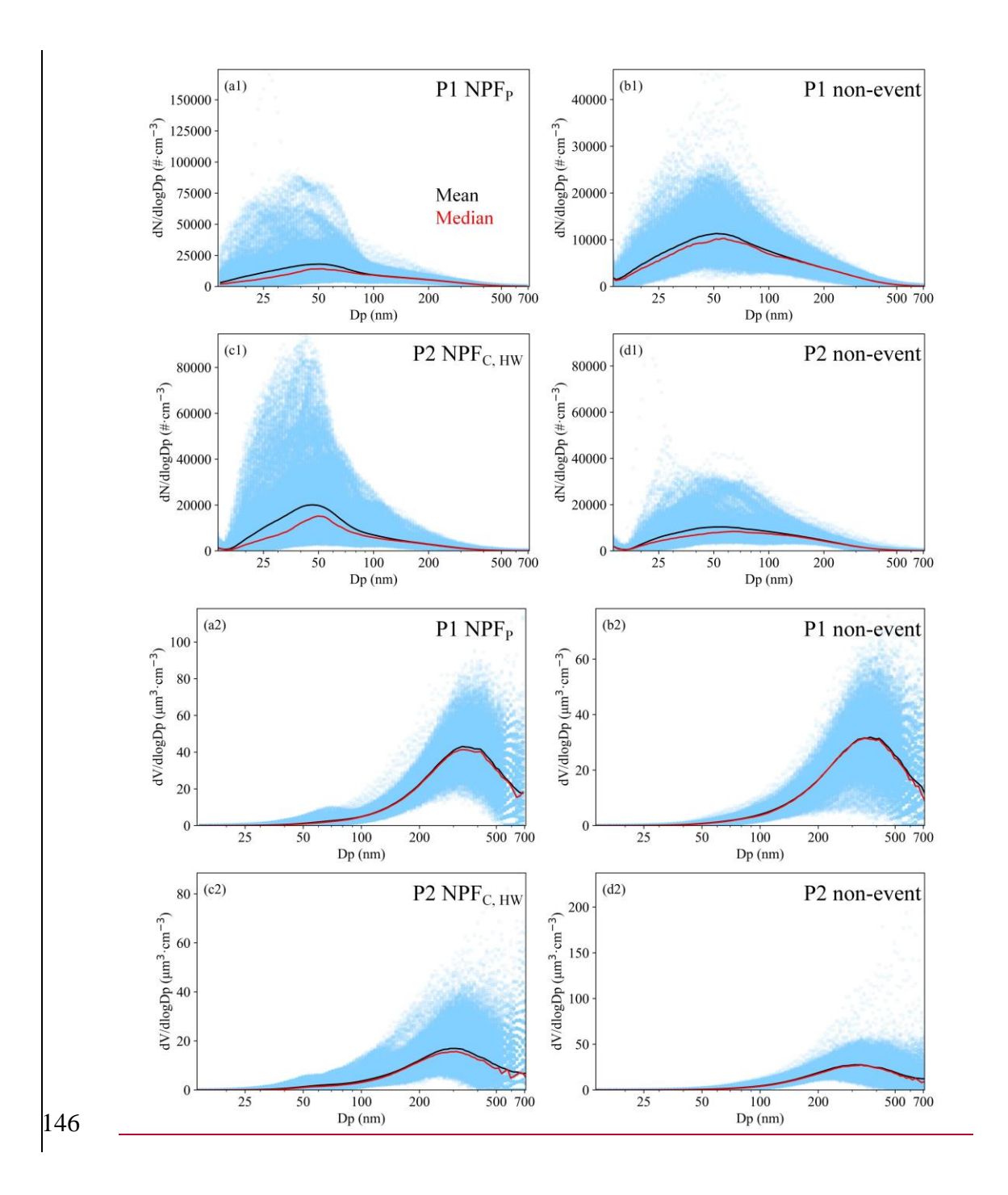


Figure S4. (a) The occurrence frequencies of NPF, non-event and Undefined days during P1, P2 and the whole observation periods. (b) The 48-h air-mass back trajectories during the study period.



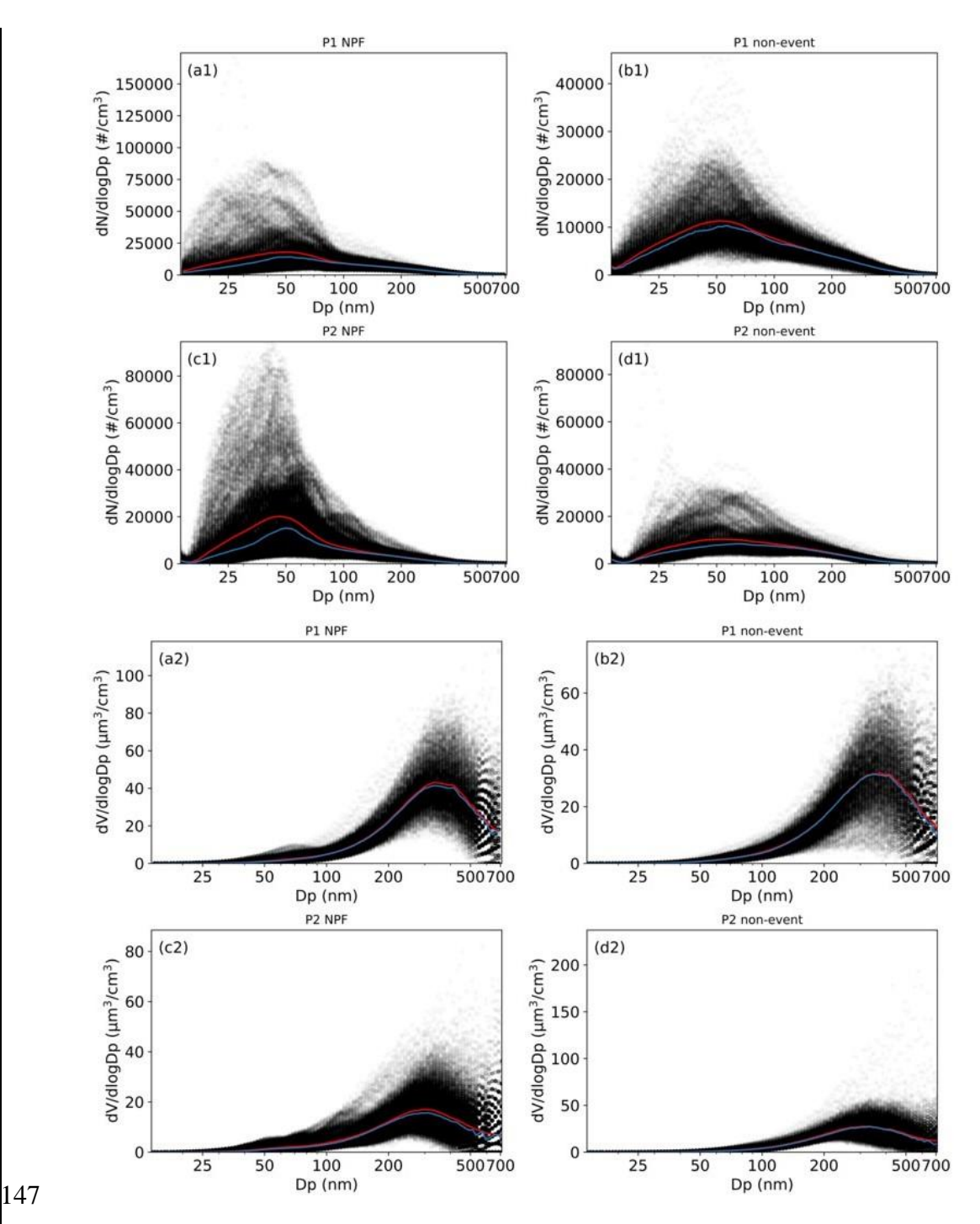


Figure S35. The PNSDs (a1-d1) and PVSDs (a2-d2) for different event categories. The red and blue lines represent the mean and median values, respectively.

The diurnal variations of PNSD, R_{eff}, particle mode diameter (D_{mode}), as well as CS, were given in Figure S6.

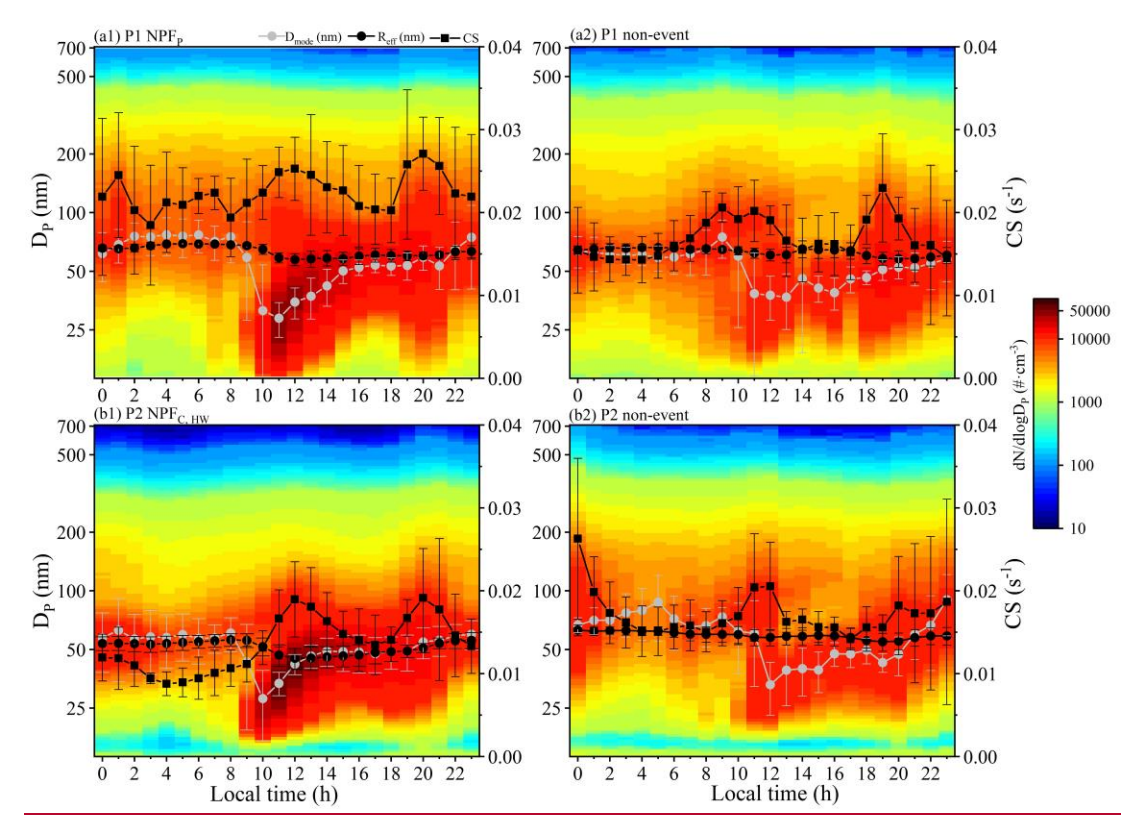


Figure S6. Diurnal variations of PNSDs, D_{mode} , R_{eff} , and CS during P1 and P2 NPF days (a1, b1) and non-event days (a2, b2), the error bars stand for \pm one standard deviations.

152

153

The PNSD is typically categorized into three modes: the nucleation mode (D_p <25 nm), Aitken mode (25-100 nm), and accumulation mode (D_p >100 nm) (Zhu et al., 2021). The diurnal variations of aerosol number and volume concentrations, as well as R_{eff} , for different modes on NPF event days are illustrated in Figure S47.

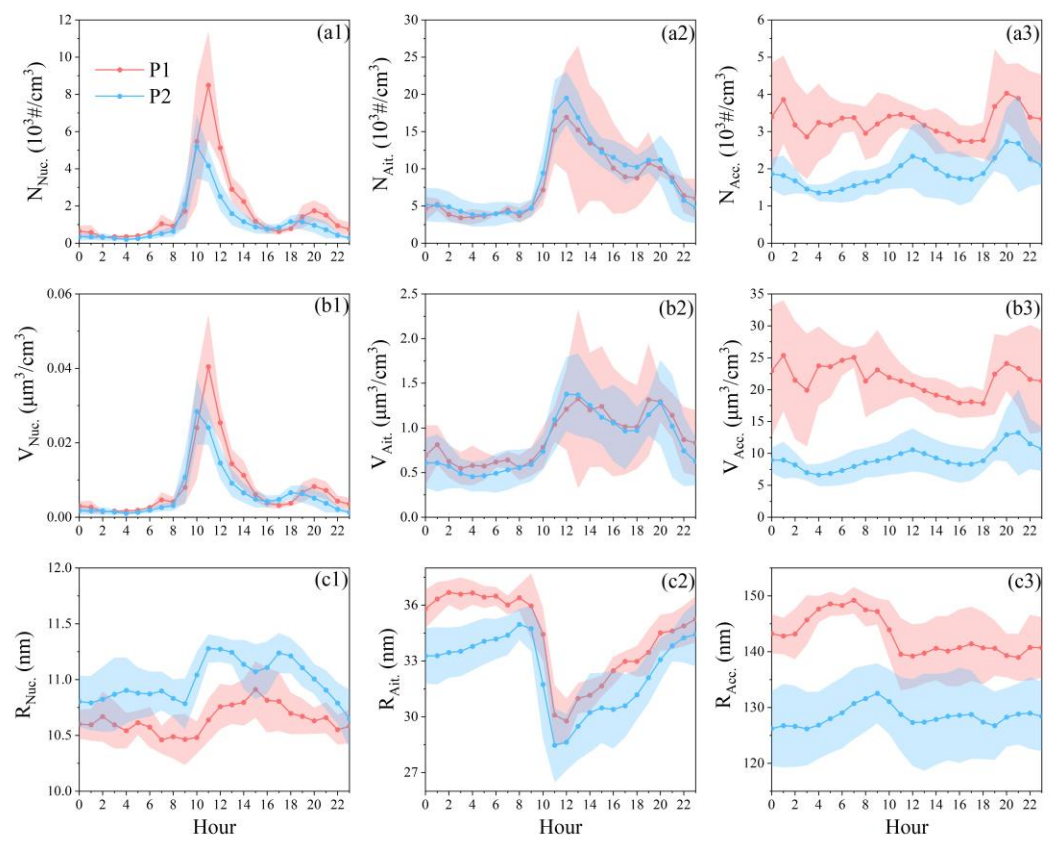


Figure S47. Diurnal variations of the number (a1-a3), volume (b1-b3) concentration and effective radius (c1-c3) of nucleation mode (left column), Aitken mode (middle column), and accumulation mode (right column) particles on NPF event days during P1 (red line) and P2 (blue line) periods. The shaded areas stand for the corresponding \pm 1 σ standard deviations.

S5. The observed temperature, start and end time of NPF, and the subsequent growth end time during NPF events. The specific start and end time of NPF, along with the subsequent growth end time during NPF events were displayed in Figure S8. The NPF event end time is defined as the moment when the formation of new nucleation-mode particles (diameter <25 nm) ceases, specifically identified by the absence of a notable increase in sub-25 nm particles (Dal Maso et al., 2005; Hamed et al., 2007; Kerminen et al., 2018). The growth event end time refers to the time when the newly formed particles stop growing, typically due to the depletion of low-volatility vapors or particle coagulation (Dal Maso et al., 2005; Kerminen et al., 2018). This can be observed as the stabilization of particle diameters in the Aitken/accumulation mode, marked by a flattening of the growth trajectory in the PNSD plot (Figure 1i).

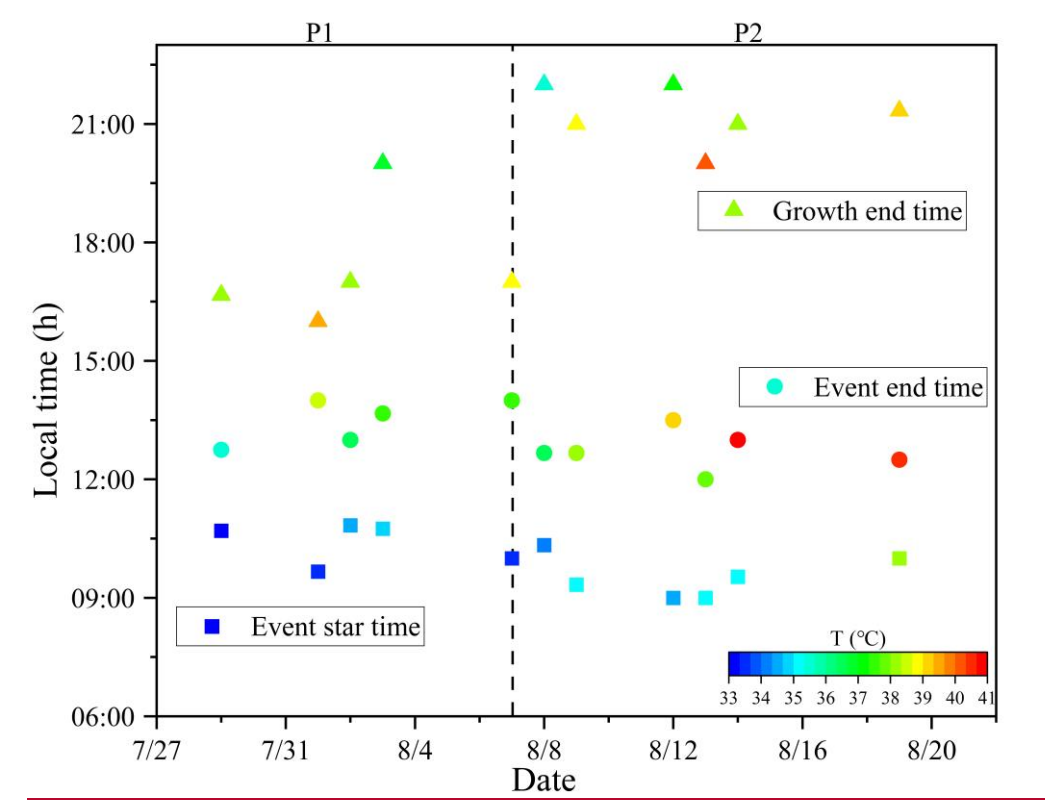


Figure S58. The start and end time of NPF, along with the subsequent growth end time and their corresponding temperature levels during NPF events.

S6. Diurnal variations of humidified nephelometer system related parameters on non-event days during both P1 and P2 periods

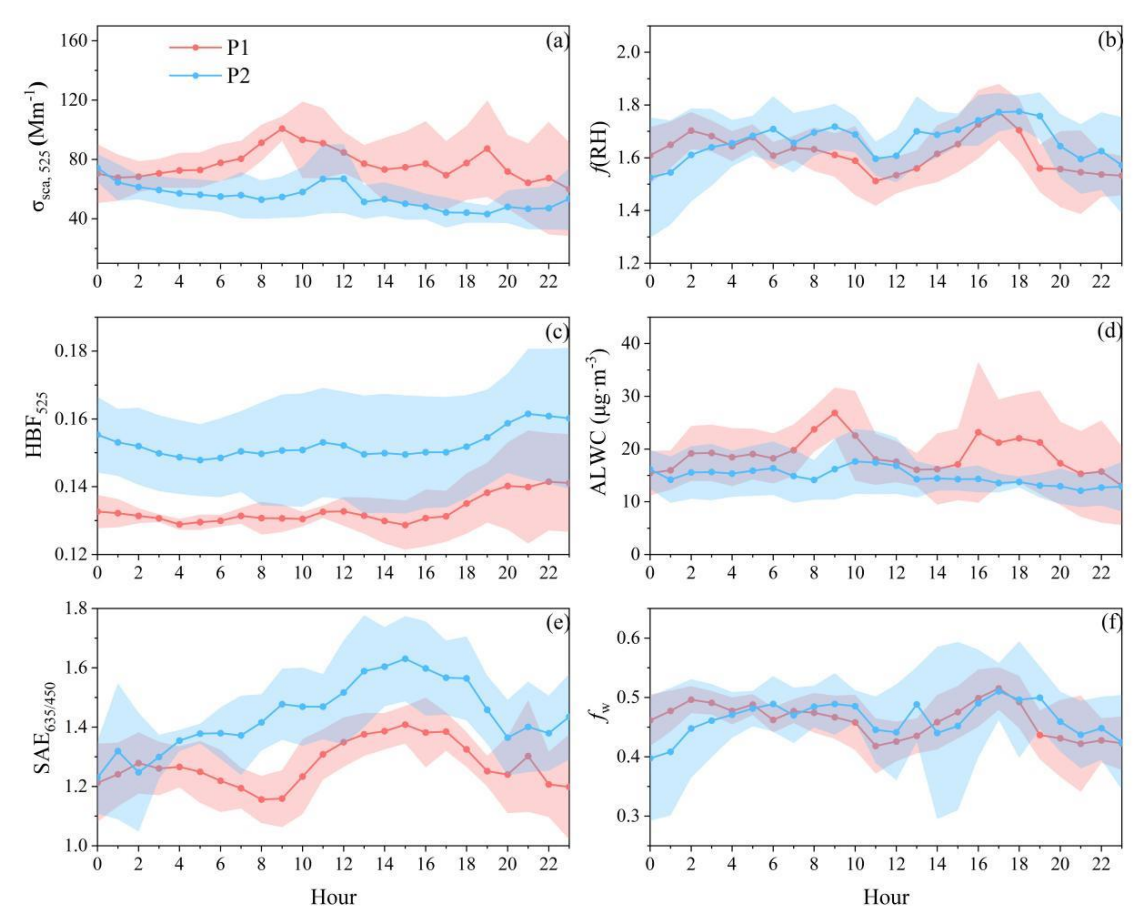
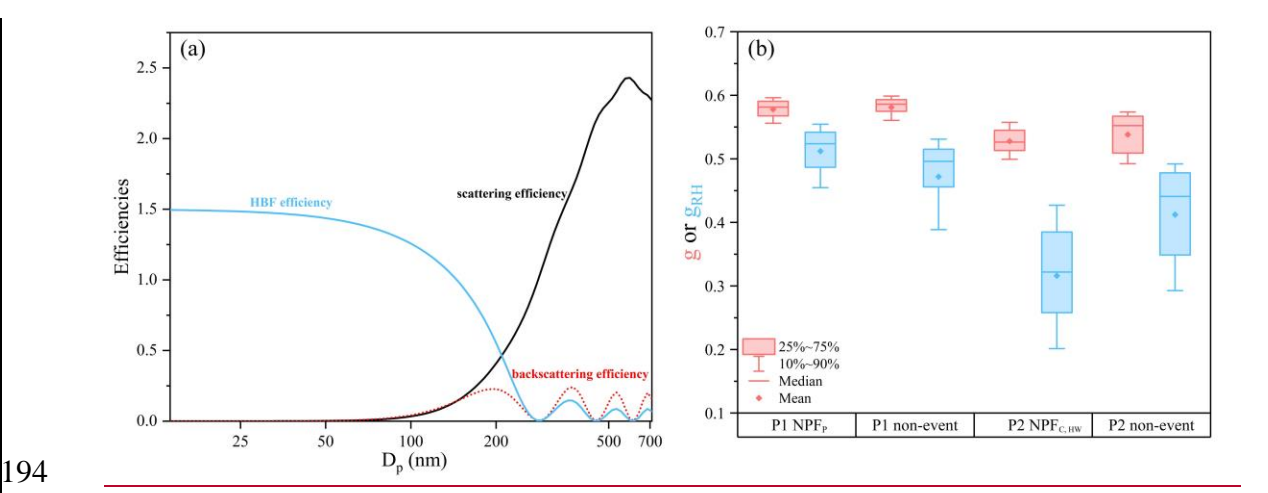


Figure S62. Diurnal variations of $\sigma_{\text{sca, 525}}$ (a), f(RH) (b), HBF₅₂₅ (c), ALWC (d), SAE_{635/450} (e) and f_{W} (f) on non-event days during P1 (red line) and P2 (blue line) periods. The shaded areas stand for the corresponding $\pm 1\sigma$ standard deviations.

S7. Calculation of $\sigma_{sca, 525}$ with the Mie theory and measured PNSD

Based on the Mie theory and measured PNSD, the σ_{sca} and σ_{bsca} for $\lambda = 525$ nm and a fixed refractive index of 1.53 + 0.1i were calculated, with good agreements between the theoretically calculated and measured values ($R^2 = 0.99$ for $\sigma_{sca, 525}$; $R^2 = 0.98$ for $\sigma_{bsca, 525}$). The size-dependent σ_{sca} , σ_{bsca} and HBF efficiencies simulated from Mie theory are shown in Figure S710a. A good correlation between SMPS-determined particle volume concentration and the measured $\sigma_{sca, 525}$ is also observed in Figure S811. The size-resolved $\sigma_{sca, 525}$ distributions and size-resolved $\sigma_{sca, 525}$ cumulative frequency distribution on NPF event (non-event) days during P1 and P2 periods are displayed in Figure S912.





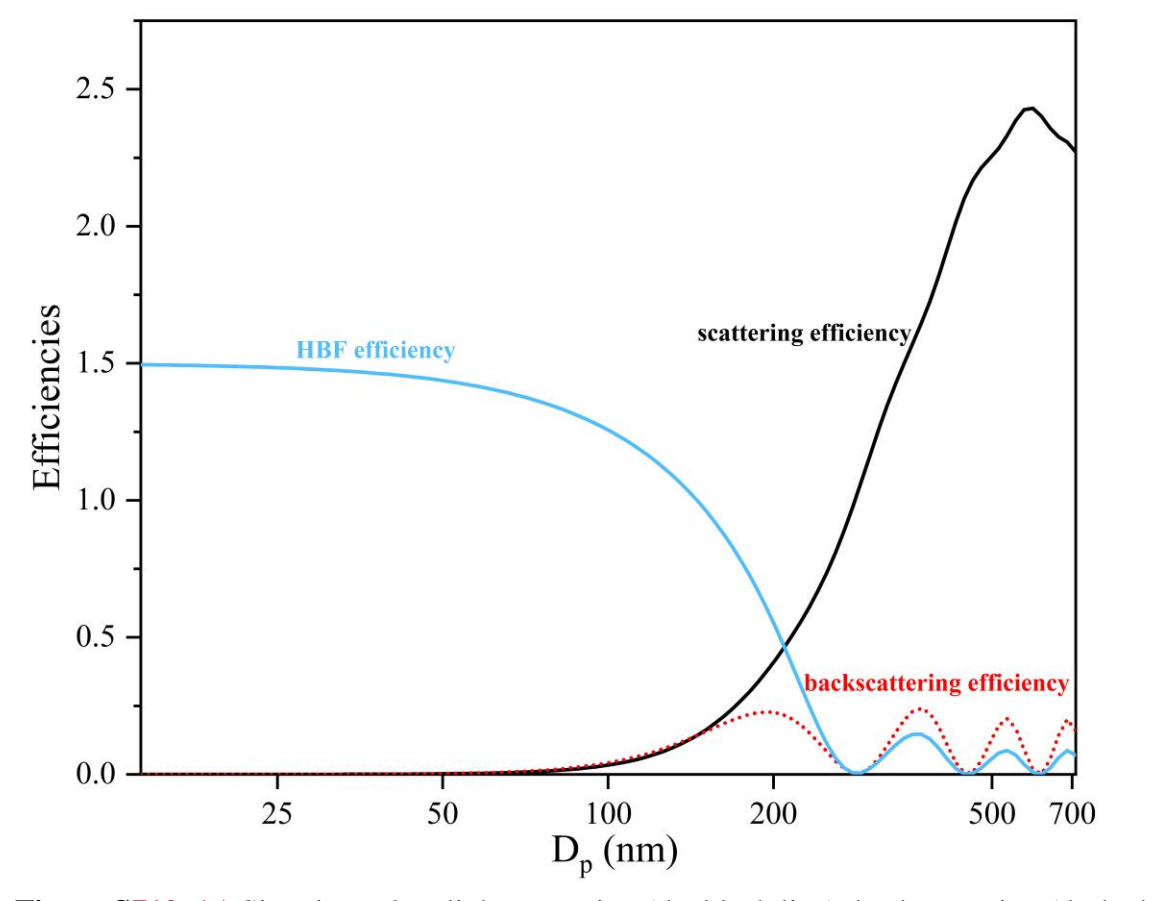


Figure S710. (a) Size-dependent light scattering (the black line), backscattering (dashed red line) and HBF (the blue line) efficiencies simulated from Mie theory for the case of λ = 525 nm and refractive index of 1.53 + 0.1i. (b) The box plots of the HBF₅₂₅ (HBF₅₂₅, RH) derived g (gRH).

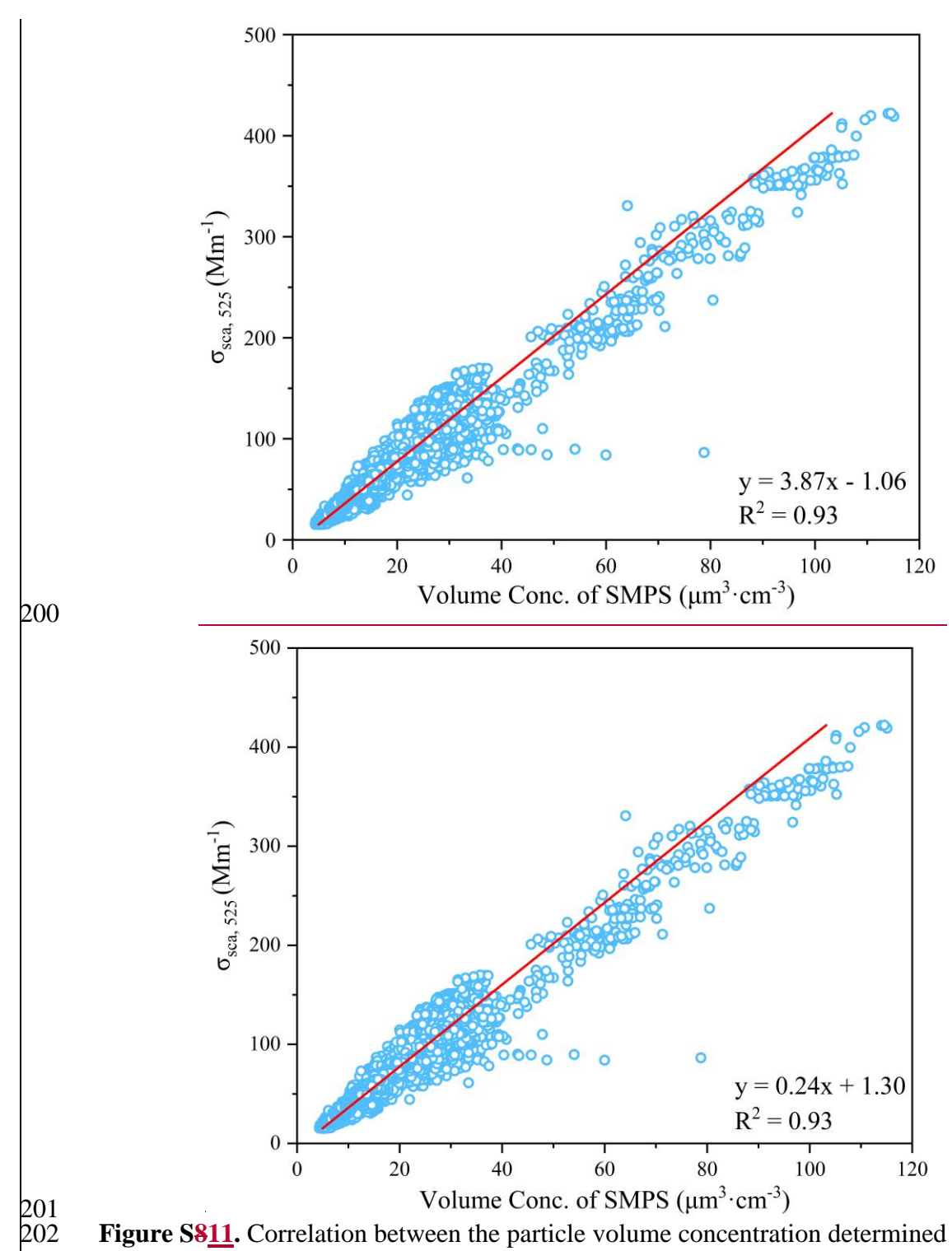
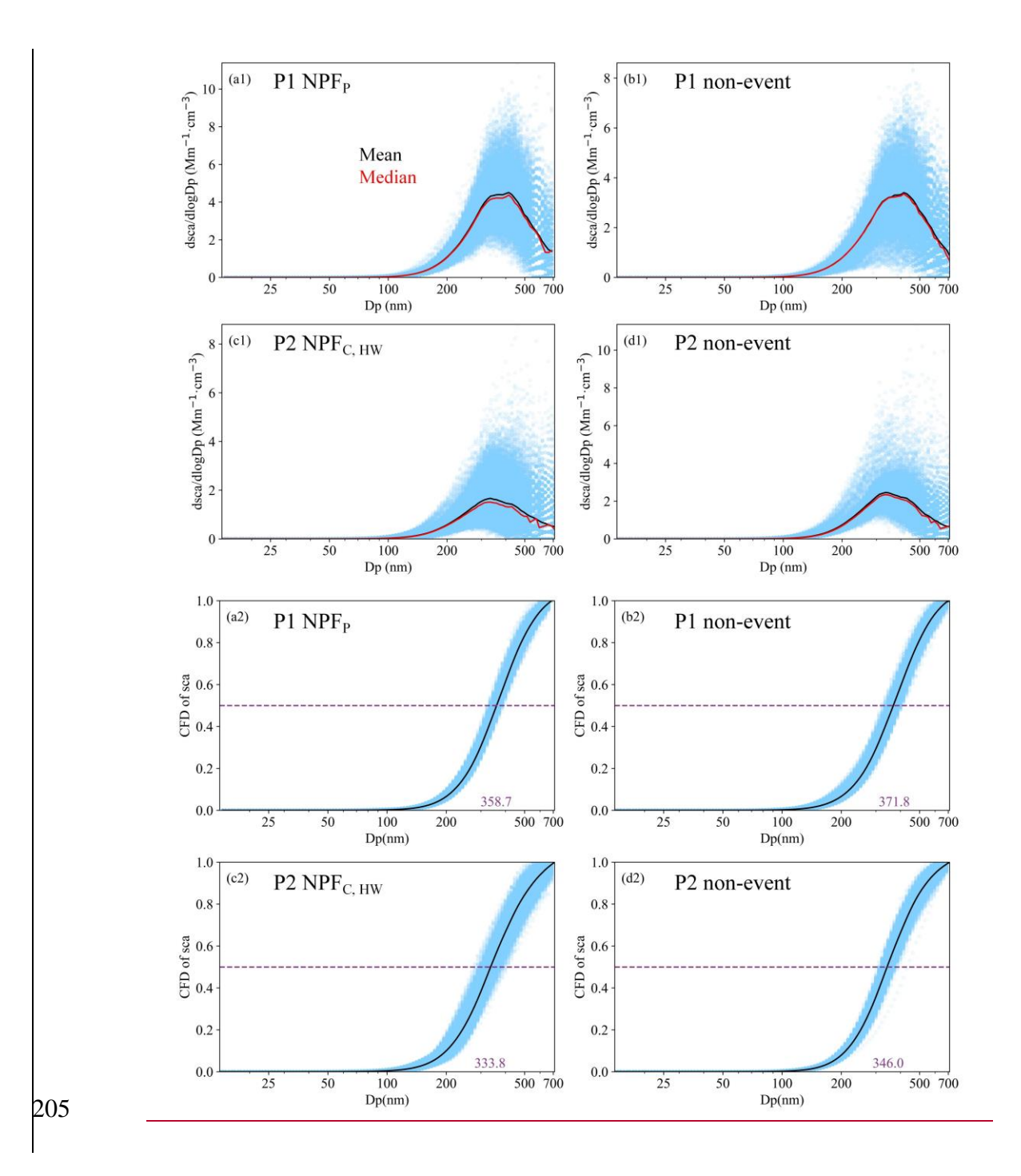


Figure S811. Correlation between the particle volume concentration determined by SMPS and $\sigma_{sca, 525}$ measured by the humidified nephelometer system during the study period. The solid line represents the fitting line.



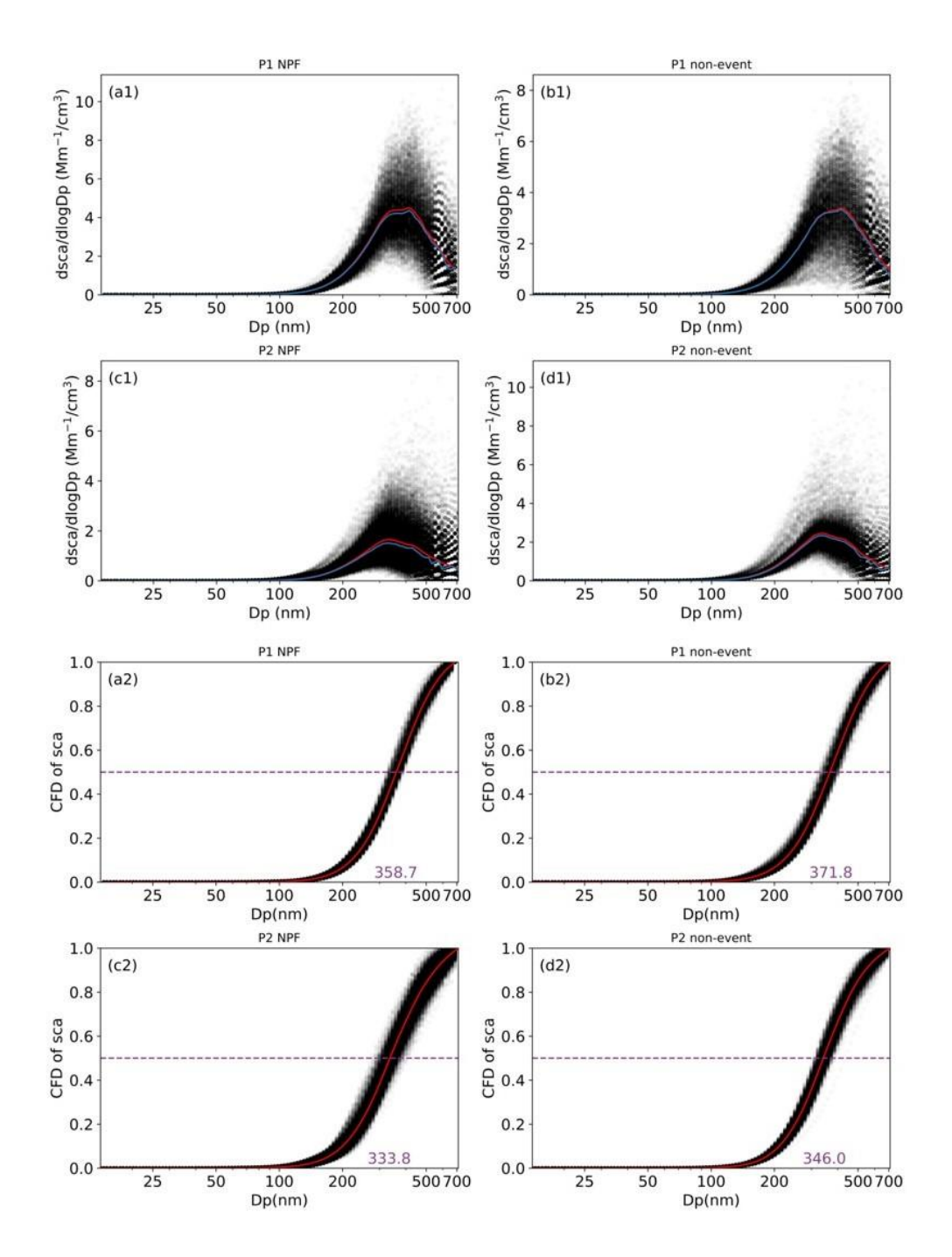
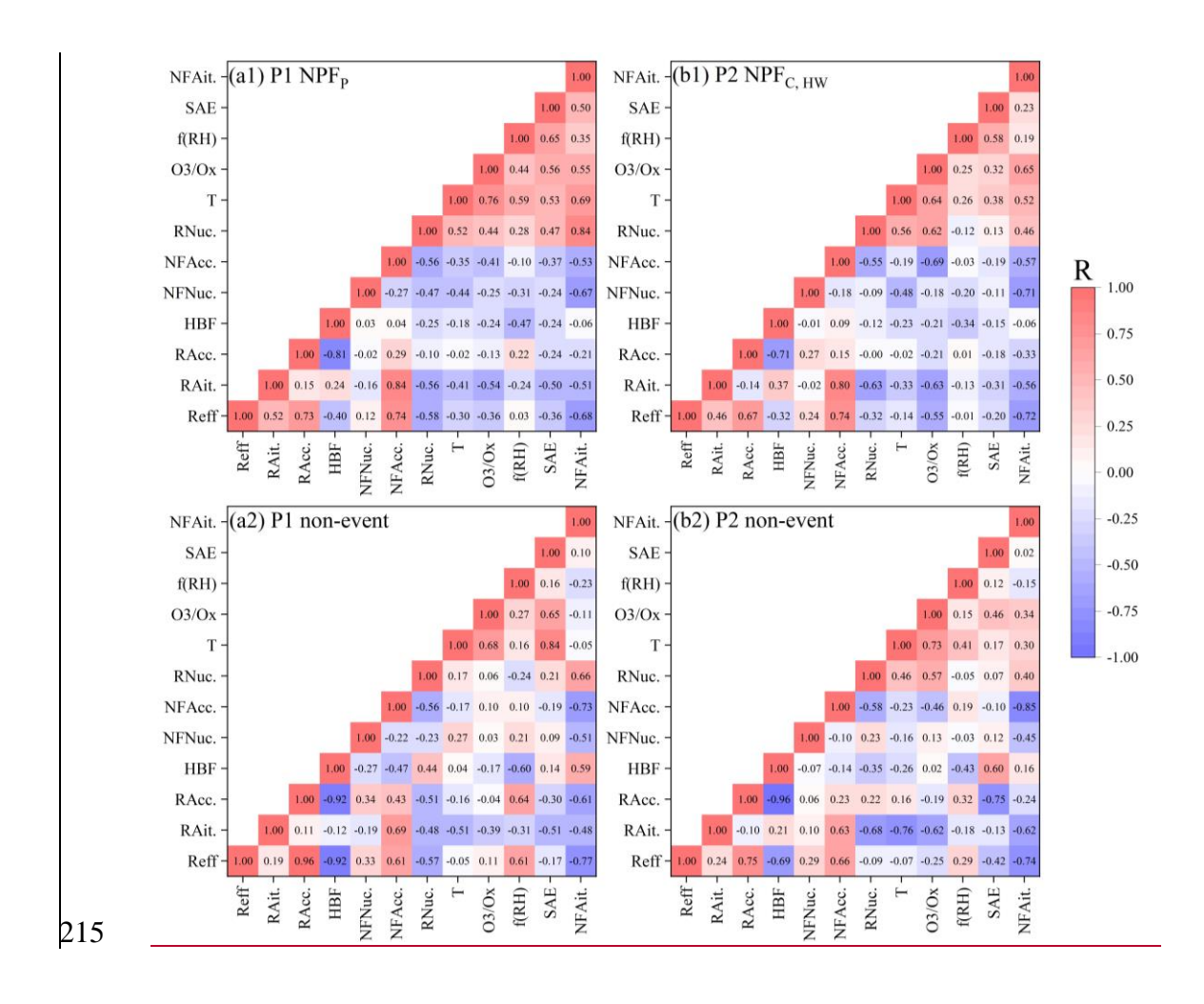


Figure S912. The size-resolved $\sigma_{sca, 525}$ distributions (**a1-d1**) and size-resolved $\sigma_{sca, 525}$ cumulative frequency distribution (**a2-d2**) for different event categories. The red and blue lines represent the mean and median values, the purple dashed line and the purple numbers on the abscissa represent the 50% cumulative frequency and the corresponding particle size (D₅₀), respectively.

- 212 S8. Correlation coefficients between different PNSD-related parameters,
- 213 temperature, O₃/O_x, aerosol optical and hygroscopic properties on NPF (non-event)
- 214 days during either P1 or P2 period



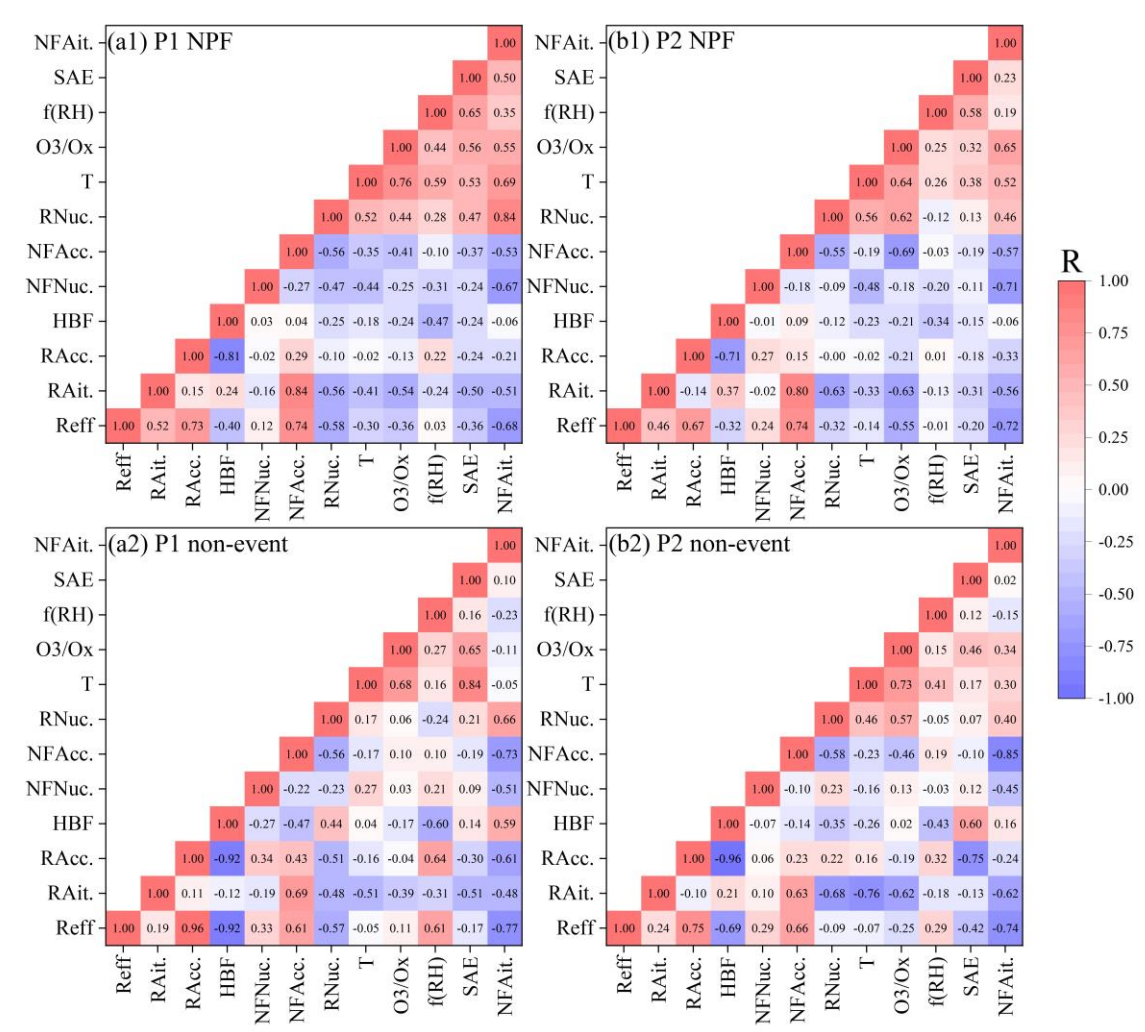


Figure S103. Correlation coefficients between different PNSD-related parameters (R_{eff}, R_{Nuc.}, R_{Ait.}, R_{Acc.}, NF_{Nuc.}, NF_{Ait.}, NF_{Acc.}), temperature (T), O₃/O_X, HBF, SAE, and *f*(RH) during NPF events (**a1**, **b1**) and non-event days (**a2**, **b2**) over the 08:00-22:00 <u>LT</u> time window.

S9. The relationship among f(RH), $R_{\rm eff}$, and $VF_{\rm Acc.}$ on P1 and P2 NPF days, as well as the relationship among f(RH), $SAE_{635/450}$ and temperature on P1 and P2 non-event days

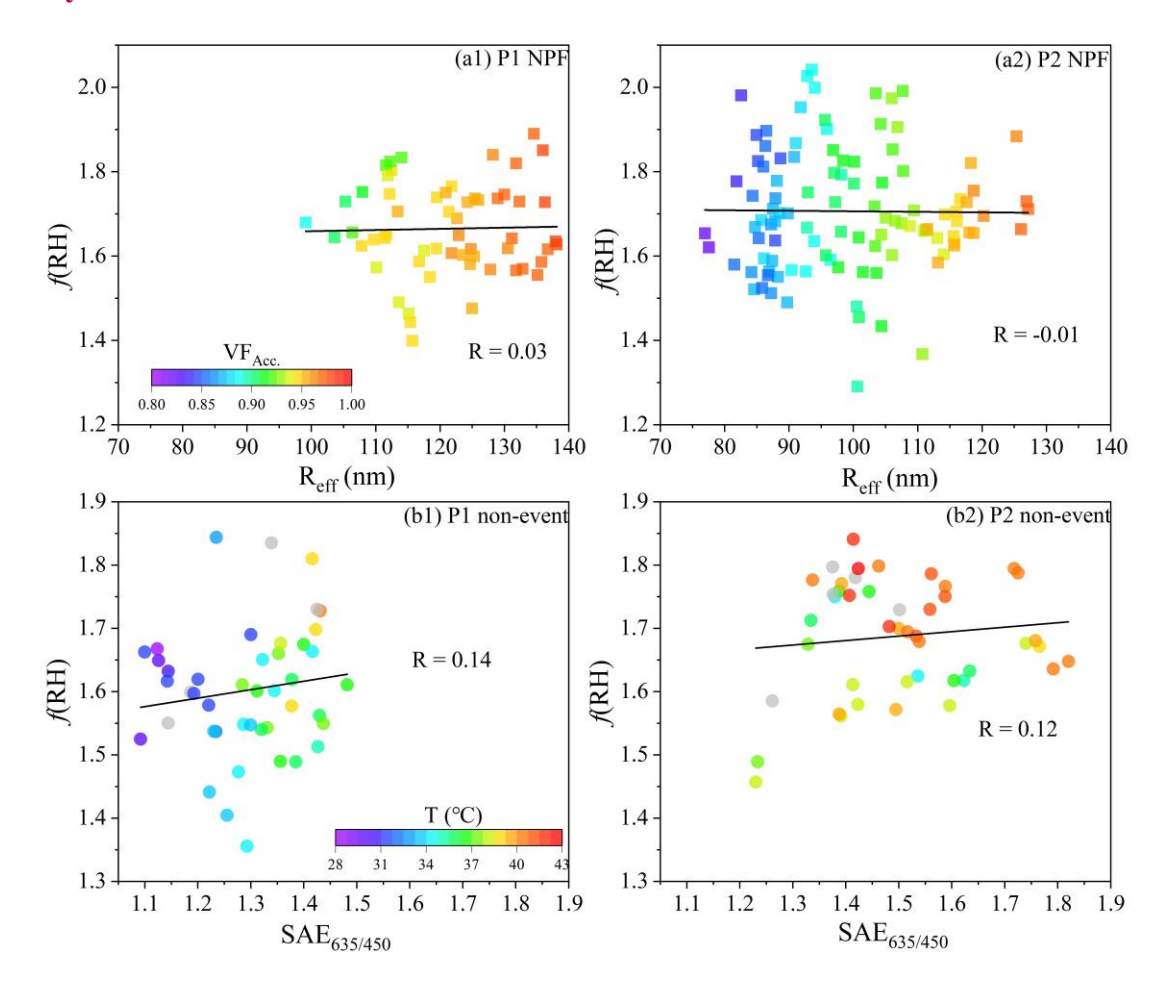


Figure S11. (a1-a2) The relationship among f(RH) and R_{eff} , as well as the VF_{Ace.} (as indicated by the color bar) on P1 and P2 NPF days during the 08:00-22:00 time window. (b1-b2) The corresponding relationship among f(RH) and SAE_{635/450}, as well as temperature (as denoted by the color bar) for non-event cases.

Table S1. Specific dates for different event categories during P1 and P2 periods.

Period	Category	Date		
P1	NPF	7.29, 8.1-3		
	non-event	8.4-6		
	Undefined	7.30-31		
P2	NPF	8.7-9, 8.12-14, 8.19		
	non-event	8.11, 8.15-16		
	Undefined	8.10, 8.17-18		

Table S2. A summary (avg. \pm std.) of humidified nephelometer system determined parameters (σ_{sca} , $\sigma_$

	NPF		non-event		Overall	
	P1	P2	P1	P2	P1	P2
σ _{sca, 525} (Mm ⁻¹)	103.8 ± 30.4	33.2 ± 11.7	76.7 ± 23.5	54.7 ± 17.6	88.0 ± 29.3	41.2 ± 16.0
f(RH)	1.64 ± 0.10	$1.7\underline{1} \pm 0.2\underline{13}$	$1.6_{\underline{2}} \pm 0.1_{\underline{0}}$	$\frac{1.7}{1.66} \pm 0.12$	1.61 ± 0.12	1.71 ± 0.215
ALWC (μg·m ⁻³)	25.9 ± 6.6	10.2 ± 3.2	18.9 ± 7.5	14.8 ± 4.5	21.4 ± 7.8	12.0 ± 3.9
HBF_{525}	$0.13\underline{4} \pm 0.0\underline{07}\underline{4}$	0.1657 ± 0.011	$0.13\underline{3} \pm 0.04\underline{08}$	$0.15\underline{2} \pm 0.0\underline{216}$	$0.14\underline{35} \pm 0.0\underline{08}$	$0.15\underline{3} \pm 0.01\underline{2}$
$SAE_{635/450}$	1.3 <u>1</u> ± 0.1 <u>0</u>	1.548 ± 0.213	$1.3\frac{27}{2} \pm 0.11$	1.44 ± 0.216	$1.3\underline{29} \pm 0.1\underline{2}$	1.547 ± 0.216
$f_{ m W}$	0.47 ± 0.04	0.48 ± 0.05	0.46 ± 0.04	0.46 ± 0.06	0.46 ± 0.05	0.48 ± 0.05
$N_{conc.}$ (10 ⁴ #·cm ⁻³)	1.4 ± 0.7	1.2 ± 0.6	0.9 ± 0.3	0.9 ± 0.3	1.2 ± 0.6	1.0 ± 0.6
$V_{conc.} (\mu m^3 \cdot cm^{-3})$	22.5 ± 5.5	10.1 ± 3.6	17.0 ± 4.8	15.9 ± 5.6	19.5 ± 6.0	12.1 ± 5.0
R_{eff} (nm)	124.8 ± 10.7	102.8 ± 12.4	126.2 ± 10.6	118.6 ± 11.4	125.0 ± 10.0	110.6 ± 13.7
NF _{ACC} .	0.28 ± 0.11	0.20 ± 0.10	0.28 ± 0.06	0.33 ± 0.07	0.28 ± 0.09	0.26 ± 0.11
VF _{ACC} .	0.96 ± 0.02	0.91 ± 0.04	0.96 ± 0.02	0.96 ± 0.02	0.96 ± 0.02	0.93 ± 0.04
T (°C)	34.0 ± 3.4	36.8 ± 3.1	33.2 ± 3.3	37.6 ± 2.7	33.8 ± 3.4	37.3 ± 3.0
RH (%)	46.6 ± 14.1	34.7 ± 9.1	52.6 ± 13.0	34.0 ± 7.5	47.9 ± 13.7	33.5 ± 8.5
WS (m/s)	1.1 ± 0.6	1.8 ± 1.0	1.4 ± 1.1	1.6 ± 0.9	1.2 ± 0.8	1.8 ± 1.0
VIS (km)	23.3 ± 6.3	29.9 ± 0.7	25.7 ± 5.1	29.2 ± 2.1	25.0 ± 5.6	29.8 ± 1.2
MLH (m)	1062.0 ± 475.6	1461.3 ± 529.9	1075.6 ± 415.4	1340.8 ± 589.8	1063.3 ± 465.8	1454.8 ± 562.6
PM _{2.5} (μg·m ⁻³)	18.3 ± 6.2	9.3 ± 4.5	10.5 ± 4.2	11.8 ± 4.0	15.1 ± 6.6	10.1 ± 4.4

NO ₂ (μg·m ⁻³)	30.8 ± 18.7	22.7 ± 12.8	21.7 ± 9.6	33.4 ± 19.2	29.8 ± 19.1	24.8 ± 15.4
$SO_2 (\mu g \cdot m^{-3})$	7.2 ± 1.8	8.8 ± 2.3	6.4 ± 1.5	9.6 ± 3.9	6.9 ± 1.8	9.0 ± 3.0
$O_3 \left(\mu g \cdot m^{-3}\right)$	108.2 ± 62.2	84.1 ± 50.2	98.7 ± 51.9	82.3 ± 58.3	100.2 ± 61.1	82.5 ± 49.5
CO (mg·m ⁻³)	0.57 ± 0.10	0.44 ± 0.09	0.53 ± 0.05	0.51 ± 0.10	0.55 ± 0.10	0.45 ± 0.09
O_3/O_X	0.71 ± 0.24	0.72 ± 0.21	0.78 ± 0.14	0.62 ± 0.27	0.70 ± 0.25	0.70 ± 0.22
<u>FR (cm⁻³·s⁻¹)</u>	17.10 ± 7.79	11.22 ± 6.81	<u> </u>	<u>/</u>	<u>/</u>	<u>/</u>
$\underline{GR}_{<25 \text{ nm}} (\underline{nm} \cdot \underline{h}^{-1})$	13.68 ± 3.39	9.31 ± 3.23	<u>/</u>	<u>/</u>	<u> </u>	<u> </u>
$\underline{GR_{25\text{-}40nm}(nm\!\cdot\!h^{\text{-}1})}$	7.12 ± 2.05	9.22 ± 4.28	<u>/</u>	<u>/</u>	<u>/</u>	<u>/</u>
$\underline{GR}_{40\text{-}60\;nm}\underline{\ (nm\cdot h^{\text{-}1})}$	6.87 ± 6.27	4.41 ± 1.72	<u>/</u>	<u>/</u>	<u>/</u>	<u>/</u>
$GR_{\underline{60-80 \text{ nm}}} (nm \cdot h^{-1})$	$\frac{13.710.73}{3.48.37} \pm$	$9.35.51 \pm 3.22.98$	/	/	/	/
CS (s ⁻¹)	$2.3 \pm 0.4 \times 10^{-2}$	$1.3 \pm 0.3 \times 10^{-2}$	/	/	/	/
CoagS (s ⁻¹)	$1.3 \pm 0.2 \times 10^{-4}$	$0.9 \pm 0.2 \times 10^{-4}$	/	/	/	/
$HBF_{525,RH}\!/\!HBF_{525}$	$1.2_{\underline{2}} \pm 0.1_{\underline{0}}$	$1.8\underline{78} \pm 0.3\underline{29}$	$1.4\underline{39} \pm 0.2\underline{4}$	$1.4\underline{3} \pm 0.2\underline{18}$	1.32 ± 0.219	$1.6\underline{3} \pm 0.3\underline{29}$
$f_{RF}(RH)$	1.989 ± 0.217	2.21 ± 0.23	1.93 ± 0.14	2.01 ± 0.218	1.91 ± 0.216	2.15 ± 0.23

- 236 References
- Castro, L. M., Pio, C. A., Harrison, R. M., and Smith, D. J. T.: Carbonaceous aerosol in
- 238 urban and rural European atmospheres: Estimation of secondary organic carbon
- 239 concentrations, Atmos. Environ., 33, 2771–2781, https://doi.org/10.1016/S1352-
- 240 2310(98)00331-8, 1999.
- Chen, J., Wu, Z., Chen, J., Reicher, N., Fang, X., Rudich, Y., and Hu, M.: Size-resolved
- 242 atmospheric ice-nucleating particles during East Asian dust events, Atmos. Chem. Phys.,
- 243 <u>21, 3491–3506, https://doi.org/10.5194/acp-21-3491-2021, 2021.</u>
- 244 Chow, J. C., Watson, J. G., Chen, L. W. A., Chang, M. C. O., Robinson, N. F., Trimble,
- D., and Kohl, S.: The IMPROVE_A temperature protocol for thermal/optical carbon
- analysis: Maintaining consistency with a long-term database, J. Air Waste Manag. Assoc.,
- 247 57, 1014–1023, https://doi.org/10.3155/1047-3289.57.9.1014, 2007.
- 248 Chow, J. C., Watson, J. G., Robles, J., Wang, X., Chen, L. W. A., Trimble, D. L., Kohl, S.
- D., Tropp, R. J., and Fung, K. K.: Quality assurance and quality control for thermal/optical
- analysis of aerosol samples for organic and elemental carbon, Anal. Bioanal. Chem., 401,
- 251 3141–3152, https://doi.org/10.1007/s00216-011-5103-3, 2011.
- Dal Maso, M., Kulmala, M., Riipinen, I., Wagner, R., Hussein, T., Aalto, P. P., and
- Lehtinen, K. E. J.: Formation and growth of fresh atmospheric aerosols: Eight years of
- aerosol size distribution data from SMEAR II, Hyytiälä, Finland, Boreal Environ. Res., 10,
- 255 323–336, 2005.
- Denjean, C., Formenti, P., Picquet-Varrault, B., Camredon, M., Pangui, E., Zapf, P., Katrib,
- Y., Giorio, C., Tapparo, A., Temime-Roussel, B., Monod, A., Aumont, B., and Doussin, J.
- F.: Aging of secondary organic aerosol generated from the ozonolysis of α -pinene: Effects
- of ozone, light and temperature, Atmos. Chem. Phys., 15, 883–897,
- 260 https://doi.org/10.5194/acp-15-883-2015, 2015.
- Dominick, D., Wilson, S. R., Paton-Walsh, C., Humphries, R., Guérette, E. A., Keywood,
- 262 M., Kubistin, D., and Marwick, B.: Characteristics of airborne particle number size

- 263 distributions in a coastal-urban environment, Atmos. Environ., 186, 256–265,
- 264 https://doi.org/10.1016/j.atmosenv.2018.05.031, 2018.
- Fitsiou, E., Pulido, T., Campisi, J., Alimirah, F., and Demaria, M.: Cellular Senescence and
- the Senescence-Associated Secretory Phenotype as Drivers of Skin Photoaging, J. Invest.
- 267 Dermatol., 141, 1119–1126, https://doi.org/10.1016/j.jid.2020.09.031, 2021.
- Grainger, R. G., Lambert, A., Rodgers, C. D., Taylor, F. W., and Deshler, T.: Stratospheric
- aerosol effective radius, surface area and volume estimated from infrared measurements, J.
- 270 Geophys. Res., 100, https://doi.org/10.1029/95jd00988, 1995.
- Hamed, A., Joutsensaari, J., Mikkonen, S., Sogacheva, L., Dal Maso, M., Kulmala, M.,
- Cavalli, F., Fuzzi, S., Facchini, M. C., Decesari, S., Mircea, M., Lehtinen, K. E. J., and
- Laaksonen, A.: Nucleation and growth of new particles in Po Valley, Italy, Atmos. Chem.
- 274 Phys., 7, 355–376, https://doi.org/10.5194/acp-7-355-2007, 2007.
- Hansen, J. E. and Travis, L. D.: Light scattering in planetary atmospheres, Space Sci. Rev.,
- 276 16, 527–610, https://doi.org/10.1007/BF00168069, 1974.
- Hao, Y., Gou, Y., Wang, Z., Huang, W., Wan, F., Tian, M., and Chen, J.: Current
- challenges in the visibility improvement of urban Chongqing in Southwest China: From
- the perspective of PM2.5-bound water uptake property over 2015–2021, Atmos. Res., 300,
- 280 107215, https://doi.org/10.1016/j.atmosres.2023.107215, 2024.
- Kerminen, V. M., Chen, X., Vakkari, V., Petäjä, T., Kulmala, M., and Bianchi, F.:
- Atmospheric new particle formation and growth: Review of field observations, Environ.
- 283 Res. Lett., 13, https://doi.org/10.1088/1748-9326/aadf3c, 2018.
- 284 Kuang, Y., He, Y., Xu, W., Zhao, P., Cheng, Y., Zhao, G., Tao, J., Ma, N., Su, H., Zhang,
- Y., Sun, J., Cheng, P., Yang, W., Zhang, S., Wu, C., Sun, Y., and Zhao, C.: Distinct diurnal
- variation in organic aerosol hygroscopicity and its relationship with oxygenated organic
- 287 aerosol, Atmos. Chem. Phys., 20, 865–880, https://doi.org/10.5194/acp-20-865-2020,
- 288 2020.

- 289 Kuang, Y., Zhao, C. S., Zhao, G., Tao, J. C., Xu, W., Ma, N., and Bian, Y. X.: A novel
- 290 method for calculating ambient aerosol liquid water content based on measurements of a
- 291 humidified nephelometer system, Atmos. Meas. Tech., 11, 2967–2982,
- 292 https://doi.org/10.5194/amt-11-2967-2018, 2018.
- Kuang, Y., Zhao, C., Tao, J., Bian, Y., Ma, N., and Zhao, G.: A novel method for deriving
- 294 the aerosol hygroscopicity parameter based only on measurements from a humidified
- 295 nephelometer system, Atmos. Chem. Phys., 17, 6651–6662, https://doi.org/10.5194/acp-
- 296 17-6651-2017, 2017.
- 297 Kulmala, M., Petäjä, T., Nieminen, T., Sipilä, M., Manninen, H. E., Lehtipalo, K., Dal
- 298 Maso, M., Aalto, P. P., Junninen, H., Paasonen, P., Riipinen, I., Lehtinen, K. E. J.,
- 299 Laaksonen, A., and Kerminen, V. M.: Measurement of the nucleation of atmospheric
- aerosol particles, Nat. Protoc., 7, 1651–1667, https://doi.org/10.1038/nprot.2012.091, 2012.
- 301 Lu, Y., Yan, C., Fu, Y., Chen, Y., Liu, Y., Yang, G., Wang, Y., Bianchi, F., Chu, B., Zhou,
- 302 Y., Yin, R., Baalbaki, R., Garmash, O., Deng, C., Wang, W., Liu, Y., Petäjä, T., Kerminen,
- V. M., Jiang, J., Kulmala, M., and Wang, L.: A proxy for atmospheric daytime gaseous
- 304 sulfuric acid concentration in urban Beijing, Atmos. Chem. Phys., 19, 1971–1983,
- 305 https://doi.org/10.5194/acp-19-1971-2019, 2019.
- Nairn, J. R. and Fawcett, R. J. B.: The excess heat factor: A metric for heatwave intensity
- and its use in classifying heatwave severity, Int. J. Environ. Res. Public Health, 12, 227—
- 308 <u>253, https://doi.org/10.3390/ijerph120100227, 2014.</u>
- Peng, C., Tian, M., Chen, Y., Wang, H., Zhang, L., Shi, G., Liu, Y., Yang, F., and Zhai,
- 310 C.: Characteristics, formation mechanisms and potential transport pathways of PM2.5 at a
- rural background site in Chongqing, Southwest China, Aerosol Air Qual. Res., 19, 1980–
- 312 1992, https://doi.org/10.4209/aaqr.2019.01.0010, 2019.
- 313 Peng, C., Tian, M., Wang, X., Yang, F., Shi, G., Huang, R. J., Yao, X., Wang, Q., Zhai, C.,
- Zhang, S., Qian, R., Cao, J., and Chen, Y.: Light absorption of brown carbon in PM2.5 in
- 315 the Three Gorges Reservoir region, southwestern China: Implications of biomass burning

- 316 and secondary formation, Atmos. Environ., 229, 117409,
- 317 https://doi.org/10.1016/j.atmosenv.2020.117409, 2020.
- Rissler, J., Vestin, A., Swietlicki, E., Fisch, G., Zhou, J., Artaxo, P., and Andreae, M. O.:
- 319 Size distribution and hygroscopic properties of aerosol particles from dry-season biomass
- burning in Amazonia, Atmos. Chem. Phys., 6, 471–491, https://doi.org/10.5194/acp-6-
- 321 471-2006, 2006.
- Rosati, B., Isokääntä, S., Christiansen, S., Jensen, M. M., Moosakutty, S. P., De Jonge, R.
- W., Massling, A., Glasius, M., Elm, J., Virtanen, A., and Bilde, M.: Hygroscopicity and
- 324 CCN potential of DMS-derived aerosol particles, Atmos. Chem. Phys., 22, 13449–13466,
- 325 https://doi.org/10.5194/acp-22-13449-2022, 2022.
- Stein, A. F., Draxler, R. R., Rolph, G. D., Stunder, B. J. B., Cohen, M. D., and Ngan, F.:
- Noaa's hysplit atmospheric transport and dispersion modeling system, Bull. Am. Meteorol.
- 328 Soc., 96, 2059–2077, https://doi.org/10.1175/BAMS-D-14-00110.1, 2015.
- 329 Strader, R., Lurmann, F., and Pandis, S. N.: Evaluation of secondary organic aerosol
- 330 formation in winter, Atmos. Environ., 33, 4849–4863, https://doi.org/10.1016/S1352-
- 331 2310(99)00310-6, 1999.
- Tian, J., Guan, H., Zhou, Y., Zheng, N., Xiao, H., Zhao, J., Zhang, Z., and Xiao, H.:
- Isotopic source analysis of nitrogen-containing aerosol: A study of PM2.5 in Guiyang (SW,
- 334 China), Sci. Total Environ., 760, 143935, https://doi.org/10.1016/j.scitotenv.2020.143935,
- 335 **2021**.
- Wan, F., Hao, Y., Huang, W., Wang, X., Tian, M., and Chen, J.: Hindered visibility
- improvement despite marked reduction in anthropogenic emissions in a megacity of
- 338 southwestern China: An interplay between enhanced secondary inorganics formation and
- 339 hygroscopic growth at prevailing high RH conditions, Sci. Total Environ., 895, 165114,
- 340 https://doi.org/10.1016/j.scitotenv.2023.165114, 2023.
- Wang, H., Tian, M., Chen, Y., Shi, G., Liu, Y., Yang, F., Zhang, L., Deng, L., Yu, J., Peng,
- 342 C., and Cao, X.: Seasonal characteristics, formation mechanisms and source origins of

- 343 PM2.5 in two megacities in Sichuan Basin, China, Atmos. Chem. Phys., 18, 865–881,
- 344 https://doi.org/10.5194/acp-18-865-2018, 2018.
- Wang, Y. Q.: MeteoInfo: GIS software for meteorological data visualization and analysis,
- Meteorol. Appl., 21, 360–368, https://doi.org/10.1002/met.1345, 2014.
- 347 Xu, W., Kuang, Y., Bian, Y., Liu, L., Li, F., Wang, Y., Xue, B., Luo, B., Huang, S., Yuan,
- 348 B., Zhao, P., and Shao, M.: Current Challenges in Visibility Improvement in Southern
- 349 China, Environ. Sci. Technol. Lett., 7, 395–401,
- 350 https://doi.org/10.1021/acs.estlett.0c00274, 2020.
- 351 Xue, B., Kuang, Y., Xu, W., and Zhao, P.: Joint increase of aerosol scattering efficiency
- and aerosol hygroscopicity aggravate visibility impairment in the North China Plain, Sci.
- 353 Total Environ., 839, 141163, https://doi.org/10.1016/j.scitotenv.2022.156279, 2022.
- 354 Zhu, Y., Shen, Y., Li, K., Meng, H., Sun, Y., Yao, X., Gao, H., Xue, L., and Wang, W.:
- 355 Investigation of Particle Number Concentrations and New Particle Formation With Largely
- Reduced Air Pollutant Emissions at a Coastal Semi-Urban Site in Northern China, J.
- 357 Geophys. Res. Atmos., 126, 1–20, https://doi.org/10.1029/2021JD035419, 2021.